ISSN:2661-4448(online)
2661-443X(print)
Volume 1 No.1 2019

MECHANICAL ENGINEERING SCIENCE

VISER
www.viserdata.com

COMPANY INTRODUCTION

公司简介

维泽科技文化有限公司(Viser Technology Pte. Ltd.)成立于新加坡，是一家科技与文化高度融合的创新型企业。我们拥有一支具有较高文化素质、管理素质和业务素质的团队，聚焦于国际开源中英文期刊、体现文化含量与学术价值图书的出版发行。秉承“传播科技文化，促进学术交流”的理念，与国内外知名院校，科研院所及数据库建立了稳定的合作关系。坚持开拓创新，实施“跨越–融合”的发展战略，立足中国、新加坡两地，辐射全球，并于中国设立河北和重庆两个分部。我们将紧紧围绕专业化、特色化的发展道路，不断营造“有情怀，有视野，有梦想”的企业文化氛围，独树一帜，做一家“有血、有肉、有温度”的创新型出版企业。

Viser Technology Pte. Ltd. was founded in Singapore with branch offices in both Hebei and Chongqing, China. Viser focuses on publishing scientific and technological journals and books that promote the exchange of scientific and technological findings among the research community and around the globe. Despite being a young company, Viser is actively connecting with well-known universities, research institutes, and indexation database, and has already established a stable collaborative relationship with them. We also have a group of experienced editors and publishing experts who are dedicated to publishing high-quality journal and book contents. We offer the scholars various academic journals covering a variety of subjects and we are committed to reducing the hassles of scholarly publishing. To achieve this goal, we provide scholars with an all-in-one platform that offers solutions to every publishing process that a scholar needs to go through in order to show their latest finding to the world.

Mechanical Engineering Science

VISER

Publisher: Viser Technology Pte. Ltd.

ISSN: 2661-4448 (online)

2661-443X (print)

Frequency: Semi-annual

Add.:21 Woodlands Close, #08-18,

Primz Bizhub SINGAPORE (737854)

https://www.viserdata.com/

Mechanical Engineering Science

Volume 1 No.1 (2019)

CONTENTS

VISER

Viser Technology Pte. Ltd.
Mechanical Engineering Science
https://doi.org/10.33142/me.v1i1.654

Research Article Open Access

Computing Method of Multivariate Process Capability Index Based on Normalized Pretreatment

Guangqi Ying[1], Yan Ran[*], Genbao Zhang, Yuxin Liu, Shengyong Zhang

State Key Laboratory of Mechanical Transmission, Chongqing University, Chongqing, China 400030

***Corresponding Author:** Yan Ran, Chongqing University, Chongqing, ranyan@cqu.edu.cn.*

Abstract:
For the traditional multi-process capability construction method based on principal component analysis, the process variables are mainly considered, but not the process capability, which leads to the deviation of the contribution rate of principal component. In response to the question, this paper first clarifies the problem from two aspects: theoretical analysis and example proof. Secondly, aiming at the rationality of principal components degree, an evaluation method for pre-processing data before constructing MPCI using PCA is proposed. The pre-processing of data is mainly to standardize the specification interval of quality characteristics making the principal components degree more reasonable and optimizes the process capability evaluation method. Finally, the effectiveness and feasibility of the method are proved by an application example.

Keywords: *Multivariate process capability index; The standard range; Contribution degree; Specification intervals*

Citation: G.Q. Ying et al, Computing Method of Multivariate Process Capability Index Based on Normalized Pretreatment. *Mech Eng Sci*, 2019,1(1): 1-6. https://doi.org/10.33142/me.v1i1.654

1. Introduction

Process capability is the consistency index of machining process. In order to measure, evaluate, analyze, and compare process capabilities, quantifiable indicators as Process Capability Index (PCI) are practically used. The concept of process capability ratio are firstly proposed by Juran[1], who compared process fluctuations with process specification as a quantitative index to evaluate process capability. Other quantifiable indicators that have emerged since then are based on process fluctuations and specifications, such as C_p, C_{pk} and C_{pm}. With the improvement of processing level and increasingly complex parts, the processing parts generally have multiple quality characteristics, and the process capability evaluation needs to consider multiple quality characteristics. Since the concept of a multi-process capability index are proposed by Chan L K et al.[2], Process Capability Index multivariate analysis model was constructed as the following categories: the multi-process capability index (MPCI) was constructed by region ratio, such as the method for evaluating the process area that are presented by Shahriari et al.[3], and the spatial MPCI proposed by Wang S. X et al.[4] to solve the eccentricity of multivariate quality features. MPCI was constructed by a failure rate, such as Wierda et al.[5] Bothe et al.[6] and Chen K S et al.[7]. MPCI was constructed by principal component analysis, such as the process capability index of principal components proposed by Wang KF and Chen JC[8], Wang FK and Du TC[9], Ma Yizhong[10] and Wang Rang CH[11] to build multi-quality characteristics index. And based on the correlation of the specification intervals, Shinde et al.[12] and Zhang M et al.[13] modified the specification interval. MPCI is constructed by vector method, such as a new multivariate capability vector that are proposed by Shahriari and Abdollahzadeh[14]. In addition to the methods above, there are another method. Pan[15] proposed two new multi-process capability indices: NMC_p and NMC_{pm}.

In the traditional Principal Component Analysis (PCA) constructing the Multivariate Process Capability Index (MPCI), a few principal components mainly consider process variation but not process capability, which is unreasonable. Therefore, aiming at the rationality of principal components degree, an evaluation method for pre-processing data before constructing MPCI using PCA is proposed.

2. Principal Component Analysis theory

When the mass data of multi-quality feature parts obeys the multivariate normal distribution, the principal component analysis is proposed by Wang KF and Chen JC[8] to construct the multivariate process capability index. They extended the one-unit capability index to pluralism and defined the multivariate process capability indices: MC_p, MC_{pk}, MC_{pm} and MC_{pmk}.

When using the principal component analysis method, a small number of principal components can explain about 90% of the process variation. In terms of construction methods, the method of weighted averaging is used by Ma Yizhong[10]. According to the fluctuations, for each principal component index, different weights are assigned. Take Cp as an example:

$$MCp = \sum_{i=1}^{v} r_i Cp;PC_i \tag{1}$$

And Wang F K and Du T C[9] and Wang Rang C H[11] use geometric mean, namely:

$$MCp=\left(\prod_{i=1}^{v} Cp;PC_i\right)^{1/v} \tag{2}$$

Where

$$Cp;PC_i = \frac{USL_{PC_i} - LSL_{PC_i}}{6\sigma_{PC_i}}$$

Where, $r_i = \lambda_i / tr(\Lambda, tr(\Lambda) = \lambda_1 + \lambda_2 + ... + \lambda_v$, here, $\lambda_1, \lambda_2, ...\lambda_p$ is the feature vector of Σ, $Cp;PC_i$ is the single process capability index of the i-th principal component, and V represents the number of principal components which can explain about 90% of the process variation. The specification range and target value of the principal component are:

$$LSL_{PCi} = u_i' LSL \quad USL_{PCi} = u_i' USL \tag{3}$$

Where, $u_1, u_2, ..., u_p$ is the feature vector of Σ.

Shinde and Khadse[12] pointed out that the formulas calculated by Wang K F et al.[8-9] are biased, because in principal component analysis, only the distribution of principal components is independent, the canonical intervals of different principal components are still interrelated, and their viewpoints are verified by examples. At the same time, new specification intervals and multi-process capability indices are defined.

$$\begin{aligned} V = \{ &(y_1, y_2, ...y_v) | LSL_X \le Uy \le USL_X, \\ &y' = (y_1, y_2, ...y_P), y_r = EY_r \} \\ &r = v+1, v+2, ..., p \end{aligned} \tag{4}$$

Where, y is the observations of the principal component (PC), V is not a super-rectangular, it is composed of 2p linear inequalities (p is the number of quality features).

$$Mp_1 = P\left\{ \begin{array}{l} Y = (Y_1, Y_2, ..., Y_v)' \in V' \\ |Y \sim N_v(\mu_Y = T_Y, \Sigma_Y = diag(\lambda_1, ..., \lambda_v)) \end{array} \right\} \tag{5}$$

$$Mp_2 = P\left\{ \begin{array}{l} Y = (Y_1, Y_2, ..., Y_v)' \in V' \\ |Y \sim N_v(\mu_Y, \Sigma_Y = diag(\lambda_1, ..., \lambda_v)) \end{array} \right\} \tag{6}$$

Y represents the vector of PC, Mp_1 is similar to MCp, Mp_2 is similar to $MCpk$ .If $Mp_1 \ge 0.9973$,it indicates that this process has potential capability. If $Mp_2 \ge 0.9973$,it indicates that this process has actual capability.

3. The principal component contribution rate

The contribution rate of the principal component was determined by the variance ratio of the quality feature and the correlation coefficient. For convenience of explanation, the following two quality characteristics are taken as examples to describe and calculate the principle component contribution rate.

3.1 Theoretical analysis of the influencing factors of the principal component contribution rate

It is known from Figure 1 that when the correlation coefficients of quality control features are same, the contribution rate of each principal component is only affected by the variance difference of each quality feature. Moreover, the higher the variance of quality characteristics, the higher the contribution rate of the first principal component. From the comparison of the three curves in Figure 1, it is found that with the increase of the variance ratio of the quality features, the correlation coefficient between quality characteristics has less influence on the contribution rate of the first principal component. When the standard deviation ratio of quality characteristics is more than 9 times, the contribution rate of the first principal component is independent from the correlation coefficient of the quality feature. What's more, it is only determined by the ratio of variance between quality characteristics. At this time, the contribution rate of the first principal component is approximately equal to the proportion of the maximum variance to the total variance.

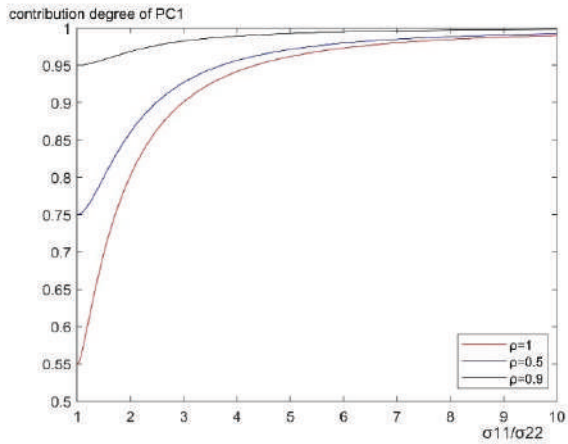

Figure 1. Variance ratio of quality characteristic influence on principal component contribution degree

As is shown in Figure 2, when the variances of the control quality characteristics are same, the contribution rate of each principal component is affected by the correlation coefficient between the various quality features, which indicates that the greater the correlation coefficient between the quality features, the greater the contribution rate of the first principal component.

From the theoretical analysis above, during analyzing the covariance matrix based on quality features, the contribution rate of principal components is determined by the variance ratio and the correlation coefficient between quality features. However, during calculating the multivariate process capability index, multivariate process capability index is not only related to the variance and the correlation coefficient of quality characteristics, but also to the quality characteristic interval. Therefore, it is not advisable and reasonable to use the contribution rate of principal components to represent and evaluate the contribution rate of multivariate process capability

3.2 Application of the principal component contribution rate

The gearbox base used in this paper has two quality characteristics, the width X_1 (60mm) and the height X_2 (90mm). $S = \{(X_1, X_2), 57 \le X_1 \le 63,\ 89.4 \le X_2 \le 90.6\}$ is the specification range. We collected 100 sets of sample data of this part. The sample mean vector and the covariance matrix are obtained as:

$$\overline{X} = (60.00, 90.00), \; S = \begin{pmatrix} 1 & 0 \\ 0 & 0.09 \end{pmatrix}$$

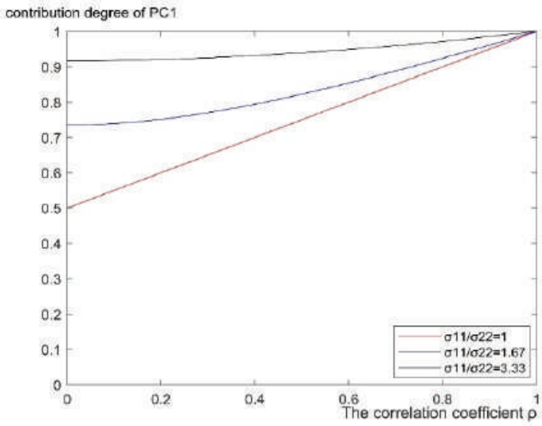

Fig 2. Correlation coefficient of quality characteristic influence on principal component contribution degree

Through principal component analysis based on covariance matrix, the principal component contribution rates of each quality characteristic are obtained as:

$$PC_1 = u_1 X = X_1 \sim N(60.00, 1)$$
$$PC_2 = u_2 X = X_2$$

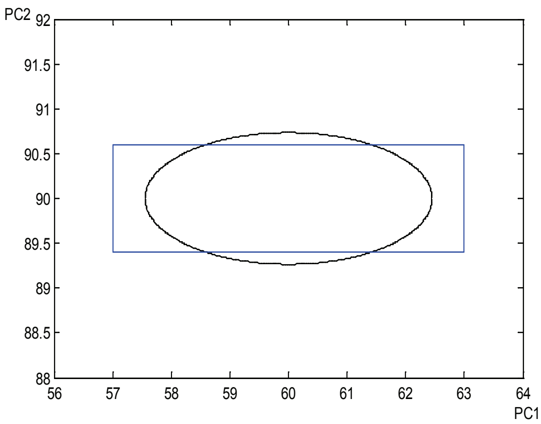

Figure 3 Principal component process capability

As shown in Figure 3, $U=(u_1,u_2)$ is the eigenvector of S. The ellipse represents the area of 95% process capability, and the rectangular refers to the specification interval.

Obviously, the process capability of the first principal component is greater than that of the second principal component, which indicated that using the first principal component to calculate the multivariate process capability index will inevitably, overestimated the multivariate process capability. Because 91,7% of the first principal component contribution rate only explains 91,7% of the variation but not the multivariate process capability. It is ignoring the influence of the specification interval on the contribution rate of the multi-process capability, that leads to the over-estimation of the multi-process capability.

As illustrated by the above example, when calculating the multivariate process capability index, using the principal component contribution rate to evaluate the multivariate process capability directly is not precise. To solve this problem, we proposed a new method based on processing raw data.

4. MPCI with improved principal component contribution rate

Different from the traditional principal component analysis method, MPCI with improved principal component contribution rate needs to preprocess the quality features to standardize the specification intervals of each quality feature.

4.1 Data preprocessing

Interval standardization:

$$H_i = (X_i - M_i) / d_i, \quad i = 1, 2, \ldots, p \tag{7}$$

where X_i is the original quality feature, H_i is the processed quality feature, M_i is the center of the X_i specification interval, and d_i is half of the interval between the upper and lower specification boundaries of X_i:

$$M_i = (USL_{Xi} + LSL_{Xi}) / 2 \qquad d_i = (USL_{Xi} - LSL_{Xi}) / 2$$

Through processing the original data, the specification intervals of all quality features are normalized to [-1, 1]. Thus, in the process of calculating the multivariate process capability index with the new data meter, the multivariate process capability index is only determined by the variance and correlation coefficient of the quality features.

In the process of principal component analysis of new data, because the principal component process with a residual contribution rate of less than 10% is very strong, these principal components can be ignored, and the total component is explained by a small part of the principal component whose cumulative contribution rate reaches 90% or more.

4.2 Multivariate process capability index calculation

For a part with p feature qualities $X_1, X_2, \ldots X_p$, its feature quality vector is $X' = [X_1, X_2, \ldots X_p]$, each of which has n sample points or observation data, and obeys $X \le N_p(\mu, \Sigma)$. $\acute{O}$ is the covariance matrix. Symbols used are defined as:

$T'_X = (T_1, T_2, \ldots, T_P)$: X target value vector

$LSL'_X = (LSL_1, LSL_2, \ldots, LSL_P)$: Lower specification limit of X

$USL'_X = (USL_1, USL_2, \ldots, USL_P)$: Upper specification limit of X

$S = \{x \mid LSL_X \le x \le USL_X\}$: X's super-rectangular specification interval

Quality characteristics H centralized treatment:

$$Z_i = H_i - \mu_{Zi}, \quad i = 1, 2, \ldots, p \tag{8}$$

So,

$Z \le N_p(0, \Sigma_z)$

Where,

$$\Sigma_z(X_i, X_j) = \frac{Cov(X_i, X_j)}{d_i d_j} \tag{9}$$

$\lambda_1 \le \lambda_2 \le \ldots \le \lambda_p$: Characteristic value of Σ_z.

$u_1, u_2, \ldots, u_p$: Characteristic vector of Σ_z.

Principal component vector:

$$Y = U'Z \tag{10}$$

Where, $U = (u_1, u_2, \ldots, u_p)$, $E(Y) = 0$.

Covariance of principal components:

$$COV(Y) = Diag(\lambda_1, \lambda_2, \ldots, \lambda_p) \tag{11}$$

Covariance of principal components:

$$T_{Zi} = \left(T_i - \mu_{Xi}\right) / d_i \tag{12}$$

Target value of quality characteristic Z_i:

$$T_Y = U' T_Z \tag{13}$$

Y specification area:

$$R = \left\{ \left(y_1, y_2, ... y_v\right) \middle| LSL_z \le (U')^{-1} y \le USL_z, \right.$$
$$\left. y' = \left(y_1, y_2, ... y_P\right), y_r = EY_r = 0 \right\}$$
$$r = v+1, v+2, ..., p \tag{14}$$

Probability that the principal component satisfies the specification area:

$$P_1 = P\begin{Bmatrix} Y=(Y_1, Y_2, ..., Y_v)' \le R \\ |YnN_v(\mu_Y = T_Y, \Sigma_Y = diag(\lambda_1, ..., \lambda_v)) \end{Bmatrix} \tag{15}$$

$$P_2 = P\begin{Bmatrix} Y = (Y_1, Y_2, ..., Y_v)' \in R \\ |Y \sim N_v(0, \Sigma_Y = diag(\lambda_1, ..., \lambda_v)) \end{Bmatrix} \tag{16}$$

Get the new MPCI at this point:

$$Mcp = \frac{1}{3}\Phi^{-1}\left(\frac{P1+1}{2}\right) \tag{17}$$

$$Mcpk = \frac{1}{3}\Phi^{-1}\left(\frac{P2+1}{2}\right) \tag{18}$$

5. Application

Take the gearbox housing produced by a domestic manufacturer as an example. The proposed multi-process capability index (MPCI) is used for the capability analysis of the gearbox housing. In the manufacturing process, the specification intervals of the quality characteristics X_1, X_2, X_3, and X_4 respectively are [-0.1, 0.1], [-0.035, 0.035], [-0.018, 0.004], and [-0.021, 0.004], and the target values are 0,0,-0.007 and -0.0085, respectively.

From the production process, 50 observation samples were randomly selected and according to the method of PAN et al.[15], the Shapiro-Wilk statistic was calculated to check whether the sampled data follows the multivariate normal distribution. The Shapiro-Wilk statistic is 0.304078, which is greater than 0.05. Therefore, the sampled data is considered to follow a multivariate normal distribution.

Calculate the sample mean vector $\overline{X}$ and the covariance matrix S:

$$\overline{X}' = \left[0.00841, 0.00281, -0.00743, -0.00821\right]'$$

$$S = \begin{pmatrix} 0.000\ 421\ 33 & & & \\ 0.000\ 146\ 98 & 0.000\ 083\ 88 & & \\ 0.000\ 054\ 25 & 0.000\ 025\ 18 & 0.000\ 010\ 52 & \\ -0.000\ 002\ 71 & 0.000\ 000\ 89 & -0.000\ 000\ 14 & 0.000\ 017\ 28 \end{pmatrix}$$

5.1 MPCI with improved principal component contribution rate

Preprocess X according to equations (7) and (8):

$$H_i = \left(X_i - M_i\right) / d_i, \quad Z_i = H_i - \mu_{Zi}, \quad i = 1, 2, ..., p$$

Calculate the Z-means vector $\overline{Z}$ and the covariance matrix S_z according to equation (9):

$$\overline{Z} = [0, 0, 0, 0]'$$

$$S_z = \begin{pmatrix} 0.042\ 133 & & & \\ 0.041\ 994 & 0.068\ 473 & & \\ 0.049\ 318 & 0.065\ 403 & 0.086\ 942 & \\ -0.002\ 168 & 0.002\ 034 & -0.001\ 018 & 0.110\ 592 \end{pmatrix}$$

Calculate each principal component according to equation (10):

$$\lambda_1 = 0.1753$$
$$PC_1 = Y_1 = \mu_1 \le Z = 0.4376Z_1 + 0.5883Z_2 + 0.6800Z_3 - 0.0069Z_4$$
$$\lambda_2 = 0.1107$$
$$PC_2 = Y_2 = \mu_2 \le Z = 0.0168Z_1 - 0.0272Z_2 + 0.0027Z_3 - 0.9995Z_4$$
$$\lambda_3 = 0.0118$$
$$PC_3 = Y_3 = \mu_3 \le Z = 0.3475Z_1 - 0.8076Z_2 + 0.4754Z_3 + 0.0292Z_4$$
$$\lambda_4 = 0.0104$$
$$PC_4 = Y_4 = \mu_4 \le Z = 0.8292Z_1 + 0.0286Z_2 - 0.5582Z_3 + 0.0117Z_4$$

In addition, the principal components Y_1, Y_2, Y_3, and Y_4 are independent of each other and obey the normal distribution, and their parameters are =(0, 0.1753), (0, 0.1107,（0,0.0118)，(0,0.0104）.The target vector of the principal component is (0.0422，-0.0283，0.1361，-0.0375). The first two principal components explain the overall difference of 92.8%, so the first two principal components were used to analyze the multivariate process capability.

Since Z can be expressed as , according to the Z section the specification interval of the first two principal components can be calculated. Because only the first two principal components are considered, the expectation of the other two principal components is used when calculating the specification region. Its specification area is as follows:

$$R = \left\{ (Y_1, Y_2) \middle| \begin{array}{c} \frac{-0.1+0.00342}{0.1} \le 0.4376Y_1 + 0.01627Y_2 \le \frac{0.1+0.00342}{0.1} \\ \frac{-0.035-0.00298}{0.035} \le 0.5883Y_1 - 0.0272Y_2 \le \frac{0.035-0.00298}{0.035} \\ \frac{-0.018+0.00826}{0.011} \le 0.6800Y_1 + 0.0027Y_2 \le \frac{0.004+0.00826}{0.011} \\ \frac{-0.021+0.00889}{0.0125} \le -0.0069Y_1 - 0.9948Y_2 \le \frac{0.004+0.00889}{0.0125} \\ E(y_3) = 0, E(y_4) = 0 \end{array} \right\}$$

As shown in Figure 4, the common area enclosed by 8 lines is the revised specification area:

$$R = \left\{ (Y_1, Y_2) \middle| \begin{array}{c} 0.5883Y_1 - 0.0272Y_2 \le 0.915 \\ -0.885 \le 0.6800Y_1 + 0.0027Y_2 \\ -0.969 \le -0.0069Y_1 - 0.9948Y_2 \le 1.031 \end{array} \right\}$$

According to equation (11), (12) and (13), the target values of principal component covariance and Y are calculated as follow:

$$\Sigma_Y = \begin{pmatrix} 0.1753 & 0 \\ 0 & 0.1107 \end{pmatrix}$$

T_Y=(0.0422，-0.0283)'

Calculate the probability that the principal component satisfies the specification region according to equations (15) and

(16):

P_1= 0.9965 P_2= 0.9962

MCP is calculated according to equation (17) and (18):

Mcp_1=0.9748

$MCpk_1$=0.9651

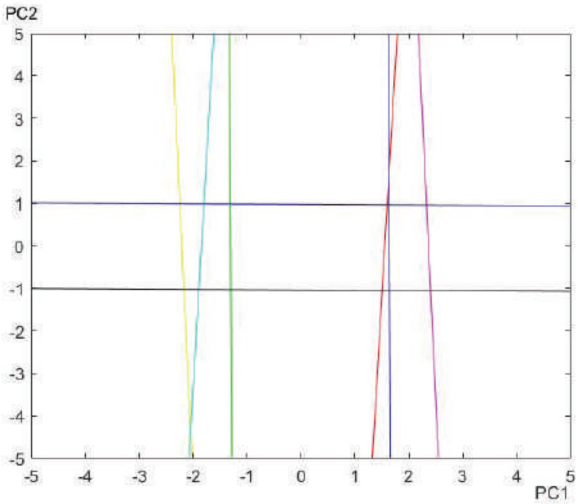

Figure 4 Revised specification area

5.2 Traditional principal component method of MPCI

Calculate the principal component based on the covariance:

$$\lambda_1 = 0.0004839$$

$$PC_1 = Y_1' = -0.9287Z_1' - 0.3491Z_2' - 0.1250Z_3' + 0.0048Z_4'$$

$$\lambda_2 = 0.0000299$$

$$PC_2 = Y_2' = 0.3622Z_1' - 0.9068Z_2' - 0.1637Z_3' - 0.1404Z_4'$$

$$\lambda_3 = 0.0000170$$

$$PC_3 = Y_3' = 0.0564Z_1' - 0.1247Z_2' - 0.0333Z_3' + 0.9900Z_4'$$

$$\lambda_4 = 0.0000022$$

$$PC_4 = Y_4' = 0.0562Z_1' + 0.2006Z_2' - 0.9780Z_3' - 0.0109Z_4'$$

Principal components Y_1, Y_2, Y_3, and Y_4 are independent from each other and subject to normal distribution, and their parameters are μ,σ^2 = (0,0.0004839), (0,0, 0.0000299 (0,0.0000170), and (0,0.0000022), respectively. The target vector of the principal component is (-0.0023, 0.0037, 0.0009, -0.0016). The first two principal components explain the overall difference of 96.4%, so the first two principal components were used to analyze the multivariate process capability.

$$R' = \left\{ \left(Y_1', Y_2'\right) \middle| \begin{array}{c} -0.1 + 0.00342 \le -0.9287Y_1' + 0.3622Y_2' \le 0.1 + 0.00342 \\ -0.035 - 0.00298 \le -0.3491Y_1' - 0.9068Y_2' \le 0.035 - 0.00298 \\ -0.018 + 0.00826 \le -0.1250Y_1' - 0.1637Y_2' \le 0.004 + 0.00826 \\ -0.021 + 0.00889 \le 0.0048Y_1' - 0.1404Y_2' \le 0.004 + 0.00889 \\ E(Y_3) = 0, E(Y_4) = 0 \end{array} \right\}$$

As shown in figure 5, the common area surrounded by 8 lines is the revised specification area:

$$R' = \left\{ \left(Y_1', Y_2'\right) \middle| \begin{array}{c} -0.09658 \le -0.9287Y_1' + 0.3622Y_2' \le 0.10342 \\ -0.03798 \le -0.3491Y_1' - 0.9068Y_2' \le 0.03202 \\ -0.00974 \le -0.1250Y'_1 - 0.1637Y_2' \end{array} \right\}$$

The target values of principal component covariance and y':

$$\Sigma_Y' = \begin{pmatrix} 0.0004839 & 0 \\ 0 & 0.0000299 \end{pmatrix}$$

T_Y'=(-0.0023，0.0037)'

The probability that the principal component satisfies the speification region:

$$P_1' = 0.99939$$

$$P_2' = 0.99936$$

The MCPI:

Mcp_2=1.1428

$MCpk_2$=1.139

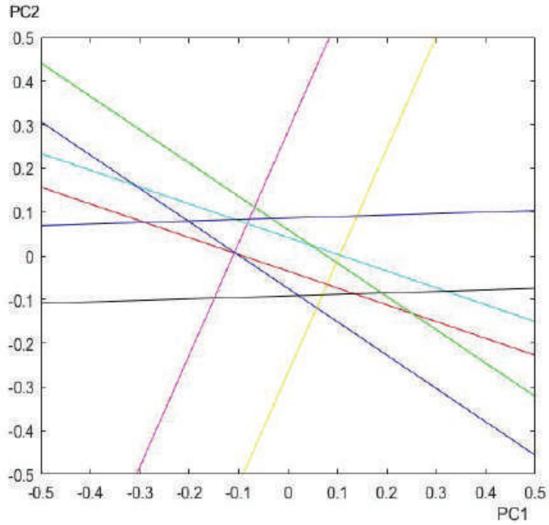

Figure 5 Revised specification area

The multi-process capability index should be less than the process capability index of any single quality feature. The potential process capability indices of the individual quality features X1, X2, X3, and X4 are calculated to be 1.62, 1.27, 1.13, and 1.002, so the multivariate process capability index should be less than 1.002.

In the example above, the potential MPCI with improved principal component contribution rate is 0.9748, and the potential MPCI of the traditional principal component method is 1.1428. The MPCI with improved principal component contribution rate is more realistic than the traditional principal component method. The analysis found that in the MPCI of the traditional principal component method, the variance of the quality feature X4 is smaller and the correlation is weaker than other quality features, so the contribution rate of the quality feature X4 is small and ignored (in the second section, it has been derived that the smaller the variance ratio and the weaker the contribution of the quality features, the smaller the contribution rate), resulting in MPCI being overestimated.

6. Conclusion

1) Through the theoretical analysis of the influence factors of the contribution rate of principal components, we found that the principal component contribution rate is determined only by the variance ratio and correlation coefficient between the quality features. Moreover, when one of them is constant, the contribution rate of the first principal component is positively linearly relative to another.

2) Based on the principal component method, we found

that the principal component contribution rate is not equivalent to the contribution rate of multivariate process capability practically. So, using the principal component contribution rate to directly evaluate the multivariate process capability is not reasonable or precise.

3) To solve the problem mentioned above, through normalizing the specification range of the processed quality features to [-1,1], eliminating the principal components with smaller variance to simplify the data. We proposed a method based on processing original data. Moreover, the rationality of the method is proved by an example.

References

[1] Juran J M, Gryna F M and Bingham R S. Quality Control Handbook. McGraw-Hill Higher Education 1974.

[2] Chan L K, Cheng SW and Spiring FA. A new measure of process capability: C_{pm}. Journal of Quality Technology 1988; 20(3): 162-175. https://doi.org/10.1080/00224065.1988.11979102

[3] Shahriari H, Hubele N and Lawrence F P. A multivariate process capability vector. Proceedings of the 4th industrial engineering research conference, Institute of Industrial Engineers 1995; 304-309.

[4] Wang S. X, Yeh. A. B. A spatial multivariate process capability index. IEEE International Conference on industrial Engineering &. En-gineering Management 2010; 1443-1445. https://doi.org/10.1109/IEEM.2010.5674321

[5] Wierda SJ. Multivariate quality control-estimation of the percentage of good products. The Netherlans: Dept. of Econometrics, University of Groningen 1992.

[6] Bothe D R. Composite capability index for multiple product characteristics. Quality Engineering 2000; 12(2): 253-258. https://doi.org/10.1080/08982119908962582

[7] Chen K S, Pearn W L and Lin P C. Capability measures for processes with multiple characteristics. Quality and Reliability Engineering lnternational 2003; 19(2): 101-110. https://doi.org/10.1002/qre.513

[8] Wang K F and Chen J C. Capability index using principal component analysis. Quality Engineering 1998; 11(1): 21-27. https://doi.org/10.1080/08982119808919208

[9] Wang F K and Du T C. Using principal component analysis in process performance for multivariate data. Omega International Journal of Management Science 2000; 28(2): 185-194. https://doi.org/10.1016/S0305-0483(99)00036-5

[10] MA Yizhong. Multivariate Quality Process Capability Index. Industrial Engineering 2001; 4(4)22-24.

[11] Wang Rang C H. Constructing multivariate process capability indices for short-run production. lnternational Journal of Advanced Man-ufacturing Technology 2005; 26 (11-12): 1306-1311. https://doi.org/10.1007/s00170-004-2397-8

[12] Shinde, R. L. and K. G. Khadse. Multivariate Process Capability Using Principal Component Analysis. Quality And Reliability Engi-neering International 2009; 25(1) : 69-77. https://doi.org/10.1002/qre.954

[13] Zhang, M., et al. Modified Multivariate Process Capability Index Using Principal Component Analysis. Chinese Journal of Mechanical Engineering 2014; 27(2): 249-259. https://doi.org/10.3901/CJME.2014.02.249

[14] Shahriari H, Abdollahzadeh M. A new multivariate process capability vector. Quality Engineering 2009; 21(3): 290-299. https://doi.org/10.1080/08982110902873605

[15] Jeh-Nan Pan and Chun-Yi Lee. New capability indices for evaluating the performance of multivariate manufacturing processes. Quality and Reliability Engineering International, 2010; 26(1): 3-15. https://doi.org/10.1002/qre.1024

Viser Technology Pte. Ltd.
Mechanical Engineering Science
https://doi.org/10.33142/me.v1i1.655

Research Article Open Access

Design of New Elevator Pressure Guide Plate and Its Test Device

Qihang Xu [1], **Shaoke Chen** [2*]

[1] Department of Machinery& Electric, Jieyang Vocational and Technical College, Jieyang, Guangdong, China
[2] Mechatronic and Electronic Engineering Department, Shantou University, Shantou, Guangdong, China

***Corresponding Author:** Shaoke Chen, 243 Daxue Road, Shantou, Guangdong, 515063, China; skchen@stu.edu.cn*

Abstract:
Pressure guide plate plays a certain role in the safe operation of elevator. Based on understanding the respective performance of new and old pressure guide plates, this paper analyses the problems existing in the original pressure guide plate. It also conducts stress analysis according to the function of pressure guide plate on elevator, and designs a new type of pressure guide plate combined with technological capability and equipment. According to the stress characteristics, a test device is designed and a comparative test is made between the new type of pressure guide plate and the old in order to test the reliability of the new type of pressure guide plate. The test proves that the new pressure guide plate of elevator can meet the requirements of product use and safe operation of elevator products.

Keywords: *Pressure guide plate; Test device; Guide rails; Elevator*

Citation: Q.H. Xu, S.K. Chen, Design of New Elevator Pressure Guide Plate and Its Test Device. *Mech Eng Sci*, 2019,1(1): 7-13. https://doi.org/10.33142/me.v1i1.655

1. Introduction

Because of the inconvenience of going upstairs and downstairs, elevators have always been the first choice for the public to solve this problem. However, in recent years, injuries caused by elevators have occurred from time to time. Thus, its safety is being questioned. In line with the enterprise mission of "providing safe, comfortable and fast delivery system for human beings", safety is put in the first place for elevator products.

Based on understanding the properties of new and old pressure guide plates, this paper analyses the problems existing in the original pressure guide plates. According to the function of pressure guide plate on elevator, a new type of pressure guide plate is designed, which combines process capability and equipment. According to the stress characteristics, the test device is designed to test the reliability of the new type of pressure guide plate to meet the requirements of the safe operation of elevator products [1].

2. Design and selection of new elevator pressure guide plate

2.1 Guide rails and pressure guide plate

Guide rails and pressure guide plate are important components of elevator guidance system. The guide rails provides guidance for the elevator's lifting motion and limits the horizontal movement of the carriage and counterweight [2]. Take the carriage as an example. Because the positions of people standing in the carriage after entering are not fixed, the carriage will incline due to the unbalance loading. The existence of the guide rails limits the occurrence of such excessive inclination, ensuring the stable operation of the carriage and reducing vibration.

Generally speaking, the guide rails are not fixed directly on the wall of the shaft, but on the guide rails bracket, as shown in Figure 1. In order to solve the problems of normal settlement, shrinkage of concrete and deviation of building, the commonly used fixing method is to fix the guide rails on the guide rails bracket with a pressure guide plate, and then connect the guide rails bracket with the pressure guide plate with bolts. The contact between the guide plate and the guide rails is a point contact. When the shaft sinks or the guide rails expand when hot and contracts when cold, and the tension force on the guide rails exceeds the compression force of the pressure guide plate, the guide rails can move relatively to avoid bending deformation [3]

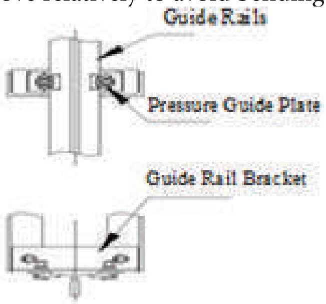

Figure 1. Fixed sketch of guide rails

2.2 New pressure guide plate structure

In elevator industry, the selection of pressure guide plate is generally based on experience. As the guide rails is a standard part, generally speaking, the specific types of guide rails have the corresponding pressure guide plates. A new type of pressure guide plate is designed in a step shape, as shown in Figure 2. The plate body is divided into three parts: front pressure surface, side pressure surface and support surface. The front pressure surface is used to hold down the guide rails. The side pressure surface is used to resist the side edge of the guide rails and reduce the inclination of the elevator. Compared with the old type of pressure guide plate, the side pressure surface of the new type is larger, which is conducive to increasing the stress area. A hole is set in the middle of the supporting surface, which is used to connect the guide rails bracket through the bolt. The upper part of the supporting surface is provided with a bolt locking groove, and the peripheral edge has a side opening. The other edges are inner hexagonal shape corresponding to the shape of bolt head. This shape is easy to install and helps to improve efficiency [4]. If the guide plate does not have such grooves, the top of the guide plate is flat. When installing, one wrench must be used to screw the head of the bolt, and another wrench must be used to tighten the nut. Both wrenches need to operate simultaneously. With a groove, the inner hexagonal shape of the groove is the same as a wrench to fix the bolt head. Therefore, the design of the groove improves the installation efficiency.

Compared with the old type of pressure guide plate (Figure 3) [5], the structure formed by the front pressure surface and the side pressure surface of the new type fits more closely with the side edge of the pressure guide plate. In use, it can reduce the possibility of micro-movement caused by carriage impact.

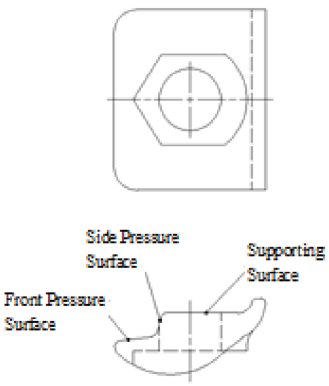

Figure 2. New pressure guide plate

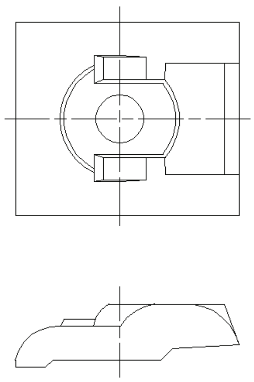

Figure **3.** Old pressure guide plate

3. Design of test device

3.1 Design thought of test device

The main function of the pressure guide plate is to limit the displacement of the guide rails in the horizontal direction. Therefore, its force comes from the guide rails. The following conditions exist when the guide rails is subjected to force:

1) The position of the passenger after entering the carriage is not fixed.

2) The cables and compensation chains suspended at the bottom of the carriage are not located at the center of gravity.

3) Because of some devices attached to the carriage (excluding cables and compensation chains), the center of gravity of the carriage is not in the central position.

The above reasons create a reversal trend for the carriage. Thus, they exert a certain force on the top and side of the guide rails.

The analysis shows that the pressure guide plate is subjected to the forces in the X and Y directions in the horizontal direction. Therefore, the main principle of the test device is to use a pendulum test (as shown in Figure 4), imitating the position of the guide rails in the shaft, fixed it on the guide rails bracket, and welded the guide rails bracket on the steel frame. At the same time, the gravitational potential energy of the heavy hammer is transformed into kinetic energy to produce the same amount of force as the theoretical analysis above, which indirectly acts on the guide rails. Then the verticality of the guide rails is measured to compare with the verticality of the guide rails specified in the national standard, to measure whether the new type of pressure guide plate can meet the requirements.

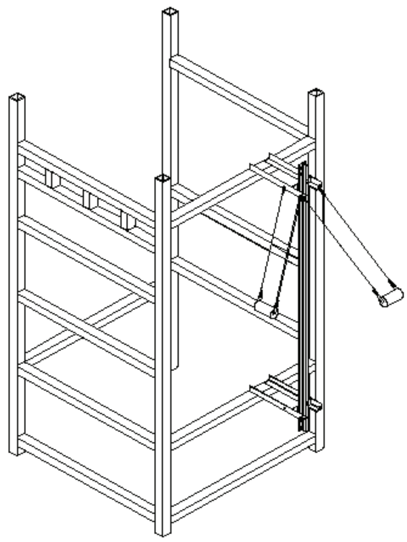

Figure 4. Schematic diagram of the test device

3.2 Force analysis of guide rails

The coordinate system of elevator guide rails specified in the national standard is shown in Figure 5. The guide rails is in the direction of x perpendicular to its side and y perpendicular to its top. When the top view of the carriage bottom is taken as an example (Figure 6), the direction of the opening of the carriage is x direction, and the horizontal direction of the other one is y direction [6].

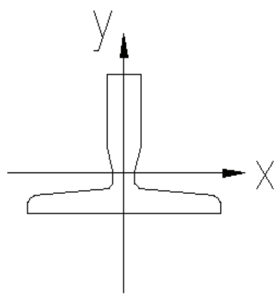

Figure 5. Guide rails coordinate system

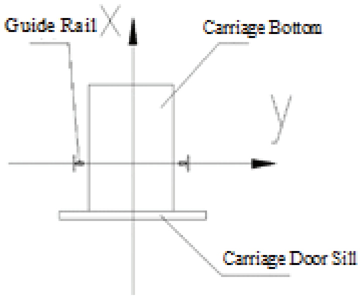

Figure 6. Carriage bottom coordinate system (View from Top)

3.2.1 Force analysis of guide rails in x direction

The joint force acting on the guide rails is divided into forces F_x and F_y in the direction of x and y by the method of orthogonal decomposition. This section begins with the calculation of F_x. Ideally, the guide rails is not stressed when the elevator is in normal operation. In fact, however, the load distribution of elevators is not even. When the front and rear forces of the carriage are uneven, there will be a reversal trend, which will cause a certain pressure on the guide rails. Especially when the safety clamp are in action, the pressure will be greater. The distribution of load when maximum pressure is exerted on the x-direction of the carriage guide is shown in Figure 7.

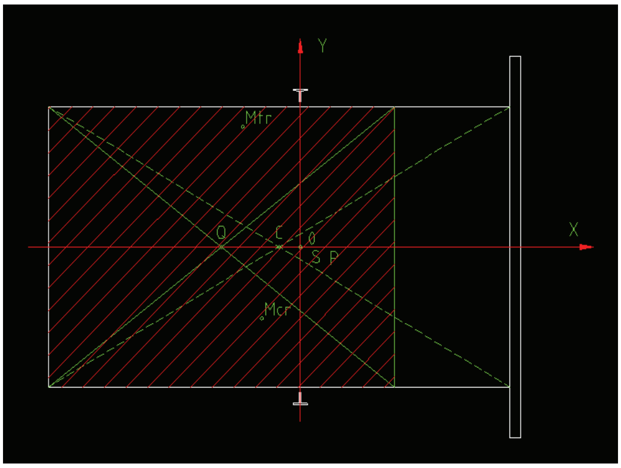

Figure 7. Distribution of gravity center of carriage bottom at maximum F_x

After measuring all the relevant data, the value of F_x can be calculated. According to the knowledge of torque calculation, when the safety clamp is in action, horizontal force F_x is produced by the front and rear torque of the carriage.

$$F_X = \frac{K_1 g_n \left(Q\cdot x_Q + m_{\mathrm{Mtr}}\cdot x_{\mathrm{Mtr}} + m_{\mathrm{Mcr}}\cdot x_{\mathrm{Mcr}}\right)}{nh} \quad (1)$$

In the formula:

K_1-- Impact coefficient, determined according to Table G2 on page 70 of Appendix G of GB 7588-2003. Take K_1=2.0;

—Standard gravity acceleration, 9.81m/s^2.

3.2.2 Force analysis of guide rails in y direction

Similarly, when the force is uneven between the left and right of the carriage, the overturning trend will result in the force F_y of the guide shoe on the guide rails. The steps are the same as those for solving F_x. However, it should be noted here is the gravity center when the carriage loads Q located 3/4 to the left of the carriage bottom (at this time, the pressure on the y direction of the guide rails is the greatest). The vertical force on the guide rails is when the carriage is overturned (see Figure 8).

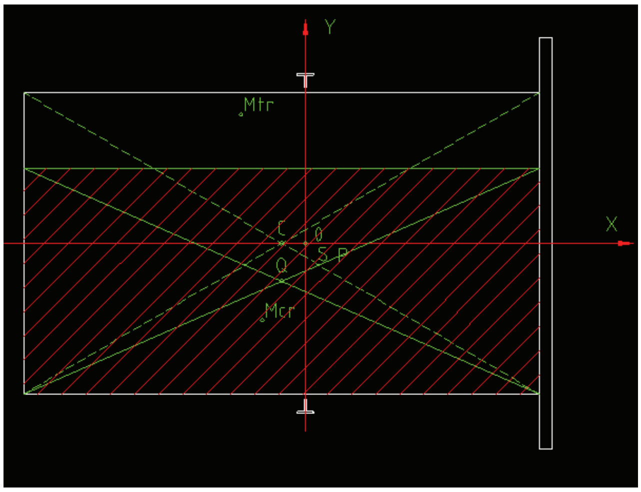

Figure 8. Distribution of gravity center of carriage bottom at maximum F_y

$$F_y = \frac{K_1 g_n \left(QY_Q - m_{\mathrm{Mtr}} Y_{\mathrm{Mtr}} + m_{\mathrm{Mcr}} Y_{\mathrm{Mcr}}\right)}{\frac{n}{2}h} \quad (2)$$

Formula has the same meaning as (1).

3.2.3 Determination of Fx and Fy

For the force on the guide rails in the x direction, assuming that the maximum load of the passenger elevator is 1600 kg, the carriage depth D_x=2400 mm, the carriage width D_y=1400 mm, and the carriage center of gravity P is also the suspension point S, the coordinate system is established for the origin. Then $(x_P, y_P) = (x_S, y_S) = (0, 0)$, carriage geometric center position (x_c, y_c) =(-110, 0), rated load gravity center position (x_Q, y_Q) =(-410, 0), traveling cable gravity center position (x_{Mtr}, y_{Mtr}) = (300, 600), compensation chain gravity center position (x_{Mcr}, y_{Mcr}) =(-200, -357), distance between guide shoe H = 3975 mm, guide shoe number n = 2, self-weight P = 1806 kg, compensation chain weight m_{Mcr} = 470 kg, traveling cable weight m_{Mtr} = 41 kg.

When the safety forceps are in action, the above data are put into formula (1) and the force on the guide rails at the stress point in the x direction is F_x≈2138N.

Similarly, for the force in the y direction at the stress point of the guide rails, except for the center of gravity of the rated load (x_Q, y_Q) =(-110, -175), other assumptions are the same. When the safety forceps are in action, the above data are put into formula (2) and the force on the guide rails at the point of force in the y direction is F_y=2089N.

3.3 Design of test device

3.3.1 Principle of Test Pendulum

The function of the pendulum is to produce a force that is the same as the theoretical analysis to impact the guide rails. The pendulum can be released from a certain height without initial velocity. According to the law of conservation of energy:

$$\mathrm{m}g_n\mathrm{H} = \frac{1}{2}mv^2 \quad (3)$$

Where:

m—Pendulum mass;

H—Pendulum drop height;

V—Velocity of the pendulum at its lowest point.

From the impulse theorem:

$$Ft=mv \tag{4}$$

Where:

F—The impulse of the pendulum on the guide rails;

t—The action time of the pendulum on the guide rails. Here t = 0.02s.

According to (3) (4), the required mass of the pendulum can be set, and then the drop height of the pendulum can be calculated. In addition, when testing the force condition, the selected measuring point should be the midpoint of the guide rails, because the deformation of the guide rails will be the largest at this time.

3.3.2 Design and calculation of guide rails bracket

The guide rails bracket structure of elevator carriage adopts Π-shaped structure, which belongs to statically indeterminate rigid frame. The original statically indeterminate structure is transformed into statically determinate structure, and unknown forces are added to the statically determinate structure. Then the displacement or deformation of statically determinate structures under the action of loads and unknown redundant forces at the redundant constraints are obtained to satisfy the constraints of the original statically indeterminate structures. The constraints are then transformed into supplementary equations with loads and unknown forces through physical equations. After solving these equations, unknown forces can be obtained, and other unknown forces can be obtained from static equilibrium equations [7].

In order to solve the displacement of guide rails support under the action of F_x and F_y alone, a unit force should be added at the action point of F_x and F_y at statically determinate base (where the transverse support is selected as statically determinate base). The unit bending moment diagrams M_{PFx} and M_{PFy} on statically determinate bases under unit force are also drawn (Figure 9 a) and Figure 9 b)).

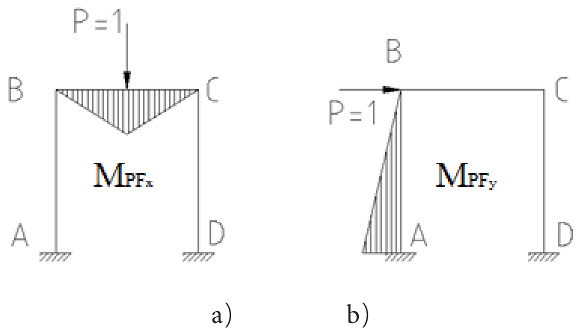

Figure 9. Unit load moment diagram

To solve the displacement of guide rails bracket under the action of F_y alone, the area of M_{PFy} can be multiplied by the coordinates of its centroid position corresponding to the load bending moment diagram of M_{Fy} load by graph multiplication [8].

$$\Delta F_y = 2\times\frac{1}{EI}\left\{\frac{1}{2}\times\frac{L}{2}\times\frac{L}{4}\times\left[\frac{2}{3}\times\left(\frac{F_y L}{4}-\frac{F_y L^2}{4(H+2L)}\right)-\frac{1}{3}\times\frac{F_y L^2}{(H+2L)}\right]\right\}=\frac{F_y L^3(2H+L)}{96EI(H+2L)} \tag{5}$$

Similarly, the displacement of guide rails bracket under the action of F_x alone can be obtained by graph multiplication.

$$\Delta F_x = \frac{1}{EI}\left\{\frac{1}{2}\times H\times H\times\left[\frac{2}{3}\times\frac{F_x H\ (3H+L)}{2(6H+L)}-\frac{1}{3}\times\frac{3F_x H^2}{2(6H+L)}\right]\right\}=\frac{F_x H^3(2H+2L)}{12EI(6H+L)} \tag{6}$$

4. Experiment and result analysis of test device

4.1 Testing device experiment

The pendulum is used to impact the guide rails according to the set height in turn, and the verticality of the guide rails is used as a benchmark to measure whether the pressure guide rails plate meets the requirements.

Mark the height to which the pendulum will be drawn with chalk on the cart and tie the other end of the pendulum to that height with a rope. Push the cart away until the rope is straightened. After adjusting the pendulum to align its impact plate with the side or top of the guide rails, use the tape to measure whether the gravity center of the pendulum to the ground meets the height requirement. If so, cut the rope with zero speed release and let the pendulum hit the test point. If the verticality of the guide rails after hitting exceeds the requirement of GB/T 10060-2011, it is necessary to readjust the verticality of the guide rails. Record the verticality value, and carry out the second pendulum impact test.

When recording the perpendicularity of the guide rails, the pendulum rope is hung above the guide rails. For the x direction, the deviation between the center of the upper guide rails and the weight line is marked as a value, the deviation between the center of the lower guide rails and the weight line is marked as value b, and the deviation between the guide rails and the weight line is marked as value a-b. For the y direction, the deviation between the top surface of the guide rails and the weight line is marked as value a, the deviation between the lower top surface of the guide rails and the weight line is marked as value b, and the deviation of the guide rails is marked as a-b (figs. 10 a), b)). At the same time, the marking fluid is used at the intersection of the pressure guide plate and the guide rails to confirm whether the guide rails displaces relative to the pressure guide plate after hitting.

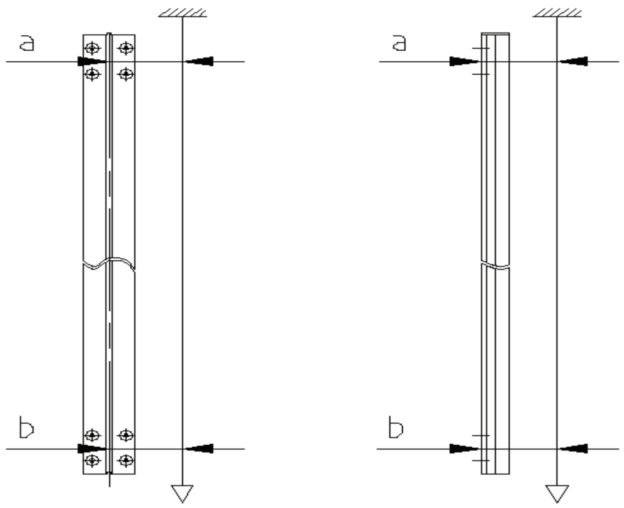

a) Measuring the Perpendicularity of the x-direction b) Measuring the Perpendicularity of the y-direction

Figure 10. Diagram of Verticality Measurement

4.2 Result Analysis

According to the test results, the verticality of x and y directions after impact is sorted out as follows:

According to the theoretical calculation, the double drop height is 711 mm, and the measured value of x-direction pendulum test of guide plate is shown in Table 1.

1) When the drop height is 3 times as high as 1422 mm, the measured values of x-direction pendulum test of guide plate are shown in Table 2.

2)According to the theoretical calculation, the double drop height is 679 mm, and the measured value of y-direction pendulum test of guide plate is shown in Table 3.

3) When the drop height is 3 times as high as 1358 mm, the measured values of y-direction pendulum test of guide plate are shown in Table 4.

The verticality data of the guide rails tested in the table are represented by a line chart, as shown in Figure 11.

Table 1. Measured value of x-direction pendulum test of guide plate at 711 mm drop height

Pressure guide plate type	Sequence		a(mm)	b(mm)	a-b（mm)
New Pressure Guide Plate	First Time	Initial Value	35.00	34.90	0.10
		After Impact	35.06	34.92	0.14
		Change Value	0.06	0.02	0.04
	Second Time	Initial Value	35.06	34.92	0.14
		After Impact	35.14	34.92	0.22
		Change Value	0.08	0.00	0.08
Old Pressure Guide Plate	First Time	Initial Value	35.68	35.37	0.31
		After Impact	35.77	33.54	2.23
		Change Value	-0.09	1.83	1.92
	Second Time	Initial Value	35.60	35.39	0.21
		After Impact	35.68	32.82	2.86
		Change Value	-0.08	2.57	2.65

Table 2. Measured value of x-direction pendulum test of guide plate at 1422 mm drop height

Pressure guide plate type	Sequence		a(mm)	b(mm)	a-b（mm)
New Pressure Guide Plate	First Time	Initial Value	39.66	39.44	0.22
		After Impact	37.56	36.50	1.06
		Change Value	-2.10	2.94	0.84
	Second Time	Initial Value	38.20	37.96	0.24
		After Impact	37.12	35.02	2.10
		Change Value	-1.08	2.94	1.86
Old Pressure Guide Plate	First Time	Initial Value	35.78	35.42	0.36
		After Impact	35.68	27.26	8.42
		Change Value	0.10	8.16	8.06
	Second Time	Initial Value	35.68	35.42	0.26
		After Impact	35.82	27.58	8.24
		Change Value	-0.14	7.84	7.98

Table 3. Measured value of y-direction pendulum test of guide plate at 679 mm drop height

Pressure guide plate type	Sequence		a(mm)	b(mm)	a-b（mm)
New Pressure Guide Plate	First Time	Initial Value	40.32	40.28	0.04
		After Impact	40.32	40.28	0.04
		Change Value	0.00	0.00	0.00
	Second Time	Initial Value	40.32	40.28	0.04
		After Impact	40.32	40.28	0.04
		Change Value	0.00	0.00	0.00

Pressure guide plate type	Sequence		a(mm)	b(mm)	a-b（mm)
Old Pressure Guide Plate	First Time	Initial Value	41.00	41.00	0.00
		After Impact	41.00	40.92	0.08
		Change Value	0.00	-0.08	0.08
	Second Time	Initial Value	41.00	40.92	0.08
		After Impact	41.02	40.88	0.14
		Change Value	0.02	-0.04	0.06

Table 4. Measured value of y-direction pendulum test of guide plate at 1358 mm drop height

Pressure guide plate type	Sequence		a(mm)	b(mm)	a-b（mm)
New Pressure Guide Plate	First Time	Initial Value	41.50	41.30	0.20
		After Impact	41.50	41.32	0.18
		Change Value	0.00	0.02	-0.02
	Second Time	Initial Value	41.50	41.32	0.18
		After Impact	41.52	41.32	0.20
		Change Value	0.02	0.00	0.02
Old Pressure Guide Plate	First Time	Initial Value	40.32	40.00	0.32
		After Impact	40.32	40.04	0.28
		Change Value	0.00	0.04	-0.04
	Second Time	Initial Value	40.32	40.04	0.28
		After Impact	40.33	40.03	0.30
		Change Value	0.01	-0.01	-0.02

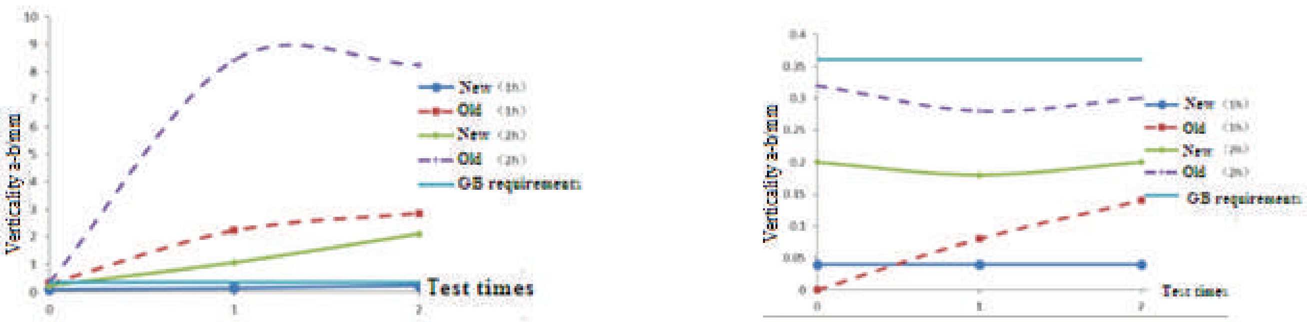

a) Verticality x-direction of guide rails test   b) Verticality y-direction of guide rails test

Figure 11. Verticality of guide rails test

By comparing the verticality charts above, it can be seen that the verticality of data display is within the requirement when measuring the verticality of y direction of both new and old pressure guide plates. This can be mainly attributed to the support function of the rear guide bracket. In addition, the pressure guide plate will not be loosened or collapsed after the y-axis of the guide is hit forward. For the x direction, the verticality of the guide rails under the action of two kinds of pressure guide plates has changed obviously, and both of them are in the state of increasing. By comparison, the following two points can be drawn:

1) After impact, the verticality guaranteed by the new type of pressure guide plate is much higher than that of the old type of pressure guide plate. Even if the guide plate is impacted at 3 times the height, the verticality guaranteed by the new type of pressure guide plate is much higher than that of the old type when the guide plate is impacted at double the height.

2) When the pressure guide plate is tested by double height, the verticality of the new type of pressure guide plate is within the prescribed range. However, the verticality of the two types of pressure guides exceeded the requirement after the test was carried out at 3 times the height. Especially the verticality value a-b of the old type pressure guides was much higher, which far exceeding the national standard.

5. Conclusion

Pressure guide plate plays a certain role in the safe operation of elevator. According to the requirements of safe operation of elevator products and the shape and structure performance of the guide rails, a new type of pressure guide plate is designed and selected in this paper. At the same time, a test device is designed for testing. Through the test, it has been verified that the verticality of the guide rails guaranteed by the new type of pressure guide plate meets the requirements of the national standard when the height is 2 times as high. It not only meets the requirements, but also reduces the cost by two-thirds compared to the old pressure guide plate.

Acknowledgments: The authors wish to thank the special funds for scientific and technological innovation and development in Jieyang, Guangdong (No. 2017xm052) for this project.

References

[1] SHENG Shichao. Design and Installation of Elevator Locking Device. Equipment Manufacturing Technology [J].2014; 3:194-200.

[2] Zheng wei. Discussion on Installation Quality Detection Technology of Elevator Guide rails Support. Technology Innovation and Application [J]. 2017; 5:100.

[3] Deng yahua. Research on the Connecting Structure of Elevator Guide rails. Science and Technology [J]. 2015; 17:144.

[4] Piotr Gołuch, Janusz Kuchmister, Kazimierz Ćmielewski, et al. Multi-sensors measuring system for geodetic monitoring of elevator guide rails. Measurement [J]. 2018; 130:18-31. https://doi.org/10.1016/j.measurement.2018.07.077

[5] Kai Wang, Baoyu Wang, Chuancheng Yang. Research on the Multi-Step Straightening for the Elevator Guide Rail. Procedia Engineering [J]. 2011; 16: 459-466. https://doi.org/10.1016/j.proeng.2011.08.1111

[6] Liu jinyuan. Discussion on Installation and Inspection of Elevator Guide rails Support. China High-Tech Enterprises [J]. 2017; 11:128-129.

[7] National Elevator Standardization Technical Standards Committee. GB/T 22562-2008 Elevator Type T guide rails[S]. Beijing: Standards Press of China, 2008.

[8] Yu chunze. Elevator design calculation and example [M]. Beijing: China Elevator Magazine.2011.

Viser Technology Pte. Ltd.
Mechanical Engineering Science
https://doi.org/10.33142/me.v1i1.656

Research Article Open Access

Study on Surface Roughness in Micro Milling of Single Crystal Materials

Qi Gao*, Po Jin, Guangyan Guo

School of Mechanical Engineering & Automation, Liaoning University of Technology, Jinzhou,121001,China.

***Corresponding Author:** Qi Gao, E-mail address: qqonline@163.com*

Abstract:
Micro milling is a machining method of high precision and efficiency for micro components and features. In order to study the surface quality of single crystal materials in micro milling, the two-edged cemented carbide tool milling cutter with 0.4 mm diameter was used, and the orthogonal experiment was completed on the micro-milling of single crystal aluminum material. Through the analysis of statistical results, the primary and secondary factor which impacting on surface quality were found as follows: spindle speed, feed rate, milling depth. The ideal combination of optimized process parameters were obtained, when the spindle speed was 36000 r/min, the milling depth was 10 μm, the feed rate was 80 μm/s, which made the milling surface roughness is 0.782 μm and minimal. Single crystal materials removal mechanism were revealed, and the influence of cutting parameters on micro-milling surface were discussed, the reason of tool wear was analyzed. Those provide a certain theoretical and experimental basis for micro milling of single crystal materials.

Keywords: *Surface roughness; Micro milling; Single crystal materials; Orthogonal experiment*

Citation: Q. Gao, P. Jin, G. Guo, Study on Surface Roughness in Micro Milling of Single Crystal Materials. *Mech Eng Sci*, 2019,1(1): 14-17. https://doi.org/10.33142/me.v1i1.656

1. Introduction

Micro milling refers to the cutting technology of precision machining of micro parts with micro milling cutters. The diameter in micro milling cutter is usually less than 1 mm [1].The size of cutter and workpiece are not reduce by macro-size in the process of micro micro-cutting, the cutting edge radius and the cutting depth are in the same order of magnitude. The cutting edge radius of the tool has obvious influence on the minimum cutting thickness, size effect and chip formation. The radius of cutting tool edge has obvious influence on the minimum cutting thickness and chip formation, and the conventional cutting mechanism is no longer applicable in the micro machining [2-4]. Through a lot of test to prove that: The micro-milling mechanism is very different from the traditional milling mechanism in cutting conditions, system stiffness, cutting parameters and so on [5-7]. In order to ensure the surface quality and accuracy of the parts, it is necessary to adopt appropriate milling methods, cutting parameters and machining conditions.

Scholars at home and abroad have studied the micro milling of single crystal silicon, copper and polycrystalline alloys. Sato et al. [8] put forward the scale effect in the micro cutting experiment of aluminum alloy. Lucca et al. [9] found the phenomenon of ploughing and scratching in the small cut depth experiment. Damazo [10] and Schaller [11] put forward the ways to solve the burr in the micro cutting test of copper, stainless steel and cast iron. But it's rarely reported both at home and abroad for micro milling of the single crystal aluminum. Tool geometric parameters, tool wear and tool vibration are many factors that will have an impact on the surface quality and the machining system. In this paper, the micro milling process of single crystal aluminum was studied by means of orthogonal experiment, the reasonable micro milling process was optimized through range and variance analysis, and the mechanism of micro milling and the reasons affecting surface roughness are analyzed.

2. Experiment on micro milling of single crystal aluminum

2.1 Experimental condition

As shown in Figure 1(a), The micro milling experiment was carried out on the JX-1 platform, which is equipped with NSK pneumatic spindle, and its working stroke of X axis is 490 mm, Y axis is 490 mm and Z axis is 120 mm respectively. The maximum spindle speed is 60000 r/min, and the radial and axial runout degree of the spindle is less than 0.1 μm and the repeat positioning accuracy is ±0.2 μm; As shown in Figure 1(b), VHX-1000E microscope is used to observe the surface morphology; As shown in Figure 1(c), The surface roughness of the microgroove bottom was measured by STIL laser 3D profile instrument, the measuring accuracy is 0.001 μm, and the measuring range is 0.02-20 μm; As shown in Figure 1(d), the cutter was M.A.FORD uncoated cemented carbide spiral cutter, the cutter diameter is 0.4 mm, the handle diameter is 3 mm, the length of cutter blade is 1.2 mm, and the cutter length is 38 mm.

(a) JX-1 Machine platform

(b) VHX-1000E Microscope

(c) STIL Profilomete

(d) Micro Milling Cutter

Figure 1 Micro milling experimental equipment and cutter

2.2 Experimental scheme

In this experiment, three factors and five levels of orthogonal test are used, namely $L_{25}(5^3)$. Factors set are mainly these cutting parameters which have main effect on cutting quality, namely, the three factors are the spindle speed n, the axial milling depth a_p and the feed rate v. Because the blade diameter of the micro milling cutter is very small, and the maximum speed of machine is 60000 r/min, in order to obtain higher surface accuracy, so the spindle speed was selected in the 12000-48000 r/min equally, that is the spindle speed must be increased; Smaller cutter blade diameter can be easily machined damage, considering the influence of vibration and the minimum cutting thickness, the cutting parameter set strive to smaller, and the milling depth uniform distributed between 5-15 μm, and the feed rate uniform distributed between 20-100 μm /s.

3. Experimental results and analysis

3.1 Experimental data

According to the factors and levels of the orthogonal experiment, the orthogonal experimental table and the corresponding roughness value were established by the micro milling experiment of single crystal aluminum, as shown in table 1.

3.2 Range and Variance analysis

According to the data in table 1, calculating the range R and variance V, the results of data processing were shown in table 2.

The range and variance chart of the surface roughness of single crystal aluminum under three kinds of cutting parameters were shown in Figure 2 We can see from the chart, the spindle speed range was the biggest, the feed rate secondly, and the milling depth is the minimum, thus what can be concluded is that the primary and secondary order was spindle speed> feed rate >milling depth that influenced surface roughness. The optimized combination of process is: when the spindle speed is 36000 r/min, the milling depth is 10 μm, and the feed rate is 80 μm/s, the minimum surface roughness and the best surface quality can be got. The scheme was repeated three times, and the surface roughness value is 0.782μm. By comparing the results, the scheme was the optimal and optimization, and the least roughness.

Table 1 Experimental data of the single crystal Al

Experimental Number	n (r/min)	a_p (μm)	v (μm /s)	R_a (μm)
1	12000	5	20	1.03
2	12000	8	40	0.992
3	12000	10	60	0.955
4	12000	12	80	0.962
5	12000	15	100	1.13
6	24000	5	40	1.02
7	24000	8	60	0.954
8	24000	10	80	0.998
9	24000	12	100	0.994
10	24000	15	20	0.946
11	36000	5	60	0.949
12	36000	8	80	0.880
13	36000	10	100	0.800
14	36000	12	20	0.929
15	36000	15	40	1.07
16	42000	5	80	0.863
17	42000	8	100	0.986
18	42000	10	20	1.03
19	42000	12	40	1.05
20	42000	15	60	0.889
21	48000	5	100	0.980
22	48000	8	20	1.01
23	48000	10	40	0.942
24	48000	12	60	1.04
25	48000	15	80	1.02

Table 2 Calculated Results of Single Crystal Aluminum Surface Roughness

Processing Number	n	a_p	v
K_{1j}	5.069 (1.014)	4.842 (0.968)	4.945 (0.989)
K_{2j}	4.912 (0.982)	4.822 (0.964)	5.074 (1.015)
K_{3j}	4.628 (0.926)	4.725 (0.945)	4.787 (0.957)
K_{4j}	4.878 (0.964)	4.975 (0.995)	4.723 (0.945)
K_{5j}	4.992 (0.998)	5.055 (1.011)	4.890 (0.978)
K_{1j}^2	25.695	23.445	24.453
K_{2j}^2	24.128	23.252	25.745
K_{3j}^2	21.418	22.326	22.915
K_{4j}^2	23.213	24.751	22.301

Processing Number	n	a_p	v
K_{5j}^2	24.920	25.553	23.912
R	0.441	0.330	0.351
T		24.419	
CT		23.852	
SS	0.0228	0.0134	0.0132
V	0.00570	0.00335	0.00330

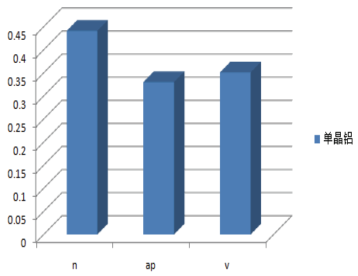

(a) Range chart

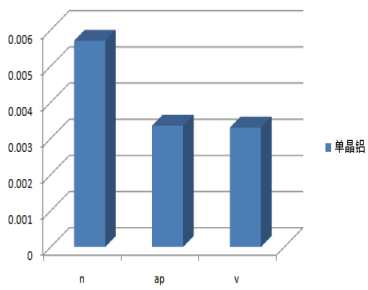

(b) Variance chart

Figure 2 Range and variance chart of the influence of each factor on surface roughness

3.3 The influence of process parameters on the surface roughness

In order to study the influences of various factors on the single crystal aluminum surface roughness, averaged the summation of the data corresponding to each level of each column, as shown in table 2, the broken line graph of the three factors such as spindle speed, milling depth and feed rate that effects on surface roughness were drawn, as shown in Figure 3.

(1) The effect of spindle speed on Ra

As shown in Figure 3 (a), the surface roughness of micro milling groove was first decreased and then increased with the increase of spindle speed, the turning point was 36000 r/min. When the spindle speed is less than 36000 r/min, the effective friction between the chip and the front tool surface decreases with the increase of the spindle speed, thus the chip deformation time was shortened, and chip was cut from the workpiece instantly. Most cutting heat was taken away by the chip. Small friction reduced cutting force and the possibility of producing tumor, and improved the processing precision of single crystal material. When the spindle speed was greater than 36000 r/min, Due to the lack of rigidity of the system, the spindle produces certain vibration that made the cutter wear with the spindle speed continues to increase. The cutting heat cannot be taken away in time, so that the surface quality would become worse.

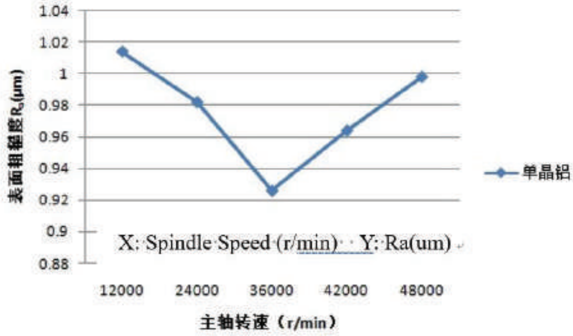

(a) Influence of Spindle Speed on Ra

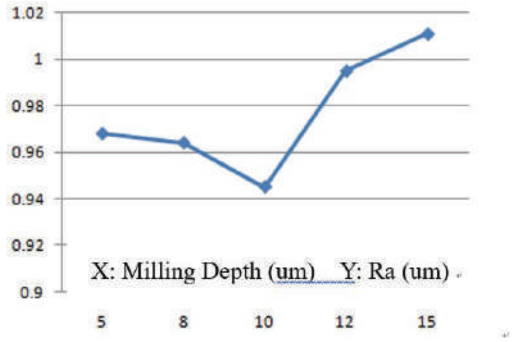

(b) Influence of Milling Depth on Ra

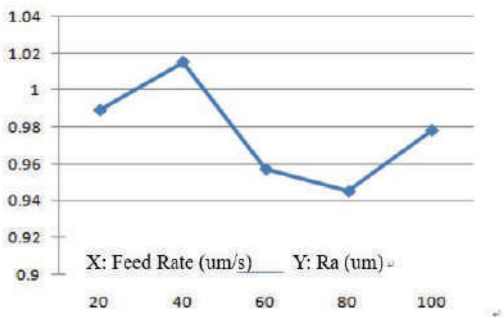

(c) Influence of Feed Rate on Ra

Figure 3 Influence of each factor on surface roughness

(2) The effect of milling depth on Ra

As shown in Figure 3 (b), the surface roughness of micro milling groove decreased first and then increased with the increase of milling depth, and the turning point is 10 μm, the roughness is the minimum. When the milling depth was lesser, the milling process was not easy to produce cutting, the cutter produced squeeze and slippage, and thereby the surface roughness was degraded. When the milling depth was greater than 10 μm, the amplitude of the cutting force increased with the increase of the milling depth, which resulting in deformation and cutting vibration of workpiece and tool, and causing a significant increase in surface roughness.

(3) The effect of feed rate on Ra

As shown in Figure 3(c), the surface roughness of micro milling groove increased first and then decreased and then increased with the increase of feed rate. Due to the exist of minimum chip thickness, when the feed rate is less than 40 μm/s, the feed per tooth is less than the minimum cutting thickness, and the milled surface was mainly caused extrusion and ploughing, and thereby the milling force was increased and surface roughness was became bigger. When the feed per tooth is greater than the minimum cutting thickness, the surface roughness decreases at first and then increases. When the feed is greater than 80 μm/s, increasing the feed rate can improve the machining efficiency, increase the residual area height, and directly lead to the increase of surface roughness.

4. Micro Milling Cutter Wear

Single crystal aluminum belongs to the plastic removal material. Through 25 groups of micro milling experiments and observed by superfield depth microscope, the micro-milling blade used in the experiment has a certain amount of wear and tear, by the observation of microscope with super field depth, as shown in Figure 4, the cutting edge radius was 0.97 μm before processing, and the cutting edge radius was 2.65 μm after wearing. It can be seen that the wear of cutter nose and grooves in the cut deep direction were the main forms of failure. In the micro milling process, a lot of heat and shear stress were generated in the deformation zone, and the cutter was easy to cause failure because of the adhesive softening, blade deformation and hot tearing. In milling process, with the increase of cutter wear, the cutter edge radius would increase sharply, and the milling force and the friction coefficient increases, and the machine trembled, thus degrading the surface roughness. Therefore, in the milling of difficult machining materials, cutting tools should be replaced in time to reduce the influence of tool wear on workpiece quality.

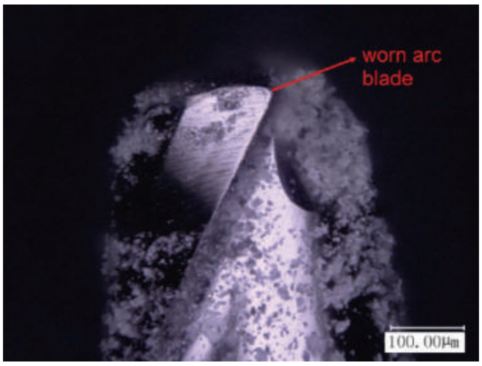

Figure 4 Worn Cutter

5. Conclusions

(1) The cemented carbide micro milling cutter with 0.4mm diameter was used for the micro milling of the single crystal aluminum by three factors and five levels orthogonal experiment. The primary and secondary factors that affect the processing surface roughness were as follows: spindle speed, feed rate, milling depth.

(2) Through the range and variance analysis and the optimized process scheme, when the spindle speed was 36000 r/min, the milling depth was 10 μm, the feed rate was 80 μm/s, the minimum surface roughness can be obtained and its value is 0.782 μm.

(3) Because of the low stiffness of the micro milling cutter, the worn cutter had a certain effect on the micro milling surface roughness. Under appropriate conditions, the cutters should be replaced to ensure the processing quality of parts.

Acknowledgment: The authors would like to thank the support of the Doctoral Start-up Fund of Liaoning Province (2019-BS-123) and Liaoning University of Technology (XR2018003).

References

[1] Wang J , Gong Y , Shi J , et al. Surface roughness prediction in micro milling using neural networks and Taguchi's design of experiments[C]. IEEE International Conference on Industrial Technology. IEEE, 2009. https://doi.org/10.1109/ICIT.2009.4939525

[2] Gong Y D, Huang X J, Wen X L, et al. Experimental Research on Wear Mechanism of Micro-grinding Tool in Grinding Soda-Lime Glass[J]. Journal of Northeastern University, 2017, 38(8):1128-1132.

[3] Kai E, Hosono S, Takemoto S, et al. Fabrication and cutting performance of cemented tungsten carbide micro-cutting tools[J]. Precision Engineering, 2011, 35(4):547-553. https://doi.org/10.1016/j.precisioneng.2011.06.002

[4] Sun Z, To S. Effect of Machining Parameters and Tool Wear on Surface Uniformity in Micro-Milling[J]. Micromachines, 2018, 9(6):268-279. https://doi.org/10.3390/mi9060268

[5] Dadgari A , Huo D , Swailes D . Investigation on tool wear and tool life prediction in micro-milling of Ti-6Al-4V[J]. Nanotechnology and Precision Engineering, 2018, 1(4):218-225. https://doi.org/10.1016/j.npe.2018.12.005

[6] Saptaji K, Subbiah S, Dhupia J S, et al. Effect of side edge angle and effective rake angle on top burrs in micro-milling[J]. Precision Engineering, 2012, 36(3):444-450. https://doi.org/10.1016/j.precisioneng.2012.01.008

[7] Gao Q , Chen X . Experimental research on micro-milling force of a single-crystal nickel-based superalloy[J]. The International Journal of Advanced Manufacturing Technology, 2019, 102(1-4):595-604. https://doi.org/10.1007/s00170-018-03211-x

[8] Sato M, Yamazaki T, Shimizu, et al. A study on the microcutting of aluminum single crystals[J]. JSME International Journal Series III, 1991,34(4): 540-545. https://doi.org/10.1299/jsmec1988.34.540

[9] Lucca D A, Seo Y W. Aspects of surface generation in orthogonal ultraprecision machining [J].CIRP Annals, 1994, 43:43-46. https://doi.org/10.1016/S0007-8506(07)62160-X

[10] Damazo B N, Davies M A, Dutterer B S, Kennedy M D. A sμmmary of micro-milling studies[C]. First International Conference of the European Society for Precision Engineering and Nanotechnology, 1999(20):322-324.

[11] Schaller T, Bohn L, Mayer J, Schubert K. Microstructure grooves with a width of less than 50μm cut with ground hard metal micro end mills. Precision Engineering[J], 1999(23): 229-235. https://doi.org/10.1016/S0141-6359(99)00011-2

Viser Technology Pte. Ltd.
Mechanical Engineering Science
https://doi.org/10.33142/me.v1i1.657

Research Article Open Access

Design and Selection of Servomotor for Radial Aircraft Tire Secondary Molding Machine

Chaoqun Wang

Qingdao Double Star Tire Co., Ltd., Qingdao 266400, China

Abstract:
The company Meridian Air Tire using two method molding, molding machine transmission components design selection using mitsubishi J4 series servo motor and control system. Among them, the two-segment host pitch and rotary servo motor selection is the most typical, this paper on its design ideas and selection of a detailed discussion, for manufacturers to correctly select servo motor to provide reference.

Keywords: *radial air tires; two-stage shaping host; servo motor; selection optimization*

Citation: C.Q. Wang, Design and Selection of Servomotor for Radial Aircraft Tire Secondary Molding Machine. *Mech Eng Sci*, 2019,1(1): 18-26. https://doi.org/10.33142/me.v1i1.657

Introduction

Meridian Air Tire Molding machine is the key equipment for the manufacture of air tires, which is usually formed by two methods. In the process of molding machine design and manufacture, the precision positioning, rapid feedback and cycle control of molded semi-finished rubber parts are required, and the main application parts are: A section of host rotation, two segments with beam layer bondingdrum rotation, two section footwear winding head lifting and panning, Two segment host pitch and rotation, host rear pressure rotation/advance and retreat/division, etc. Among them, the two-segment host pitch and rotary servo motor selection is the most typical, the following on its design ideas and selection methods to discuss.

1 process flow and equipment structure principle

Company 16~20 Inch radial air tire two-time molding machine consists of a section of molding machine and two-segment molding machine. A molding machine is used for molding aeronautical meridian Fetal Body, the main adhesive components include lining layer, fiber cord body, wire ring, tire side, filler glue, shoulder pad glue, wear-resistant adhesive and body coating, curtain reinforcement layer, etc.; two-stage molding machine with beam layer bonding drum forwinding beam layer, bonding corrugated protective layer, FittingTire surface and other adhesive parts, Two-stage molding machine shaping drum adoption no capsule drum, by the left and right two chucks respectively installed in the molding machine spindle, external bushings on the chuck composition.The joint area is fitted with a PU ring to prevent compressed air leakage during training. The following focuses on the two-segment fetal billet shaping process and equipment structure principle.

1.1 Process Flow

In the two section of the host training drum, a section of the molding machine molded a good tire body in the adjustment of a flat width of the shaping chuck, the shape of the bulging drum rise, chuck lock the body mouth part. Compressed air through the molding machine hollow spindle to inflate the body, while the spindle pitch servo motor rotation, through the ball screw to drive the two cards to the middle of the closing, so that the body inflatable shaping, the formation of the basic outline of the tire. Then, the transmission ring will be clamped tread/belt layer composite parts transmitted and fitted to the surface of the tread, the spindle rotation, at the same time through the tread pressure roller,tire shoulder pressure roller, rear pressure roller combination rolling, the body, The composite parts with bundles are closely attached to the surface of the tread, and the tread is shaped and finished. After shaping and rolling, the gas in the fetus is discharged, the tire billet is detached from the shaping Chuck, and the tire billet is removed by the transfer ring. The entire training process processes are as follows:

The chuck is divided into a flat width → placement of fetal body→ The stereotype drum rise → low pressure inflatable→ The chuck closes to the predetermined type →Transfer ring right shift → high pressure inflatable→ chuck closed to styling position, ultra-shaping position →Transfer ring relaxation→Transfer ring left shift → tread, tire shoulder, rear pressure roller combination rolling→ Passing ring discharge tire

During the training process, the tire body inflatable pressure gradually increased, from 0.05MPa,0.1Mpa finally reached 0.18MPa, the center line of the placenta does not move, the side of the fetal ring symmetrical shrinkage, Inflatable, fetal coil shrinkage, fetal expansion synchronized, the center line of the placenta and tread/belt layer composite parts of the center line coincide, each glue parts through the rear pressure combined pressure roller rolling tightly fit to form the shape of the fetal billet.

1.2 Principle of equipment structure

Two segment molding machine host pitch, rotation diagram as shown in Figure 1(overlooking):

1.2.1 shaping distance mechanism

Two segment molding machine host pitch implementation process is: Mitsubishi HG-SR Series servo motor with MOTOREDUCE brand VB series Planetary reducer1 (Motor reducer under the spindle, the diagram will be removed from the motor, indicated by a dotted line) rotation, motor sprocket2 drive sprocket8, two sprocket8 Installed on two bidirectional ball screws, two bidirectional screw horizontal placement, front right spin, back end left, two pieces supporting screw nut12,13 Installing external bushings separately14 rear end Front bracket 11 upper and spindle 4 back end the rear bracket 9 On.

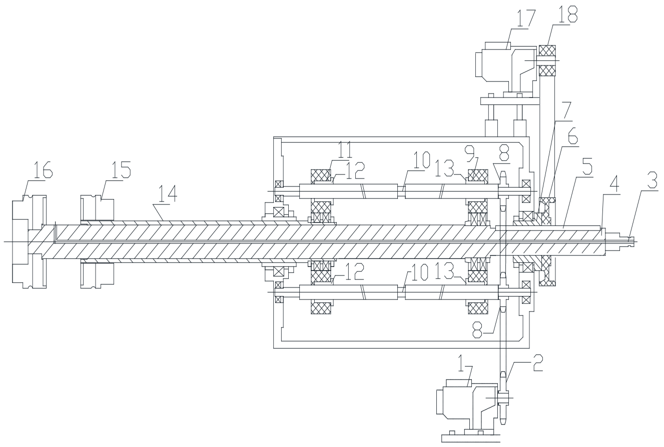

1-distance servo motor, reducer; 2-motor sprocket; 3-rotary joint; 4-spindle; 5-guide key; 6-large synchronous belt wheel; 7-guide seat; 8-ball screw sprocket; 9-ball screw rear bracket; 10-left and right ball screw; 11-ball screw front bracket; 12-Front ball screw Nut ; 13-rear ball screw nut; 14-outer bushing; 15-right Chuck; 16-left chuck; 17-Rotary servo motor, reducer; 18-small Synchronous belt wheel

Figure 1: two segment molding machine host pitch, rotation diagram

When the distance servo motor is turning in the direction, driving the sprocket 8, the ball screw is rotated with the same turn, at this time, two front right-handed ball screws push the outer bushing14 Flattening shift, install the right chuck at the front end of the outer bushing15 and pan forward at the same time; two rear left spin ball screws pull the spindle back and pan, mounted on the front end of the spindle left chuck16 pan backward at the same time. The two cards are panned in opposite directions, and the tire billet pitch is shaped. When the shaping servo motor rotates in the opposite direction, driving the sprocket8, the ball screw 10 is rotated with the same turn, two front right-handed ball screws pull the outer bushing14 pan backward, right chuck15 at the same time pan backward; two rear left spin ball screws push the spindle forward to pan, left chuck 16 pan forward at the same time. Two card disk back translation, to carry out the training drum adjustmentlevelingwide work.

1.2.2 host rotating mechanism

Two segment molding machine host rotation execution process is: Mitsubishi HG-SRSeries servo motor with MOTOREDUCE brand VB series Planetary reducer17, the motor synchronous belt wheel18 drive the spindle synchronous belt wheel 6 rotation. Thespindle 4 is supported by the bearing of the front seat and rear seat of the chassis, and the rear bearing is mounted on the guide seat7, and thesynchronous belt wheel 6 is fixed on the guide seat, the guide seat7and the spindle4 are connected by the guide key5, and the spindle is in the guide groove make axial movement and drive torque through the key. The spindle4 and the outer bushing14 also have a guide key connection when the rotating servo motor rotates, driving the spindle4 , outer bushing14, shaping drum15/16, The fetal billet rotates together, and the combined rolling action is carried out.

Spindle 4 and outer bushing14 have guide key connection, can carry on the left and right relative translation movement, rotate together when rotating; spindle4and guide seat7 also has the guide key join, can carry on the left and right relative translation movement, rotates together when rotating.

2 Design selection process

2.1 Existing problems and preliminary verification and servo motor selection conditions in question

After the Air Meridian two section molding machine is put into production and applied, the servo motor has several overload alarm phenomena in the process of pitch setting and rotary rolling, and the power of servo motor is judged preliminarily by empirical method and analogy method. First, based on the principle of investment minimization, the following verification is carried out:

2.1.1 Preliminary verification

(1) The host rotary servo motor, REDUCER (Mitsubish HG-SR502J 5KW,reducerVB-DR-140-005-S2-P1, speed ratio 1:5) with pitch servo motor (MitsubishiHG-SR352J 3.5KW,reducerVB-DR-180-010-S2-P1, Speed ratio1:10) Installation position interchange,at the same time the control system servo drive, cable, connector replacement, modify PLC control procedures, still appear pitch motor , rotating motor have overload alarm phenomenon.

Only consider the motor, reducer situation, the preliminary reasoning is as follows:

By formula:

$$T = \frac{9550\ P}{N_e \times i \times \eta} \tag{1}$$

T--rated torque in formula Nm

P-- rated power KW

N_e --rated speed r/min

i --deceleration ratio

η--reducer transmission efficiency, checkVB-140/VB-180 Series Reducer samples, its efficiency are above 95%.

Rated output torque in the non-braking, the same rated speed (2000r/min), the host pitch replacement motor, reducer after the output torque reduction, easier overload alarm, the host rotation replacement servo motor, reducer, improper selection, overload alarm.

(2) Adjust 2 sets of motors and gearboxes back to the original installation position, the distance motor VB series reducer from1:10 to 1:20, at the same time, the motor sprocket2from the original 32 teeth, changed to 26 teeth , So the adjustment of the mechanism deceleration ratioreached more than 2 times the original. In the process of fetal billet shaping, the rotation drive of the distance motor can make the tire billet reach the super-stereotyped position by the training bit, but in the super-stereotyped position combination rolling process, the servo motor can not maintain the positioning for a long time, the display display pitch spacing gradually increased, the motor alarm, the equipment can not move. After that, the motor is replaced with Mitsubishi HG-SR352BJ 3.5KWwith electromagnetic brake servo motor, the situation has changed, but there will be motor overload alarm problem.

As a result of the preliminary verification, the selection of the distance servo motor needs to be re-demonstrated, and the selection of rotary servo motor is verified.

2.1.2 Selection conditions

Servo motor selection, generally follow the following principles:

(1) Continuous operating torque < servo motor rated torque (special case 0.8 times)

(2) Instant maximum torque < servo motor maximum torque (when accelerating)

(3) Inertia ratio < required by motor (4times)

(4) Continuous operating speed < motor rated speed

2.2 Pitch servo motor selection verification

2.2.1 Relevant parameters:

After consulting the relevant drawings and information, as follows:

Tire Billet quality M_1: 78kg

Spindle quality M_2: 280kg

External bushing quality M_3: 73kg

Left and right shaping drum mass M_4: 15kg

Ball screw mass M_{sg}= 24.2 kg pitch P_B =8mm nominal diameterD_{sg} take 60 mm

Ball screw friction coefficient: μ_1 take 0.02

Tire Billet rim plane width 915mm, predetermined position 880mm stay 5 seconds, ultra-shaping location 430mm, training totaltime 42 seconds

Ball screw sprocket Tooth number Z_1 = 17 mass M_{L1}= 2.1 kg, chain 16A

Motor sprocket Tooth number Z_2 =26 quality M_{L2}= 4.8 kg

Motor deceleration ratio is based on the original design to take i_1 =20

VB180 reducer transmission efficiency take η_1 = 90%

Sprocket drive Efficiency η_2 = 96%

Transmission efficiency of ball screw η_3 = 95%

Ball screw positioning accuracy APC 0.01mm

2.2.2 Servo motor speed

According to the actual production, the unilateral training pitch speed V control in 6.5 mm/s is most suitable, the maximum speed of 8 mm/s, because the ball screw drive The shaping chuck at the same time parallel, the shape of the pitch speed of twice times the unilateral speed. The maximum speed of the servo motor is determined by the shaping speed, the screw pitch and the deceleration ratio of the transmission system, by the formula:

$$N_e \geq N = 60 \ \frac{V}{P_B} \times i_z \tag{2}$$

N--Servo motor speed ,r/min

V--Tire billet shaping distance working speed ,mm/s

i_z -Total deceleration ratio of the distance adjustment mechanism

Put V = 6.5 mm/s, PB = 8mm, iz =Z1/Z_2 × i1 = 13.08, get N = 637.5 r/min

Maximum speed N_{max}= 785 r/min.

2.2.3 Load inertia

The load inertia of the distance servo motor is the inertia generated by acceleration and deceleration during the shaping pitch. When the load inertia is relative to the motor inertia exceeding the load inertia ratio specified by the motor, the motor response characteristics become worse. In the training process of two-segment molding machine, in order to ensure the positioning accuracy and response characteristics, it is required that the load inertia J_Z converted to the shaft end of the motor and the inertial J_M ratio of the motor itself be within 4 times range.

1) 2 ball screw inertia converted to the shaft end of the motor:

$$J_{sg} = \frac{2J_1}{i_z^2} = \frac{2M_{sg}D_{sg}^2}{8i_z^2} \tag{3}$$

To $J_{SG} \approx 1.27$ kg · cm²

2) 2 Ball screw sprocket inertia converted to the shaft end of the motor:

$$J_{L1} = \frac{2J_2}{i_z^2} = \frac{2M_{L1}D_{L1}^2}{8i_z^2} \tag{4}$$

Calculate p= 25.4mm pitch sprocket, estimate

$$D_{L1} = \frac{p}{\sin\frac{180^o}{Z_1}} = 138\text{mm}$$

by fractal circle diameter, and get J_{l1} ≈0.58 kg· cm²

3) 1 motor sprocket inertia converted to the shaft end of the motor:

$$J_{L2} = \frac{J_3}{i_1^2} = \frac{M_{L2}D_{L2}^2}{8i_1^2} \tag{5}$$

Estimation by split circle diameter

$$D_{L2} = \frac{p}{\sin\frac{180^o}{Z_2}} = 211\text{mm}$$

get J_{L2} ≈ 0.67 kg • cm²

4) Inertia of axial moving parts:

$$J_Y = M_Z \times \left(\frac{P_B}{2\pi}\right)^2 \tag{6}$$

Where M_Z -The sum of the quality of the accessories such as the shape of the tire billet, the outer bushing, the spindle, the shaping drum and the bracket, take 500kg

Get J_Y ≈ 8.1 kg • cm²

5) The moment of inertia of the reducer, check the sample of VB-DR-180-020-S2-P1 reducer, the moment of inertia is J_{j1}=7.3kg·cm²

6) The sum of the inertia of the inner ring of 4 bearings on 2 ball screws is smaller than that of the sprocket and ball screw, and the inner ring inertia of the bearing is small.

$J_Z = J_{SG} + J_{l1} + J_{l2} + J_Y + J_{j1} \approx 18.0 \text{kg} \bullet \text{cm}^2$

Check Mitsubishi HG-SR352 J servo motor sample, rated speed of 2000r/min, maximum speed of 3000r/min, motor rotor inertia J_M= 88.2 kg· cm^2, much larger than the Load inertia at the end of the motor shaft, and the load inertia matched.

2.2.4 Load torque

The load torque of the distance motor refers to the working driving force, friction and acceleration torque of the mechanical moving part during the training pitch, and after a working cycle of the two-segment molding machine, the motor is shut down for a long time, requiring the load torque $T_L \leq T_e$ can be.

1) Load torque generated by internal pressure

In the horizontal axial position of the training process, the axial load F_a of the shape internal pressure on the left shaping drum and the right shaping drum can estimate the load torque converted to the shaft end of the motor by the left and right ball screws, as shown in Figures 2 and 3:

When the stereotype is in an ultra-stereotyped position, at this point, the internal pressure is the largest, resulting in the largest axial load, 2 F_a

$$F_a = \frac{\pi(D_t{}^2 - d_t{}^2)\times 10^{-6}}{4} \times 0.18 \times 10^6 \tag{7}$$

D_t --Maximum diameter of fetal billet cavity, 1100mm

d_z -shape drum spindle outer diameter, 140mm

By the above parameters, get the $F_a \approx 168203.5$ N

Load torque generated by motor shaft end T_{ny}:

$$T_{ny} = \frac{2F_a P_B}{2\pi\eta_1\eta_2\eta_3 i_z} \tag{8}$$

Substitute the above calculated values, $T_{ny} \approx 39.9$Nm

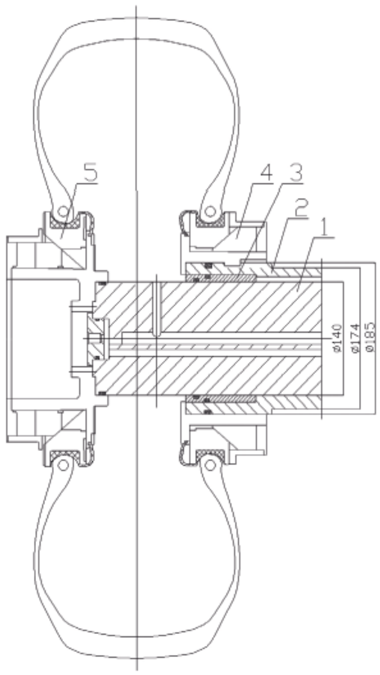

1- spindle; 2-outer bushing; 3-bearing; 4-right shaping drum; 5-left shaping drum

Figure 2: shaping drum shrinkage structure diagram

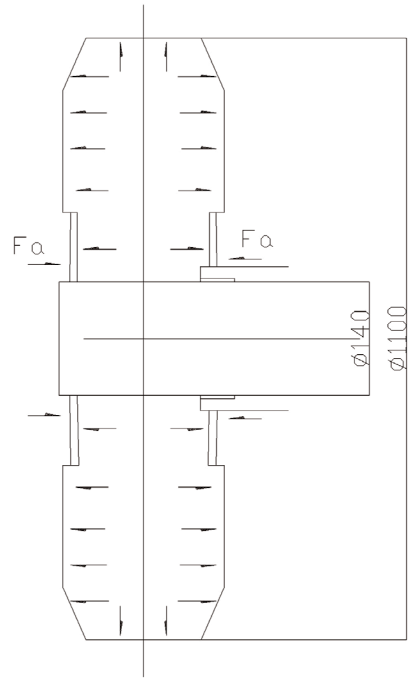

Figure 3: Analysis of inflatable force of Tire Billet

2) Friction load torque T_μ, generated by friction of the bearing

$$T_\mu = \frac{F_{\mu 0} P_B}{2\pi\eta_1\eta_2\eta_3 i_z} \tag{9}$$

$F_{\mu 0}$ --friction of the load state bearing, N, $F_{\mu 0} = \mu F_z g$

μ--Friction coefficient of copper tile and steel, take μ=0.15

F_z -The total friction caused by the relative motion of the outer bushing and spindle, N

As shown in Figure 1, during the mainframe pitch, the spindle and the outer bushing are relatively panned, while bearing the weight of the cantilever shaft support tire billet, the contact bearing of each component is sliding friction, the force size changes, according to the two section of the main spindle length, support point position, cantilever length, force direction and other related factors, the estimated total friction force F_Z at 2~4 times the M_z value, where the mean value of 3 times is calculated, the known value is taken into the $T_\mu \approx 0.26$ Nm

3) Additional pre-tightening torque T_f, generated by screw pretightening Force

The ball screw drive with fetal billet shaping does not allow for reverse clearance, requires high positioning accuracy and axial stiffness, and the ball screw should be pre-set to pre-tighten the force. In this example, the ball screw is balanced by axial force, and the axial load is approximately1/20~1/40 of the rated dynamic loadof the ball screw. Check the FFZD6308 ball screw rated dynamic load for 40KN, take the preload F_f = 2 KN, calculate 2 ball screws, there are:

$$T_f = \frac{2KF_f P_B}{2\pi\eta_1\eta_2 i_z} \tag{10}$$

K--ball screw torque coefficient $k = 0.05\sqrt{(\tan\beta)}$, β for ball screw guide Angle

$\tan\beta = \frac{P_B}{\pi D_a}$, Da is the roller diameter, check the ball screw sample D_a=4.762mm, get k=0.037

F_f --pretightening force of ball screw nut pair, N

Substitute known values for $T_f \approx 0.017$ Nm

4) Maximum Load torque

Molding machine Shape drum no-load pitch process, fast forward maximum load torque T_{KJ}:

$$T_{KJ} = T_{\mu} + T_f \approx 0.28 \text{ Nm} \tag{11}$$

The maximum load torque T_{GJ} during the formation of the tire billet of the molding machine:

$$T_{GJ} = T_{ny} + T_f \approx 39.9 \text{ Nm} \tag{12}$$

$$T_e \geq \text{MAX}\{T_{KJ}, T_{GJ}\} = 39.9 \text{ Nm} \tag{13}$$

5) Maximum acceleration torque required at the end of the motor shaft.

When the no-load accelerates the start ,The training process is generated by the linear acceleration law of the TorqueT_{ap}:

$$T_{ap} = \frac{2\pi N_{max}(J_M + J_z)\times 10^{-4}\times(1-e^{-k_s t_a})}{60 t_a} \tag{14}$$

N_{max} -The maximum speed of the motor corresponding to the load-empty shaping drum moving at the fastest speed, r/min

J_M -rotor inertia of the motor,kg· cm²

J_z -Motor total load inertia,kg· cm²

$t_a = 3/K_s$,k_s is the position ring gain of the servo system, Hz, usually take k_s = 8~25Hz, servo motor in position control mode. Pulse to add deceleration slope, molding machine training requirements positioning accuracy control in 0.1mm can be, the desirability of k_s=10 Hz, get t_a= 0.3s

Substitute the above values for $T_{ap} \approx 2.8$ Nm

In the tire billet booking process, at this time there is a 5-second time pause process, and began to run until the training, ultra-stereotyped position, the motor in the load acceleration state, the resulting acceleration torque T_{ad}:

$$T_{ad} = \frac{2\pi N(J_M + J_z)\times 10^{-4}}{60 t_a} \tag{15}$$

N-maximumshaping speed when the motor speed, for the motor operating speed, r/min

t_a = 1/k_v ,k_v for servo systemspeed loopgain, Hz, satisfying formula:positionringgain (1/s) ≤2*π*speed ringGain (Hz)/4, take k_V=2k_S=20Hz, get t_a= 0.05s

Substitute the above values for $T_{ad} \approx 14.2$ Nm

6) Maximum torque Ta required on the motor shaft:

No-load startup acceleration torque

$$T_{akj} = T_{ap} + T_{\mu} + T_f \approx 2.1 \text{ Nm} \tag{16}$$

Styling speed change accelerate torque

$$T_{aGJ} = T_{ad} + T_{ny} + T_f \approx 54.1 \text{ Nm} \tag{17}$$

Maximum equivalent load torque

$$T_{dx} = \text{MAX}\{T_{aKJ}, T_{aGJ}\} = 54.1 \text{ Nm} \tag{18}$$

7) Molding machine Training process, servo motor in intermittent working state, no need to start frequently, braking, can not consider the servo motor in a cycle of torque mean square root value.

Mitsubishi HG-SR352BJ Servo rated torque 16.7 nm, maximum torque 50.1 nm, obviously, can not meet (13), (18) type requirements, the need for servo motor,deceleration machine re-selection.

According to the above relevant parameters, choose Mitsubishi Servo Motor Reducer HG-SR702BG1 type, 7.0KW, rated speed N_e 2000r/min， maximum speed 3000r/min, rated torque 33.4Nm, maximum torque 100Nm, motor inertia 161 kg· cm², choose Mitsubishi Reducer Speed ratio 1:29, reducer Model: KB-180-29-S2-P2 J_{J1}' = 15.2kg· cm², Reducer transmission efficiency: η_1' = 94%

According to the above formula, you can get:

$$i_Z' = \frac{Z1}{Z_2} \times i_1' \approx 19$$

$$N' = 926.3 \text{ r/min}$$

$$N_{max}' = 1140 \text{ r/min}$$

$$J_Z' \approx 24.5 \text{ kg}\bullet\text{cm}^2$$

$$T_{ny}' \approx 26.3 \text{ Nm}$$

$$T_\mu' \approx 0.17 \text{ Nm}$$

$$T_f' \approx 0.011 \text{ Nm}$$

$$T_{KJ}' = T_\mu' + T_f' \approx 0.18 \text{ Nm}$$

$$T_{GJ}' = T_{ny}' + T_f' \approx 26.3 \text{ Nm}$$

$$T_e' \geq \text{MAX}\{T_{KJ}', T_{GJ}'\} = 26.3 \text{ Nm}$$

$$T_{ap}' \approx 7.0 \text{ Nm}$$

$$T_{ad}' \approx 36.0 \text{ Nm}$$

$$T_{aKJ}' = T_{ap}' + T_\mu' + T_f' \approx 7.2 \text{ Nm}$$

$$T_{aGJ}' = T_{ad}' + T_{ny}' + T_f' \approx 62.3 \text{ Nm}$$

$$T_{dx}' = \text{MAX}\{T_{aKJ}', T_{aGJ}'\} = 62.3 \text{ Nm}$$

From the above calculation data can be seen :

Motor operating speed is less than motor rated speed, $N' <$ 2000r/min

The maximum working speed is less than the maximum motor speed,

$N_{max}' <$ 3000r/min

The load inertia of the motor shaft end is much smaller than the motor inertia,

$J_z' <$ 161 kg • cm²

The working torque is less than the rated torque of the motor,

$T_e' <$33.4 Nm

The maximum operating torque of the load is less than the maximum torque of the motor,

$T_{dx}' <$ 100 Nm

Through the verification, two-segment molding host distance motor re-selection qualified.

2.3 Rotary servo Motor selection Verification

2.3.1 Relevant parameters:

Consult the relevant drawings and materials as follows:

Servo motor model: HG-SR502J 5KW, reducer VB-DR-140-005-S2-P1 deceleration ratio i_2=5

Servo synchronous Belt Wheel: 32-14M, diameter d_1= 142.6 mm, number of teeth z_{dl1} = 32, Mass M_{dl1} = 7.7kg

Spindle Synchronous Belt Wheel: 80-14M, diameter d_2= 356.5 mm tooth number z_{dl2} = 80, mass M_{dl2} = 24.3kg

Friction coefficient between roller wheel and adhesive parts during tire billet combination rolling: μ_x take 0.20

Tire Billet combination Rolling working speed:N_x = 45r/min, maximum speed N_{xmax} = 65r/min

During the combination rolling process of the tire billet, the pressure change process of the rear pressure cylinder is as: 0.25 Mpa→0.3 MPa→0.35 MPa→0.25MPa, tire shoulder pressure roller pressure : 0.4MPa, tread press roller pressure: 0.4MPa

VB140 reducer transmission efficiency take η_{x1} = 95%

Synchronous belt drive Efficiency η_{x2} = 98%

2.3.2 rotating servo motor speed

The rotation speed of the rotating servo motor of the two-segment molding machine is determined by the rotation speed of the tire billet and the deceleration ratio of the transmission system, by the formula:

$$N_M = N_x \times \frac{z_{dl2}}{z_{dl1}} \times i_2 \tag{19}$$

The known data is included in the N_M = 562.5 r/min, the maximum speed N_{Mmax}= 812.5 r/min.

2.3.3 Load inertia

The load inertia of rotary servo motor of molding machine is the inertia produced during the acceleration and deceleration of the tire billet rolling process. During the combined rolling rotation of the two-segment molding machine, the load inertia J_{XZ} , which is required to be converted to the shaft end of the motor, is within 4 times the ratio of the inertial J_{Mx} of the motor itself .

1) Synchronous belt wheel inertia of servo motor converted to motor shaft end:

$$J_{dl1} = \frac{M_{dl1} d_1^2}{8 i_2^2} \tag{20}$$

Get $J_{dl1} \approx 7.8$ kg · cm²

2) The Spindle synchronous belt wheel inertia converted to the shaft end of the motor:

$$J_{dl2} = \frac{M_{dl2} d_2^2}{8 i_{xz}^2} \tag{21}$$

$i_{xz} = \frac{z_{dl2}}{z_{dl1}} \times i_2$ = 12.5, get $J_{dl2} \approx 24.7$ kg•cm²

3) Spindle, outer bushing inertia: In the tire billet combination rolling process, the spindle, external bushing together rotation, take M_{zz}= 400kg

$$J_{zz} = \frac{M_{zz} D_z^2}{8 i_{xz}^2} \tag{22}$$

Take D_z = 16 cm, get $J_{zz} \approx 81.9$ kg • cm²

4) Shaping Drum Inertia:

$$J_g = \frac{M_g\left(D_g^2 + d_z^2\right)}{8 i_{xz}^2} \tag{23}$$

M_g= 30kg,d_z = 14 cm, take D_g = 40 cm, get $J_g \approx 43.1$ kg • cm²

5) The moment of inertia of the reducer, check the sample of VB-DR-140-005-S2-P1 reducer, the moment of inertia is:

J_{j2} = 7.42 kg · cm²

6) Rotation inertia of tire billet

The tire billet model figure is shown in Figure 3, the total mass of the placenta is 78kg, and the placenta is divided into three parts, left, middle and right, and the quality of M_5=24kg, M_6=30kg, M_5=24kg,it is estimated respectively on both sides of the fetal shoulder. the left and right two parts are similar to hollow cylinders to calculate the rotational inertia, the middle part is different hollow cylinders, the sum of which is the moment of inertia of the whole fetal billet.

$$J_t = \frac{\frac{1}{8} M_5\left(d_t^2 + D_t^2\right) \times 2 + \frac{1}{8} M_6\left(D_t^2 + D_3^2\right)}{i_{xz}^2} \tag{24}$$

M_5 = 24 kg, M_6 = 30 kg, Rim diameter d_t = 50.4 cm, D_t = 110 cm, D_3 = 121 cm, get $J_t \approx 1204.0$ kg • cm²

7) The inertia of the inner ring of the rotating bearing on the spindle is very small relative to the spindle inertia and is negligible here.

$J_{xz} = J_{dl1} + J_{dl2} + J_{zz} + J_g + J_{j2} + J_t \approx 1368.9$kg • cm²

Check Mitsubishi HG-SR502J servo motor sample, rated speed of 2000r/min, maximum speed of 3000r/min, motor rotor inertia 99.7 kg· cm²,motor inertia ratio:J_{xz}/J_{Mx}= 13.7 times, well beyond the motor end load inertia 4 times range.

2.3.4 Load torque

Rotating servo motor load torque refers to the motor itself acceleration torque, load acceleration torque and normal operation of the required torque, molding machine combined rolling process, servo motor in a long time continuous working state, no need to start frequently, braking, do not consider the servo motor A periodic torque of the mean square root value,But to ensure that the load torque $T_{Lx} \leq 0.8T_{Mx}$

1) Accelerated torque of the motor itself T_{x1}

$$T_{x1} = J_{mx} \times \alpha_{mx} = \frac{2\pi N_{Mmax} J_{Mx} \times 10^{-4}}{60 t_{ax}} \tag{25}$$

In the speed control mode, the rotary servo motor operates according to the acceleration and deceleration time inside the drive, considering the large inertia of the tire billet, the acceleration and deceleration time can be extended appropriately. Take $t_{ax} = 10/k_{sx}$,k_{sx} Position Ring gain for servo system, Hz, usually take k_{sx} = 8~25Hz, take k_{sx}=10 Hz , Get t_{ax}= 1.0s

Substitute the above parameters for T_{x1} = 0.85 Nm

2) Load Acceleration Torque T_{x2}

$$T_{x2} = \frac{2\pi N_{Mmax} J_{xz} \times 10^{-4}}{60 t_{ax} \eta_{x1} \eta_{x2}} \tag{26}$$

Substitute known values for $T_{x2} \approx 12.5$ Nm

3) Torque T_{x3} required for normal operation, generated by combined rolling

After the completion of the fetal billet training, in two segments of the mainframe, the use of tread pressure roller, tireShoulder pressure roller, rear pressure roller on the tire billet adhesive parts for rolling. Tread Roller cylinder DSBC-80-560-PPVA-N3, 1 group; tire shoulder Roller cylinder DSBC-80-600-PPVA-N3, 1 group; rear pressure roller cylinder ADVU-80-80-A-P-A, 2 groups; tread roller and tireshoulder pressure roller different action, a certain period of time, there is a tireShoulder pressure roller (or tread pressure roller) and the rear pressureRoller simultaneous action process. As shown in Figure 4, considering the number of cylinders, cylinder diameter and other factors, the maximum rolling pressure appearsin the tireshoulder pressure roller(or tread pressure roller) and the rear pressureroller at the same time The period of action, at this time, the rear pressure gaspressureis up to 0.35MPa.

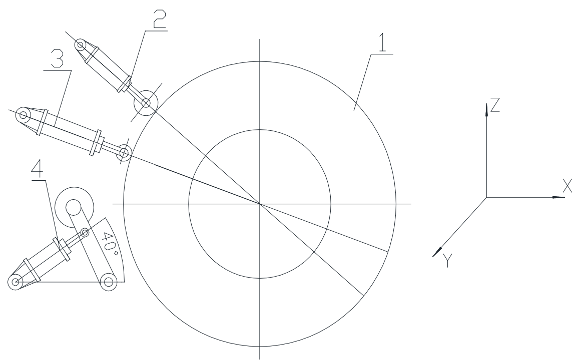

1-Fetal billet; 2-tread pressure roller; 3-tire shoulder pressure roller; 4-Rear Press Roller

Figure 4: Styling combination pressure Roller diagram

$$T_{x3}=\frac{\mu_x F_x \times \frac{D_3}{2}}{i_{xz}\eta_{x1}\eta_{x2}} \quad (27)$$

μ_x-Combination pressure roller and tire billet rolling friction coefficient, take 0.20

F_x-The maximum pressure force of the combined pressure roller on the centerline of the spindle, N ; it is equal to the joint force of the tireShoulder pressure roller andthe rear pressure roller.

$$F_x = F_j + 2\times F_h \cos 40^\circ$$
$$= \frac{\pi}{4}\times 0.08^2\times 0.4\times 10^6 + 2\times\frac{\pi}{4}\times 0.08^2\times 0.35\times 10^6\times\cos 40^\circ$$
$$= 4703.6\ \mathrm{N}$$

D_3-Outer diameter of tire billet, 1.21m

The known value , $T_{x3}\approx 48.9$ Nm, which is the working torque of the servo motor.

4) Maximum load torque

$$T_{xmax} = T_{x1} + T_{x2} + T_{x3} \approx 62.3\ \mathrm{Nm} \quad (28)$$

Mitsubishi HG-SR502J servorated torque 23.9 Nm, maximum torque 71.6 nm, obviously, can not meet the requirements of (27), at the same time, the motor load inertia ratio far beyond the requirements of not more than 4 times, the servo motor reducer needs to be re-selected.

According to the above relevant parameters, select Mitsubishi Servo Motor reducer, the motor reducer deceleration ratio from 1:5 to 1:17, rated torque 23.9Nm, maximum torque 71.6Nm, motor inertia J_{Mx}' = 99.7 kg· cm², reducer speed ratio 1:17, reducer model: KB180-17-S2-P2, reducer transmission efficiency η_{x1}' = 94%

To re-account the above values, you must:

N_M' = 1912.5 r/min,maximum velocity N_{Mmax}' = 2762.5 r/min。

$J_{dl1}'\approx 0.67$ kg · cm²

$J_{dl2}'\approx 2.1$ kg • cm²

$J_{zz}'\approx 7.08$ kg • cm²

$J_g'\approx 3.7$ kg • cm²

J_{J2}' = 15. 2kg·cm² (check Mitsubishi Servo motor REDUCER sample)

J_t' = 104.2 kg • cm²

$J_{xz}'\approx 133$ kg • cm²

Check Mitsubishi HG-SR502J servo motor sample, rated speed of 2000r/min, maximum speed of 3000r/min, motor rotor inertia J_{Mx}' = 99.7 kg· cm², Themotor inertia ratio is:J_{xz}' / J_{Mx}' = 1.33 times, well below the motor end load Inertia 4 times range, load inertia matching.

$T_{x1}'\approx 2.88$ Nm

T_{x2}' = 4.17 Nm

$T_{x3}'\approx 14.5$ Nm

$T_{Mx}'\approx 21.6$ Nm

Mitsubishi HG-SR502J Servo motor rated torque 23.9 nm 0.8 times greater than the load torque T_{x3}' 14.5Nm, Motor Maximum torque 71.6 nm greater than maximum load torque T_{MX}' 21.6Nm, For the host rotating servo motor deceleration Machine to re-qualified selection.

3 2-segment Molding machine host rotation and shaping servo motor selection Summary

Two segment molding machine host re-selection replacement servo motor, reducer process, some selection parameters are summarized, as follows:

3.1 Host Styling Pitch Servo Motor

Original motor, gearbox model: HG-SR352BJ with VB-DR-180-020-S2-P1

Related parameters:

Rated speed 2000 r/min

Maximum speed 3000 r/min

Inertia 88.2 kg•cm²

Rated torque 16.7 Nm, maximum torque 50.1 Nm

Convert the load to the end of the motor shaft:

Rev 637.5 r/min

Maximum speed 785 r/min

Inertia 18 kg•cm²

Operating torque 39.9Nm, maximum torque 54.1 Nm

Selection verdict: Unqualified

Non-conformities: operating torque and maximum torque exceed motor rated torque and maximum torque

Re-selected motor, gearbox: HG-SR702BG1 with KB180-29-S2-P2 Mitsubishi brand

Re-select motor parameters:

Rated speed 2000r/min

Maximum speed 3000r/min

Inertia 161 kg•cm²

Rated torque 33.4Nm, maximum torque 100 Nm

Convert the load to the end of the motor shaft:

Speed 926.3 r/min

Maximum speed 1140r/min

Inertia 24.5 kg•cm²

Operating torque 26.3Nm, maximum torque 62.3 Nm

Re-selection verification results: qualified

3.2 Host Rotary Servo Motor

Original motor, gearbox model: HG-SR502JVB-DR-140-005-S2-P1

Related parameters:

Rated speed 2000r/min

Maximum speed 3000r/min

Inertia 99.7 kg•cm²

Rated torque 23.9Nm, maximum torque 71.6 Nm

Convert the load to the end of the motor shaft:

Rev 562.5r/min

Maximum speed 812.5 r/min

Repertoire 1368.9 kg•cm^2

Operating torque 51.6Nm, maximum torque 65.7 Nm

Selection verdict: Unqualified

Non-conformity: operating torque exceeds motor rated torque, load inertia ratio exceeds specified value

Re-selected motor, gearbox: HG-SR502J (unchanged) with KB180-17-S2-P2 Mitsubishi brand

Re-select motor parameters:

Rated speed 2000 r/min

Maximum speed 3000 r/min

Inertia 99.7 kg•cm^2

Rated torque 23.9Nm, maximum torque 71.6 Nm

Convert the load to the end of the motor shaft:

Rated speed 1912.5r/min

Maximum speed 2762.5r/min

Inertia 133 kg•cm^2

Working torque 14.5 Nm, maximum torque 21.6 Nm

Re-selection verification results: qualified

The key point of selection of servo motor for two-segment molding machine is the calculation of load torque, and the selection of Rotary servo motor has a large load inertia. The above two sets of calculated servo motor, reducer, as well as re-alignment motor servo system control drive, cable, connector selection, installation in place and modify the corresponding PLC program, after 2 consecutive months of production, there are no problems, in the production practice has been fully verified.

4 Conclusion

The selection design of host pitchandrotary servo motor in radial Air Tire two-section molding machine is a relatively complex design and calculation process, which involves many disciplines of mechanical design and manufacture, including mechanical transmission, kinetic energy conservation Conversion, mechanical analysis, Electrical control and so on. Servo motor selection must be based on the actual operating conditions of the motor continuous working torque, instantaneous maximum torque, inertia ratio, continuous operating speed and other parameters and its own rated torque, maximum torque, the specified inertia ratio, rated speed comparison, in line with the principle of less than the latter, choose servo motor and supporting gearbox. Under certain circumstances, the maximum speed of the servo motor should also be considered, and if the servo motor is started frequently and braking, parameters such as the torque mean square root value of torque during a period are also considered. In the process of production practice, the efficient and smooth operation of equipment is the practice test process of design and manufacture, and the applicability audit process of special working conditions on site. Equipment manufacturers can draw lessons from this, design and develop suitable for high-performance radial air tire molding key manufacturing equipment.

Personal CV: Wang Chaoqun (1974---) Man AnhuiYingShang Bachelor of Engineers, Double Star Tire Co., Ltd. is engaged in rubber equipment technology work, published 23 papers. Qingdao Road, Huangdao District, Shandong Province, No. 666 Doublestar R & amp; d Center 1410004241@qq.com

References

[1] LiuCaixia TOM-L5641 CNC Milling Machine servo motor selection and calculation [J] Journal of Baotou Vocational and Technical College P25-26 Issue 3rd of 2014

[2] Xiao Xiao et al. Selection principle and calculation of servo motor [J] machine tool & amp; Hydraulic 2014 issue 22nd P46

[3] Wangjianghong et al. Calculation and selection of X-axis servo motor for CNC gantry milling machine [J] Machinery Manufacturing 2016 12th month P10-11

[4] Fanwei et al.Selection and calculation of AC servo motor feeding in machining center [J] Electromechanical technology 2017 8th month P48-49

Viser Technology Pte. Ltd.
Mechanical Engineering Science
https://doi.org/10.33142/me.v1i1.658

Research Article Open Access

The Additive Manufacturing Process of Electric Power Fittings Fabricated by Metal Droplet Deposition

Haihua Wu[1] **, Guangxi Zhao**[2] **, Zhengying Wei**[*1,2]

[1] College of Mechanical & Power Engineering, China Three Gorges University
[2] The State Key Laboratory for Manufacturing Systems Engineering, Xi'an Jiaotong University

***Corresponding Author:** Zhengying Wei, zywei@mail.xjtu.edu.cn*

Abstract:
Metal droplet deposition is a kind of additive manufacturing (3D Printing) technique that fabricates near-net part through droplets deposition with lower cost and higher efficiency. This paper proposed a solution to problems of electric power fittings that large inventories, high procurement costs, low manufacturing efficiency and transportation cost. Using additive Manufacturing technique - metal droplet deposition, electric power fittings fabricated on power construction site. This paper describes the manufacturing process of typical thin-walled samples (the structure optimized based on additive manufacturing principle) and ball head rings of electric power fittings. Aiming at the integral AM forming for ball and ball socket electric power fitting workpiece, a novel easy removal forming support material (ceramics and gypsum mixed with UV cured resin) have been developed. Here this support material was used to fabricate nested integral workpieces. Dimensional accuracy and microstructure of the test pieces were analyzed. The error of the height and width of the forming workpiece is within 5%. No obvious overlap trace (such as overlap line and cracks) observed, and the internal microstructure is equiaxial crystal. The average density of the component is 99.51%, which measured by drainage method and 13.39% higher than the cast raw material.

Keywords: *Additive manufacturing; Metal droplets; Electric power fittings; Thin-walled sample; Ball head rings workpiece.*

Citation: H.H. Wu, G.X. Zhao, Z.Y. Wei, The Additive Manufacturing Process of Electric Power Fittings fabricated by Metal Droplet Deposition. *Mech Eng Sci*, 2019,1(1): 27-32. https://doi.org/10.33142/me.v1i1.658

1. Introduction

Metal additive manufacturing (3D printing) of metallic materials has become a research hotspot in additive manufacturing (AM) technology [1-2], which fabricates functional component directly. Currently, high power laser or electron beam are adopted as heat source in metal 3D printing [3-4], and raw materials are usually in powder or wire form, leading to high cost and material limitations. As a result, it is necessary to propose a new metal additive manufacturing technology that cost saving and high efficiency. In this paper a 3D printing device has been established for fabricating electric power fittings using electromagnetic induction as the heat source.

At present, the main forming methods of electric power fittings are casting and forging. The issues that large inventories, high procurement costs, low manufacturing efficiency and transportation cost have caused great economic losses. Therefore, it is significant to fabricate electric power fittings on power construction site using high efficiency and low-cost metal 3D printing process according to site requirement.

Metal droplet deposition is an additive manufacturing process during which workpieces are fabricated from molten materials without mould or other tooling. Workpieces are fabricated by droplets deposition layer-by-layer which belongs to near net shape methods. Electric power fittings are fabricated by metal droplet deposition process, satisfying the electrical repairs requirements, while reducing assembly costs and achieving zero inventories.

Researchers at the University of Toronto [5-6] researched 3D printing technology of tiny metal workpieces, which uses pulsed air pressure to melt low-melting tin-lead metals under a pneumatic pulse. The lead or tin metal droplets with diameters between 100 and 300μm printed by layer-by-layer stacking of droplets [7], Lee [8] produced uniform solder droplets with a molten metal inkjet system, but the material is limited to low melting metal materials. Wenbin [9] researched the droplet deposition process of metal workpieces and intermetallic compound materials, but the surface quality is low. Xiong and Ando established the numerical analysis models with different overlapping conditions [10-11]. Trapaga studied the spreading and solidification mechanism of the droplets deposition within a narrow space and large temperature gradient [12]. The numerical analysis and experimental varication were used to investigate the metal droplet deposition and spreading with different process parameters, such as droplet size, displacement and substrate temperature. At present, the numerical simulation works [13-15] of droplets deposition and overlap processes were mainly based on simple prototypes, which couldn't reflect practical application value of the deposition process.

In this paper, the process test is carried out for typical electric power fittings with cantilever structure, and the forming accuracy and microstructure of the forming workpieces are analyzed. The functional parts of electric power fittings were fabricated by successive deposition and solidification of molten aluminium droplets on a horizontally Al alloy substrate, and the microstructure and performance of deposition parts were also analyzed. The morphology and the influences of the internal quality of the droplets on the cross-sectional feature were revealed. The results could provide technical support and reference to the electric power fittings forming.

2. Experimental system and Methods

2.1 Experimental system

Figure 1 shows a conceptual view of the droplet deposition process. It mainly consisted of a pneumatic system, a motion control system, a forming process monitoring system and an inert environment control system. The pneumatic system is used to produce metal droplets on demand. It includes a droplet controller, a solenoid valve, a crucible, a heating furnace and a nitrogen gas resource. The motion control system is used to form the workpieces by controlling the motion of a 3D platform according to data information. It consisted of a PMAC (program multiple axes controller), a 3D movement platform and the deposition substrate. The forming process monitoring system composed by a CCD camera and an image acquisition card is used to observe the deposition process of droplets. The inert environment control system is made up of glove box and gas circulating device. It is used to prevent the metal from being oxidized. The whole process is coordinately controlled by industrial computer to complete the fabrication of workpieces.

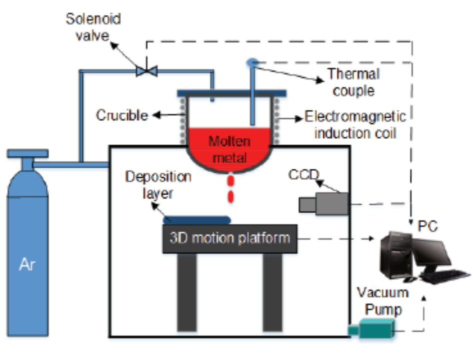

Figure 1 Schematic diagram of droplet deposition system

Figure 2 shows the experimental system of droplet deposition according to above schematic diagram. The equipment mainly includes pneumatic drive system, droplet deposition system, inert gas protection system and three-dimensional motion translation stage. The photograph in Figure 2 shows the manufacturing system established by the scholars in Xi'an JiaoTong University (China) [16-17].

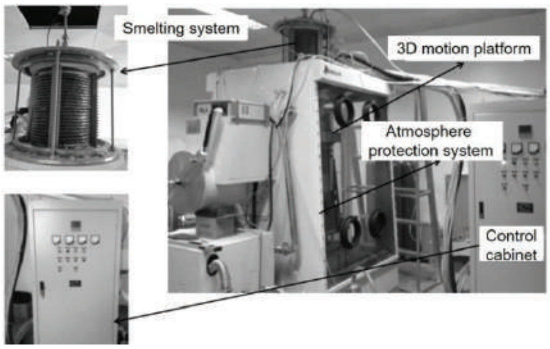

Figure 2 Experimental system of droplet deposition

2.2 Manufacturing parameters of electric power fittings

A variety of electric power fittings are exhibited in Figure 3. It can be seen that there are so many kinds of electric power fittings. So, a typical component that a movable joint with hollow structures (shown in Figure 4) were selected for the forming research. As shown in Figure 5, the movable joint mainly consists of a thin-walled workpiece and a ball head ring workpiece. As long as the parts shown in Figure 4 can be processed by the droplet deposition process, almost all the forming of the electric power fittings can be realized.

Figure 3. Structure of the electric power fittings

Figure 4. The movable joint with hollow structure

Figure 5(a) Typical thin-walled workpiece

Figure 5(b) Ball head ring workpiece

One of the advantages of additive manufacturing technology is the ability to simplify complex assemblies into one functional part. As shown in Figure 6a to Figure 6c, the structure of typical thin-walled workpiece was redesigned based on the characteristics of metal droplet deposition. The thin-walled workpiece with 100mm*2mm dimension was fabricated by molten droplets depositing sequentially layer by layer. The experimental parameters were shown in Table 1.

Table 1 Process parameters of typical Electric Power Fittings

Parameter	Value
Scanning speed (mm`s^{-1})	30
Droplets temperature (K)	950
Substrate temperature (K)	400
Nozzle diameter (mm)	0.7
Pulse pressure(Mpa)	0.4
Oxygen content (PPM)	20
Frequency(Hz)	30
Manufacturing time (min)	12.5
Interlayer height (mm)	1

During the manufacturing process, droplets with initial temperature of 950K were generated and deposited onto a 400K substrate. Deposition experiments were carried out in glove box under inert atmosphere with low oxygen content (below 20 ppm). The argon gas pulses were imposed by a solenoid value onto the molten metal in crucible with a 0.4MPa pulse pressure and a 30 Hz pulse frequency. Therefore, the uniform droplets are ejected from the nozzle with a diameter of 0.5 mm at the bottom of the crucible, which is wrapped by a resistance heating ring. In order to stabilize the morphology and dynamic behavior of droplets, the distance between nozzle and substrate is 5 mm. The time it takes to fabricate the typical thin-walled workpiece is 12.5min, when the displacement speed is 30mm/s and the height interval of adjacent layer is 1mm.

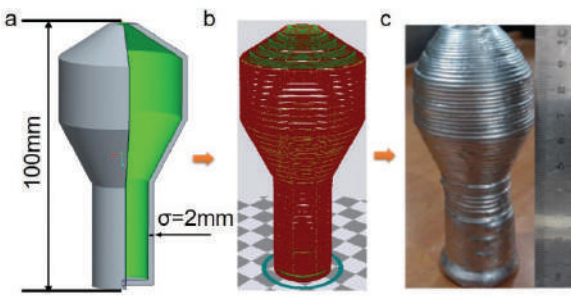

Figure 6 Structure of typical thin-walled workpiece. (a) Model (b) schematic diagram of layer slices (c) workpiece fabricated by droplets

As is shown in Figure 7, the ball head ring workpiece 85 mm in length, 42 mm in width and 12 mm in height and 15 mm of the inner diameter. According to the influencing factors of droplet deposition process, the stratified cross section is shown in Figure 7b, the suitable parameters such as scanning speed, droplet temperature and nozzle diameter were selected, Workpiece of ball head ring after rough grinding is shown in Figure 7c. The process parameters of deposition of ball head ring workpiece are the same with the parameters of thin-walled workpiece except the interlayer space. The time used for building the ball head ring workpiece was 13.5min, when the scanning speed was 30mm/s and interlayer spacing was 0.6mm.

Figure 7 Structure of ball head ring workpiece. (a) Model; (b) Schematic diagram of layered slices; (c) The workpieces fabricated by droplets

2.3 Investigation on supporting materials

Due to the existence of cantilever and movable joints, it is necessary to add support during the metal droplet deposition forming process, otherwise collapse and joint immobility will occur. Based on the principle of metal droplet deposition process, it can be known that good supporting properties, fluidity, high temperature resistance and removable property are required for supporting material. As shown in Figure 8, supporting material performance testing device mainly consisted of a pneumatic system, a nozzle, a 3D motion platform and corresponding control software. The pressure control device controls the outlet pressure of the pressure tank to extrude the support material out of the nozzle stably. Simultaneous, the 3D motion platform moves under the control of the pre-set path until the desired support is formed. In this paper, water, gypsum powder, sand, ceramic powder, and resin were mixed in different proportions to develop supporting materials.

Forming process diagram of suspended structure was shown in Figure 9. The two nozzles were alternately operated, one nozzle was provided with the metal material to be formed, and the other nozzle was filled with the suitable supporting material. Firstly, the metal substrate was deposited layer by layer by droplet deposition, and then the supporting material of a specified shape was deposited under the suspended portion of the power fitting. Furthermore, the cantilever structure was deposited on the supporting material and finally the supporting material was removed to complete the forming of the cantilever.

3. Results and Discussion

3.1 Forming accuracy of droplet deposition

The height and thickness of the experimental measurements are shown in Table 2 by multiple measurements. It can be seen that the relative error in height direction is small, but it is larger in thickness direction. This is due to that the relative error of height direction is more prominent than that in thickness direction during deposition. The experimental results verify the correctness and feasibility of the typical thin-walled workpiece prepared by droplet deposition process, and provide a new method for the research of thin-walled workpiece.

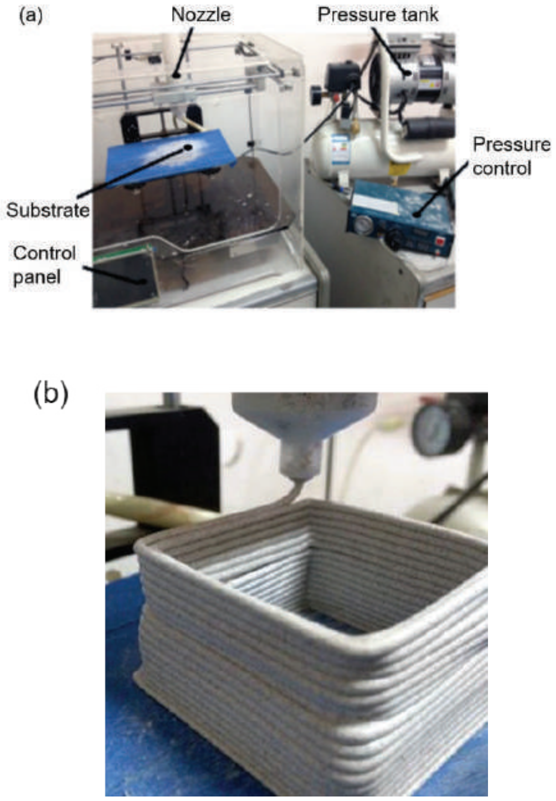

Figure 8 Testing device of supporting material performance

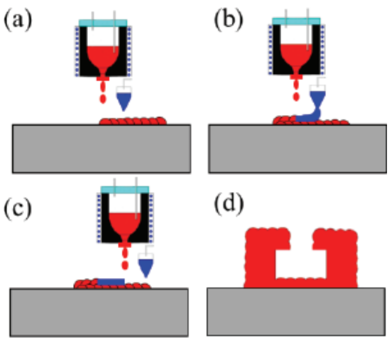

Figure 9 Forming process diagram of suspended structure

In order to verify the manufacturing accuracy of the ball head ring workpiece, by using the method of averaging through multiple measurements, the dimensional accuracy of the forming part was measured and analysed and the results are shown in table 3.

3.3 Performance test of the supporting material and nested integral workpiece

The different proportions and properties of supporting material are shown in Table 4.

As is shown in Table 4, No.3, No.4 and No.5 have high supporting strength and better surface quality so that they are suitable, and their accuracy retaining abilities were further tested, respectively. Initial samples were rectangular with a cylindrical hole, and the dimensions of the hole were measured after 12 hours standing. Results are shown in Table 5.It can be seen from Table 5 that No.5 supporting material has the best accuracy retaining ability so it was adopted to process suspended structure. Comparison of electric power fittings structure is shown in Figure 10.

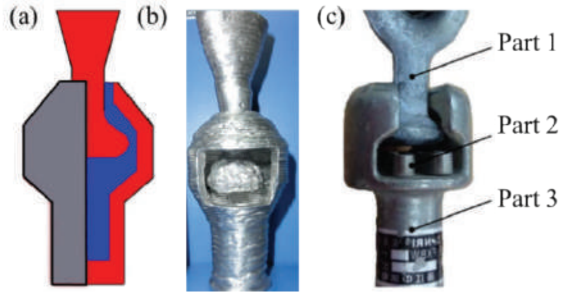

Figure 10 Electric power fittings. (a) model (b) Experimental piece (c) Original component

As shown in Figure 10, complex nested component was fabricated by metal droplet deposition with supporting material. Compared with traditional subtractive method, the workpiece is simplified as an integral structure, which can greatly reduce the assembly cost.

3.4 Microstructure Analysis

The formed end-shapes were examined by SEM (scanning electron microscope). The droplet diameter was maintained at a size of about 100 μm in all experiments because at this size, the resulting droplets were the most stable. The initial droplet diameter was measured by integrating Nikon AF Micro 200 mm and Monarch Nova-Strobe BBX 115/230 Digital Portable Stroboscope.

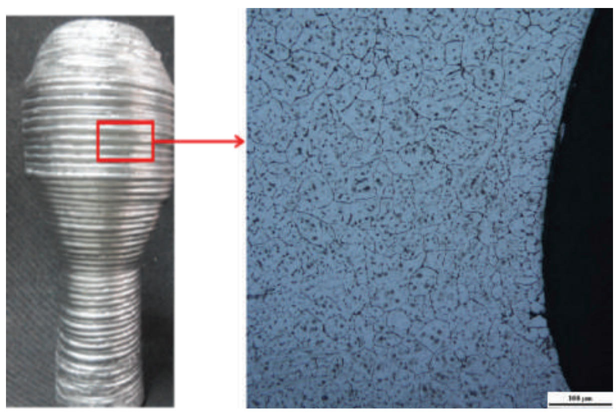

Figure 11 Microstructure of overlap area

As illustrated in Figure 11, no obvious overlap trace (such as overlap line and cracks) was observed, and the internal microstructure is equiaxial crystal.

3.5 Density Measurement

Density was measured by drainage method, measuring principle diagram of which is shown in Figure 12.

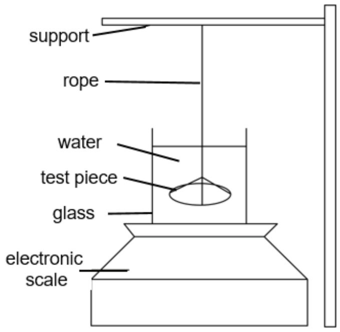

Figure 12 Measuring principle diagram of density

Measure the mass of the test piece in the air and marked as m1, and put a cup of water on an electronic scale and set the display to zero. Immerse the test piece in water, ensuring that the water doesn't spill and that the test piece doesn't touch the bottom of the cup and marked the display as m2. The actual density of droplet deposition component can be expressed as:

$$\rho_{\text{test}} = \frac{m_1}{m_2}\rho_{water} \tag{3}$$

Densification degree can be calculated by:

$$D = \frac{\rho_{\text{test}}}{\rho_{theory}} \tag{4}$$

This paper takes six pieces of droplet deposition components and raw casting material respectively for densification test, results are shown in Figure 13.

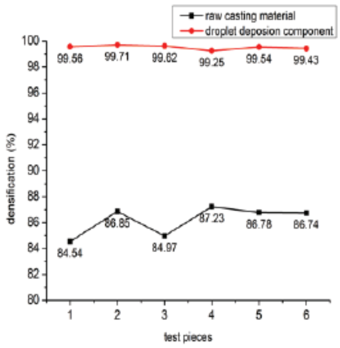

Figure 13 Density of test pieces

Table 2 Height and thickness measurement results of typical thin-walled workpiece

	Five measurement values /mm	Average value /mm	relative error
Height	101;98;102;101;100	100.4	0.4%
Thickness	2.05;2.10;2.12;1.96;1.92	2.03	1.5%

Table 3 Measurement results of ball head ring workpiece dimension

	Five measurement values /mm	Average value /mm	relative error
Height	85.8;86.3;85.3;85.7;85.9	85.8	0.94%
Thickness	42.8;43.6;42.3;42.7;43.1	42.9	2.14%
diameter	14.5;14.2;14.8;14.6;14.4	14.5	3.3%

Table 4 Proportions and properties of supporting material

NO	gypsum powder/g	ceramic powder/g	Sand/g	Photosensitive resin/ml	Water/ ml	Supporting strength	Surface quality	Extrusion performance
1	62	62	0	0	40	--	--	Hard to squeezed out
2	62	62	0	0	50	High	Good	Squeezed out but solidified too fast
3	62	0	0	25	0	High	better	Squeezed out, no solidification
4	62	62	0	35	0	High	better	Squeezed out, no solidification
5	62	62	62	48	0	High	better	Squeezed out, no solidification
6	62	0	25.5	0	88	Higher	Good	Squeezed out but solidified too fast

Table 5 Results of accuracy retaining abilities

NO.	placement methods	Diameter/mm	Depth/mm
3	Initial sample	10	7
	After 12h (without light)	10.5	6
4	Initial sample	8 8	9 9
	After 12h (with light)	8.5 7.8	8.9 9.2
5	Initial sample	12 12 12 12	8 8.5 9 9
	After 12h (with light)	12 12 12 12	8 8.6 9 9

The average density of droplet deposition component and raw casting material were respectively 99.51% and 86.12%. Droplet deposition isn't like casting which usually has defects such as air entrainment and shrinkage, so that the densification is higher.

4. Conclusions

In this paper, the functional parts of electric power fittings were fabricated by successive deposition with a suitable supporting material, and the microstructure and performance of deposition parts were also analyzed. Experiments proved that the typical electric power fittings fabricated by droplets depositing satisfied the using requirements.

(1) Using the process parameters shown in Table 1, such as substrate temperature and moving speed, the droplet deposition process was experimentally investigated. It is found that the relative error of dimension is less than 5%.

(2) Aiming at the integral AM forming for the typical electric power fitting workpiece, the composition and performance of forming support material were researched. The optimal support material composition and configuration are shown in the fifth group of schemes in Table 4. Nested integral workpieces were fabricated with this support material.

(3) Dimensional accuracy and microstructure analysis of the workpieces were carried out. No obvious overlap trace (such as overlap line and cracks) was observed, and the internal microstructure is equiaxial crystal.

(4) Density of the metal droplet deposition workpiece was measured by the drainage method. The average density of droplet deposition components is 99.51%, which is much higher than the cast raw material.

Acknowledgements: This research was funded by National Natural Science Foundation of China under grant number 51575313 and 51775420. This paper got help from Du Jun and Wang Xin of Xi'an Jiaotong University.

References

[1] Frazier, W. E. (2014). Metal additive manufacturing: a review. Journal of Materials Engineering and Performance, 23(6), 1917-1928.

[2] Wong, K. V., & Hernandez, A. (2012). A review of additive manufacturing. ISRN Mechanical Engineering, 2012.

[3] Zhang, B., Li, Y., & Bai, Q. (2017). Defect formation mechanisms in selective laser melting: a review. Chinese Journal of Mechanical Engineering, 30(3), 515-527.

[4] Parthasarathy, J., Starly, B., Raman, S., & Christensen, A. (2010). Mechanical evaluation of porous titanium (Ti6Al4V) structures with electron beam melting (EBM). Journal of the mechanical behavior of biomedical materials, 3(3), 249-259.

[5] Cheng, S., & Chandra, S. (2003). A pneumatic droplet-on-demand generator. Experiments in fluids, 34(6), 755-762.

[6] Cheng, S. X., Li, T., & Chandra, S. (2005). Producing molten metal droplets with a pneumatic droplet-on-demand generator. journal of materials processing technology, 159(3), 295-302.

[7] Fang, M., Chandra, S., & Park, C. B. (2007). Experiments on remelting and solidification of molten metal droplets deposited in vertical columns. Journal of Manufacturing Science and Engineering, 129(2), 311-318.

[8] Lee, T. M., Kang, T. G., Yang, J. S., Jo, J., Kim, K. Y., Choi, B. O., & Kim, D. S. (2008). Drop-on-demand solder droplet jetting system for fabricating microstructure. IEEE Transactions on Electronics Packaging Manufacturing, 31(3), 202-210.

[9] Cao, W., & Miyamoto, Y. (2006). Freeform fabrication of aluminum parts by direct deposition of molten aluminum. Journal of Materials Processing Technology, 173(2), 209-212.

[10] Xiong, X., Zhang, H., & Wang, G. (2009). Metal direct prototyping by using hybrid plasma deposition and milling. journal of materials processing technology, 209(1), 124-130.

[11] Ando, T., Chun, J., & Blue, C. (1999). Uniform droplets benefit advanced particulates. Metal Powder Report, 3(54), 30-34.

[12] Trapaga, G., Matthys, E. F., Valencia, J. J., & Szekely, J. (1992). Fluid flow, heat transfer, and solidification of molten metal droplets impinging on substrates: comparison of numerical and experimental results. Metallurgical Transactions B, 23(6), 701-718.

[13] Noecker, F. F. I. I., & DuPont, J. N. (2002). Functionally graded copper-steel using LENS Process. Rapid Prototyping of Materials, 139-147.

[14] Matsumoto, M., Shiomi, M., Osakada, K., & Abe, F. (2002). Finite element analysis of single layer forming on metallic powder bed in rapid prototyping by selective laser processing. International Journal of Machine Tools and Manufacture, 42(1), 61-67.

[15] Peng, L., Shengqin, J., Xiaoyan, Z., Qianwu, H., & Weihao, X. (2007). Direct laser fabrication of thin-walled metal parts under open-loop control. International Journal of Machine Tools and Manufacture, 47(6), 996-1002.

[16] Liu, J. H., Shi, Y. S., Lu, Z. L., Xu, Y., Chen, K. H., & Huang, S. H. (2007). Manufacturing metal parts via indirect SLS of composite elemental powders. Materials Science and Engineering: A, 444(1-2), 146-152.

[17] Shellabear, M., Danzig, A., Heugel, M., Kotila, J., & Nyrhilä, O. (2001). The breakthrough to 20 micron layers–Increasing precision and efficiency in Direct Metal Laser-Sintering. Proceedings of the uRapid, 256-267.

Viser Technology Pte. Ltd.
Mechanical Engineering Science
https://doi.org/10.33142/me.v1i1.659

Research Article Open Access

A Prediction Method for TBM Cutterhead Dynamic Tunneling Performance under Typical Composite Geological Conditions

Jingxiu Ling [1, 2,*], Xiaojing Yang [1, 3], Zhihong Wu [2]

[1] School of Mechanical and Automotive Engineering, Fujian University of Technology, Fuzhou, China
[2] CSCEC Strait Construction and Development Co., Ltd, Fuzhou, China
[3] Mechanical Engineering Practice Training Base, Fujian University of Technology, Fuzhou, China

***Corresponding Author:** Jingxiu Ling, School of Mechanical and Automotive Engineering, Fujian University of Technology, Fuzhou, China. ljxyxj@fjut.edu.cn*

Abstract:
The cutterhead system is a core component of TBM equipment, which works in the extremely severe environment, and the strong impact loads result in severe vibration, crack, damage failure and other engineering failures. Accordingly, the key for cutterhead system structure design and parameter matching is to evaluate and predict cutterhead tunneling per-formance reasonably. In this paper, a prediction method for TBM cutterhead dynamic tunneling performance is pro-posed under the typical composite geological conditions, based on the CSM model of multi-cutters and cutter loads field test data. Then an actual TBM cutterhead of a water conservancy project is taken as an example, a spatial three-dimensional separation zone model for cutterhead tunneling is established under the typical geological condition, and the parameters influence rules of cutterhead tunneling performance are analyzed. The results show that, the cutter-head loads and specific energy change rules with different parameters are basically similar. Moreover, under the condi-tion of penetration p=10mm, the cutterhead bending moment coefficient of variation magnitude exceeds 20%, which is the maximum, and the normal cutter spacing optimal value is 95mm. Also, when the normal cutter spacing is kept constant in 85mm, the penetration has a greater influence on the torque and specific energy coefficient of variations, which is increased from 2mm to 10mm, and the two indexes decrease by about 73%. It is indicated that proper increase of pene-tration is beneficial to reduce the vibration fluctuation degree of torque and specific energy. The proposed method of TBM cutterhead dynamic tunneling performance and the analysis results can provide theoretical basis and design refer-ence for TBM cutterhead layout and tunneling parameters matching.

Keywords: *TBM cutterhead, spatial geological model, tunneling performance, parameter influence*

Citation: J.X. Ling, X.J. Yang, Z.H. Wu. A Prediction Method for TBM Cutterhead Dynamic Tunneling Performance under Typical Composite Geological Conditions. *Mech Eng Sci*, 2019,1(1): 33-41. https://doi.org/10.33142/me.v1i1.659

1. Introduction

Cutterhead system is a key working component of the full face hard rock Tunnel Boring Machine (TBM), which endures strong, random, and multi-point distributed impact loads, leading to structure vibration, fatigue, crack damage and other mechanical failures (Huo et al., 2017; Cai, et al., 2017). Hence, accurate analysis and evaluation of cutterhead loads are closely related to the whole machine control parameters matching, system dynamic as well as the key structure fatigue life prediction. Besides, it may indirectly affect the construction efficiency and safety. Moreover, the energy consumption prediction of rock breaking by cutter is also a key point of TBM. Due to the random variability of surrounding rock in excavation interface and tunneling direction, the TBM cutterhead force and load transfer condition are extremely complicated. Accordingly it is difficult to accurately evaluate the cutterhead excavation performance. However, it is necessary to predict and analyze the cutterhead dynamic excavation performance in the design stage, according to the geologic exploration report, so as to achieve the purpose of component structure optimization and tunneling parameters matching.

In view of the problems above-mentioned, relevant scholars have done a lot of research. Many researchers have proposed different prediction models to estimate the cutting forces, with the means of theoretical derivation, test and numerical simulation. Previous attempts to measure cutting forces (i.e., normal, rolling, and side force) in the field and laboratory were carried out by Samuel and Seow (1984), Rostami (1997), Zhang et al. (2003) and Gertsch et al. (2007). These studies gave valuable insight into the rock breaking mechanism and load change regulation of an individual disk cutter. However, different types of disc cutters were mounted on the cutterhead, and with different installation locations, the change regulation of cutting forces were not the same. Moreover, in all these studies, the normal disc cutters were mostly used, and the gage cutters were rarely studied. Accordingly, a new cutter force measurement method was proposed by Entacher et al. (2013), and it was implemented at Koralm tunnel. Later, a series of punch penetration tests were performed by Jeong et al. (2015), to estimate the disc cutter's normal force, and the results were validated by a LCM test. Considering the circular running path and wear of the disc cutter, a new cutter force model was developed by Yang et al. (2013), which was also compared with the classical models. Besides, with the rapid development of numerical simulation technology, many researchers carried out lots of CAE analyses to simulate the rock breaking process. A 3D FEM-SPH coupling method was applied to study the rock fragmentation mechanism by Nan et al. (2015). Meanwhile, Liu et al. (2015), Geng et al. (2017), Xia et al. (2017) and Jiang et al. (2017) respectively simulated the rock cutting process by the methods of FEM and DEM, to obtain the cutter forces and the optimal cutter spacing, as well as establish foundation for cutterhead performance prediction. Some scholars studied the rock cutting process based on numerical simulation and rotary cutting experiments (Xia et al., 2016; Geng et al., 2016), to provide reference for side force formation mechanism and cutters layout.

For a long time, many earlier models and studies have also been carried out about cutterhead loads, cutterhead system design and specific energy. Zhu et al. (2014) studied the excavating loads characteristic on TBM cutterhead, and the parameters influence on cutterhead loads was analyzed. A new cutterhead load model was established based on the CSM model and rock section circular hierarchical model, then the cutterhead force distribution under certain geology was calculated (Liu et al., 2016 and 2017). The cylinders thrust force and cutterhead loads were respectively presented by Huang et al. (2016) and Han et al. (2017), based on the theoretical derivation and simulation method, which can provide important theoretical basis and a reference for the design and parameters control during TBM construction. The cutterhead system design for the hard rock TBM was studied by Rostami (2008), and it pointed out that the cutters distribution was critical to cutterhead balance performance. A calculation model was built to study the TBM cutterhead mechanical performance in mixed rock ground conditions, and it was verified with a boring experiment (Geng et al., 2016). They also proposed a free-face-assisted rock breaking method based on a multi-stage TBM cutterhead, to improve the TBM rock breaking efficiency (Geng et al., 2016). Huo et al. (2015, 2016) studied the multi-directional coupling dynamic characteristics of TBM cutterhead system, to lay a foundation of cutterhead structural design and system parameters matching. Avunduk and Copur (2018) developed empirical performance prediction models for predicting a EPB TBM excavation performance, and field tests were carried out to validate these proposed models. The specific energy (SE) is another important performance parameter, and many scholars have studied it with different methods in different tunnels (Wang et al., 2012 ; Mirahmadi et al., 2017).

As mentioned above, scholars have studied cutter force prediction, cutterhead loads and system design, specific energy and so on, by using the methods of theoretical derivation, numerical simulation, and model experiment, as well as field test. However, in the previous studies, it was assumed that the formation was single and homogeneous or two element circular cross-section model while predicting the cutter forces. It was inappropriate since the results ignored the cutter forces impact-resistance, time variation of the cutter's surrounding rock in excavation section and the formation random variation. Besides, the rock breaking loads change is closely related to the cutter location and tunneling parameters. The dynamic parameters changes need to be considered while solving the cutterhead loads and specific energy, and then the performance indexes can be obtained. For this, in this study, a spatial three-dimensional separate surrounding rock model under an actual typical tunnel is established, based on the geological exploration data. That is, the rock physical properties in different tunneling sections are all different. Meanwhile, a prediction method for TBM cutterhead excavation performance under typical geological conditions is proposed, considering the TBM tunneling parameters, cutters position information and the dynamic changes of surrounding rock property at different time, based on the CSM model and cutter loads field test data (Samuel and Seow, 1984; Zhang, et al., 2003). In this study, the cutterhead loads and specific energy are used to quantify the excavation performance. Last，taking a water diversion project as an example, the dynamic cutter loads, cutterhead loads and specific energy are obtained with the proposed method. And the influences of normal cutter spacing and penetration on cutterhead excavation performance are analyzed, which can provide reference for TBM cutterhead layout and tunneling parameters matching.

2. Theoretical calculation model of cutterhead excavation performance

When the TBM tunnels, the cutterhead endures strong, multi-point distributed impact loads, which leads to intense vibration. After all the cutters loads are combined, the cutterhead mainly bears the thrust P_v, radial force P_r, torque T and the bending moment M, as shown in Figure 1. Accordingly, the cutterhead loads can be obtained with the information of cutters locations, installation angles and surrounding rock physical properties under the typical condition. In addition, the relational schematic diagram between the cutter force and layout position is shown in Figure 2. In this figure, the cutter normal force, tangential force and side force are denoted as F_v ,F_r and F_s , respectively, l is the cutter polar radius, θ is the cutter phase angle, and β is the installation angle of gauge cutter.

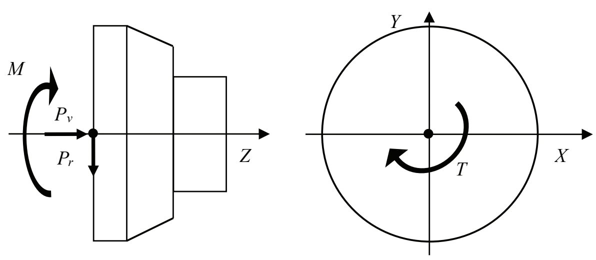

Figure 1. Cutterhead force.

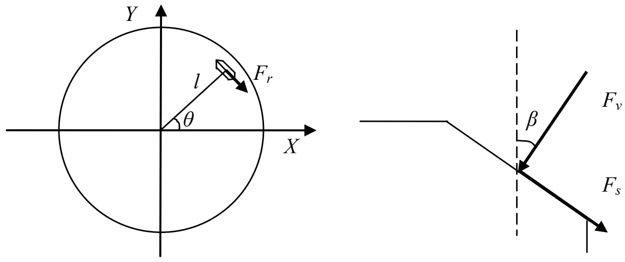

Figure 2. Cutter force and layout position.

2.1. Cutter load model

It is necessary to obtain the dynamic loads of each cutter, before solving the cutterhead loads. The cutter rock breaking force model developed at the Colorado School of Mines (CSM) was based on the experimental data, which was deduced by a regression analysis algorithm, and it had been verified in lots of projects with high precision (Rostami, 1997). However, in the CSM model, the cutter loads are static and calculated under the uniform geological condition. Actually, due to the rock inherent physical properties, the rock breaking forces are time-variant even in the uniform geologic section, which shows a certain degree of randomness. Concerning the randomness of cutter force, the test data indicated that it conformed to logarithmic normal distribution (Samuel and Seow, 1984; Zhang et al., 2003), as shown in Figure 3. Accordingly, in this study, it is assumed that the cutter force follows log-normal distribution, the mean value is calculated by CSM model, and the mean square deviation is obtained indirectly by counting the cutter force test data.

In the CSM model, the normal force F_v and tangential force F_r are expressed as follows:

$$F_v = C \cdot T \cdot R \cdot \varphi \cdot \left(\frac{\sigma_c^2 \sigma_t S}{\varphi\sqrt{RT}}\right)^{\frac{1}{3}} \cdot \cos\frac{\varphi}{2} \tag{1}$$

$$F_r = C \cdot T \cdot R \cdot \varphi \cdot \left(\frac{\sigma_c^2 \sigma_t S}{\varphi\sqrt{RT}}\right)^{\frac{1}{3}} \cdot \sin\frac{\varphi}{2} \tag{2}$$

$$\varphi = \arccos((R-p)/R) \tag{3}$$

where φ is angle of the contact area, σ_c is uniaxial compressive strength of rock, σ_t brazilian indirect tensile strength of rock, R is cutter radius, S is cutter spacing, p is cutter penetration, T is cutter tip width, C is constant equal 2.12.

2.2. Cutterhead excavation performance model

After obtaining the cutters loads, the cutterhead loads can be combined according to the cutters location information. Then according to the specific energy definition, the time history of cutterhead specific energy can be obtained. The cutter side force direction is greatly related to the rock breaking way, so the randomness is obvious. Moreover, due to the cutter layout symmetry, the side forces can be approximately counteracted. Accordingly, the side forces have little influence on the cutterhead loads, which can be ignored. Besides, the cutterhead radial force is up and down balanced with small fluctuation when the cutterhead tunnels, which is considered as a constant load and can be equivalent to the cutterhead system gravity. Hence, the cutterhead torque, thrust and bending moment characteristics are mainly studied in this paper.

2.2.1 Cutterhead torque

Cutterhead torque T is equal to the resultant torque of each tangential force around Z axial, which can be expressed as:

$$T = \sum_{i=1}^{n} F_{ri} l_i + \sum_{j=1}^{m} F_{rj} l_j + \sum_{k=1}^{q} F_{rk} l_k \tag{4}$$

where F_{rt} (t=i,j,k) is the tangential force of the t-th center cutter, normal cutter and gauge cutter, respectively, n, m and p are the number of the center cutter, normal cutter and gauge cutter, respectively, and l_t (t=i,j,k) is the polar radius of the t-th center cutter, normal cutter and gauge cutter respectively.

2.2.2 Cutterhead thrust

Cutterhead thrust P_v is equal to the resultant force in Z direction of each cutter, with the following expression:

$$P_v = \sum_{i=1}^{n} F_{vi} + \sum_{j=1}^{m} F_{vj} + \sum_{k=1}^{q} F_{vk} \cos\beta_k \tag{5}$$

where F_{vt} (t=i,j,k) is the normal force of the t-th center cutter, normal cutter and gauge cutter, respectively, and β_k is the tilt angle of the k-th gauge cutter.

2.2.3 Cutterhead bending moment

Similarly, the cutterhead bending moment M can be decomposed into two directions, which is equal to the vector sum of overturning moment M_x and M_y, with the expressions showing in Eq. (6) ~ Eq. (8).

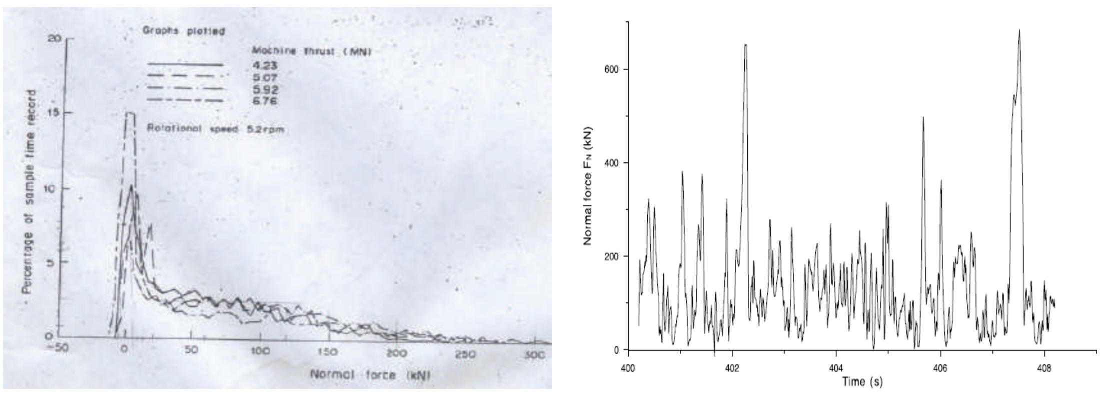

Figure 3. The measured forces of disc cutter rock crushing

$$M_x = \sum_{i=1}^{n} F_{vi} l_{ix} + \sum_{j=1}^{m} F_{vj} l_{jx} + \sum_{k=1}^{q} F_{vk} l_{kx} \cos\beta_k \tag{6}$$

$$M_y = \sum_{i=1}^{n} F_{vi} l_{iy} + \sum_{j=1}^{m} F_{vj} l_{jy} + \sum_{k=1}^{q} F_{vk} l_{ky} \cos\beta_k \tag{7}$$

$$M = \sqrt{M_x^2 + M_y^2} \tag{8}$$

where l_{tx} $(t=i,j,k)$ and l_{ty} $(t=i,j,k)$ are the distance to X and Y axis of the t-th cutter, respectively.

2.2.4 Cutterhead specific energy

The energy consumption of rock fragmentation per unit volume is defined as specific energy, which is an important basis for evaluating the cutter spacing. The cutterhead rock breaking energy is mainly produced by thrust and torque, so the specific energy E_s can be expressed as:

$$E_s = \frac{P_v p + 2\pi T}{\pi R_d^2 p} \tag{9}$$

where R_d is the tunnel excavation radius.

3. Project case

The total length of the diversion tunnel in Liaoning Dahuofang water project is 85.31km, and the project is tunneled by 3 TBM with 8.03 m excavation diameter. An American Robbins TBM is employed, with the whole machine showing in Figure 4, and the cutterhead system parameters are shown in Table 1. According to the statistics of geological exploration data, the typical soft rock and hard rock are mainly pelitic siltstone and granitic gneiss, and the rock mechanical property parameters are shown in Table 2.

Figure 4. The physical model of TBM.

3.1. Spatial geological model in mixed-face rock ground condition

Based on the geological exploration report, a separation zone model for continuous tunneling is established, and the simulation length of two typical geology models is 100m. Using an interpolation algorithm in Matlab software, a three dimensional stratigraphic separation model is obtained, as shown in Figure 5, soft rock is above the separation zone, and hard rock is under it.

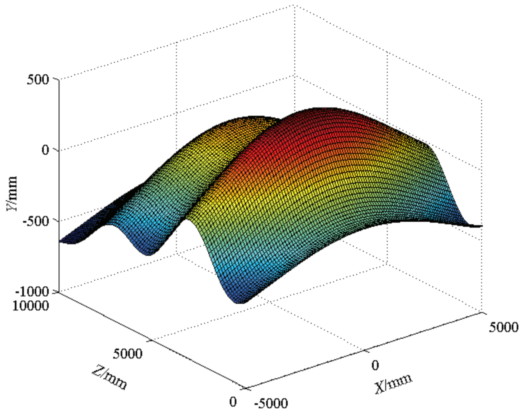

Figure 5. Geological model in typical engineering.

3.2. Numerical calculation and analysis of cutterhead loads in complex strata

The cutterhead loads numerical calculation is a process of continuously synthesizing the cutter forces and solving the cutterhead thrust, torque and bending moment, and the key step is to judge the surrounding rock property of each cutter at any time at the tunneling section in complex strata. The relative position of cutters and formation changed continually due to the cutterhead moving forward and rotating, which is the most influential factor of cutterhead loads fluctuation. Another important factor is the randomness of cutter rock breaking loads. In order to get the continuous cutterhead loads time-histories, the composite strata model and cutter position matrix are constructed, and then the numerical simulation analysis of the whole cutterhead excavation process is carried out based on the cutterhead tunneling parameters, cutter rock breaking load models and the field test data. The numerical solution process is shown in Figure 6.

3.2.1 Cutter loads

As mentioned above, based on the CSM model and cutter test loads data, the cutter loads are obtained under different conditions. With the conditions of 85mm normal cutter spacing and rated penetration, the obtained loads of 30# cutter are presented in Figure 7.

Table 1 Parameters of cutterhead system.

Cutterhead diameter /mm	Rated speed /rpm	Rated torque /kNm	Rated thrust /kN
8030	6	3490	13750
Driving power /kW	Cutter number	Cutter diameter/mm	Rated penetration /(mm/r)
3000	51	483	10

Table 2 Mechanics parameters of typical rocks.

Rock type	Density /(g/cm^3)	Compression strength/MPa	Peak shear strength		Elastic modulus /GPa	Poisson ratio
			Internal friction angle /(°)	Cohesion / MPa		
Pelitic siltstone	2.61	42	33.8	1.2	9.6	0.30
Granite gneiss	2.75	93.6	33.4	0.9	18	0.19

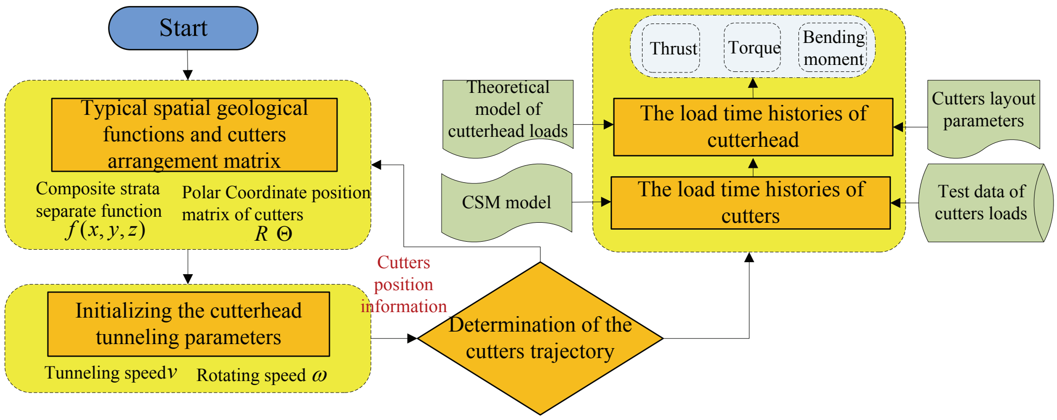

Figure 6. Numerical simulation process of cutterhead loads.

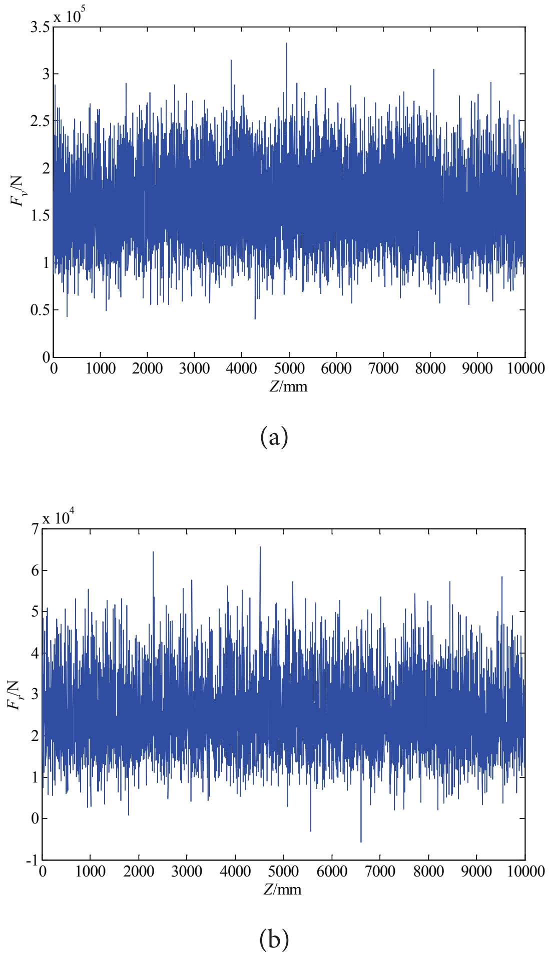

Figure 7. Loads of 30# cutter (a) Normal force. (b) Tangential force.

3.2.2 Torque characteristics

According to engineering statistics, the TBM cutterhead normal cutter spacing is generally 40mm ~ 120mm. Due to the installation position limit, the spacing less than 60mm is seldom used. Accordingly, in this paper, the range of spacing value is limited to 75mm ~115mm when the influence of cutter spacing on the cutterhead tunneling performance is analyzed. Generally speaking, the value of cutter penetration depends on the rock properties at the cutterhead tunneling section. When the rock is hard, the penetration is taken as a smaller value appropriately and vice versa. So the range of penetration is defined as 2mm~10mm in this study.

Based on the numerical simulation process of cutterhead loads in Figure 6, with the condition of penetration p=10mm, the cutterhead torque along the tunneling direction under different normal cutter spacing values is obtained after substituting each parameter into Eq. (4), as shown in Figure 8(a). Similarly, the cutterhead torque under different penetration values is calculated with the condition of normal cutter spacing S=85mm, as shown in Figure 8(b).

From the above results, when the cutter penetration p=10mm and the normal cutter spacing S=85mm, the cutterhead torque fluctuates in the range of 2500~2900kNm approximately, which is basically consistent with the field cutterhead torque value in TBM tunneling state monitoring interface (as showed in Figure 9). It shows that the cutterhead loads calculation method and simulation process are reasonable and effective.

3.3.3 Thrust characteristics

Based on the numerical simulation process in Figure 6 and Eq. (5), the influence law of the normal cutter spacing and penetration on the cutterhead thrust can be also obtained, as shown in Figure 10.

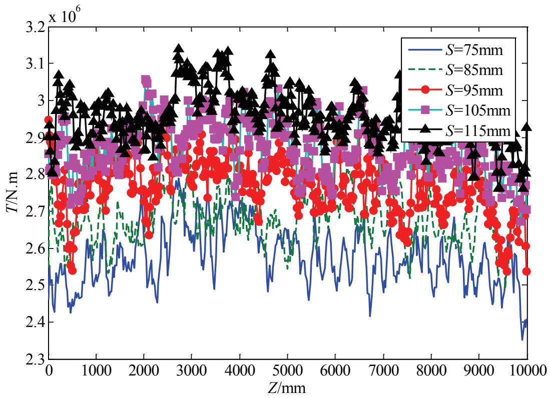

(a)

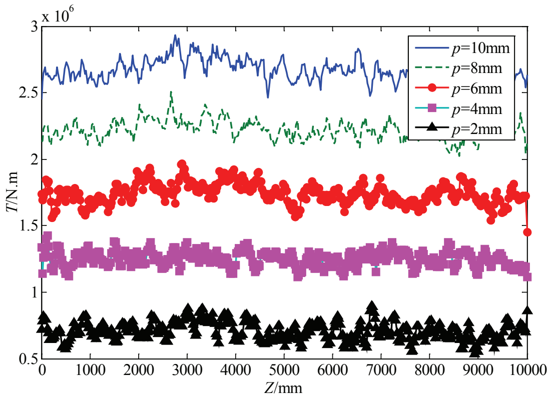

(b)

Figure 8. The influence of different parameters on cutterhead torque (a) Influence of cutter spacing (p=10mm). (b) Influence of penetration (S=85mm).

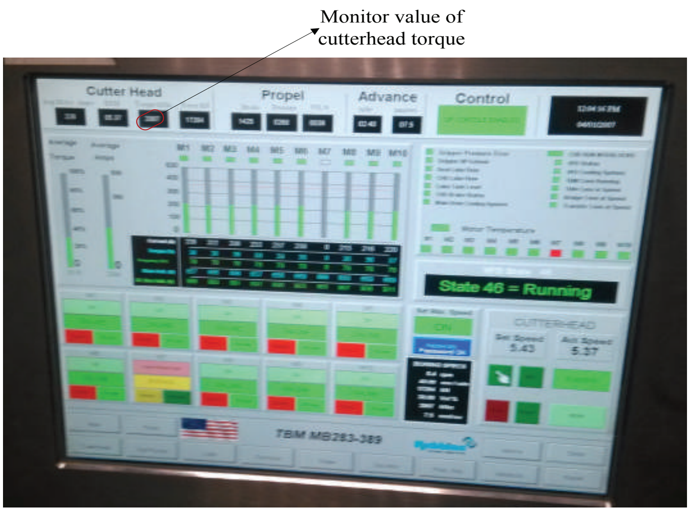

Figure 9. Tunneling state monitoring interface of field TBM.

3.2.4 Bending moment characteristics

In the same way, the influence law of the normal cutter spacing and penetration on the cutterhead bending moment are solved, as shown in Figure 11.

3.3. Specific energy characteristics

The obtained cutterhead torque and thrust, as well as the given parameters are substituted into Eq. (9), and the influence law of the normal cutter spacing and penetration on the cutterhead specific energy are analyzed, as the results shown in Figure 12.

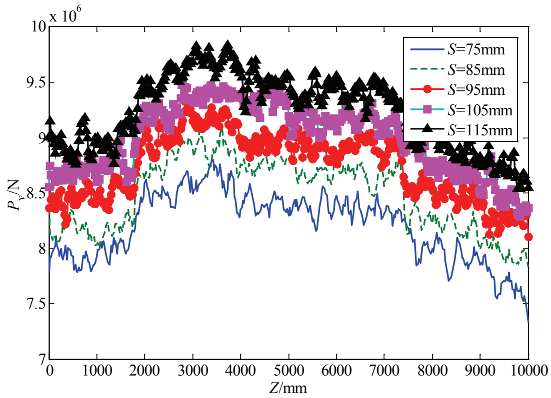

(a)

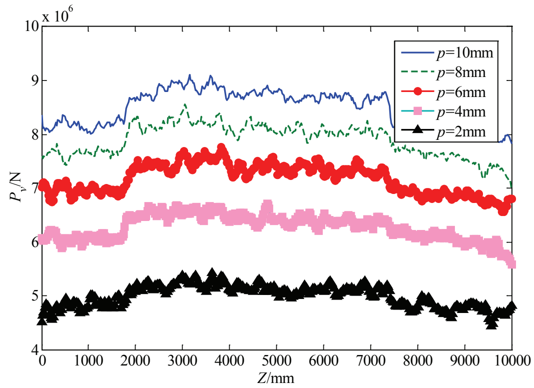

(b)

Figure 10. The influence of different parameters on cutterhead thrust (a) Influence of cutter spacing (p=10mm). (b) Influence of penetration (S=85mm).

3.4. Data statistics and analysis

In order to further analyze the influence of the normal cutter spacing and penetration on the cutterhead performance, the mean value, standard deviation and coefficient of variation under different cutter spacing and penetration values are counted, with the statistical results showing in Table 3 and Table 4, respectively.

From the cutterhead tunneling performance influence rule and statistical results can be known:

(1) From Figure 8 ~ Figure 12 can be seen, the change regulation of the cutterhead tunneling performance under different normal cutter spacing and penetrations is basically identical, and the performance curves with each parameter show strong randomness.

(2) From the statistical data in Table 3 can be found, the cutterhead performance mean value increases with the normal cutter spacing. Under the working condition of penetration p=10mm, the normal cutter spacing is increased from 75mm to 115mm (increased about 53%), and the increase values of cutterhead torque and specific energy mean values are the maximum, which is about 15%. Then the bending moment mean value increases about 14.7%. Last, the thrust mean value increases about 12.6%.

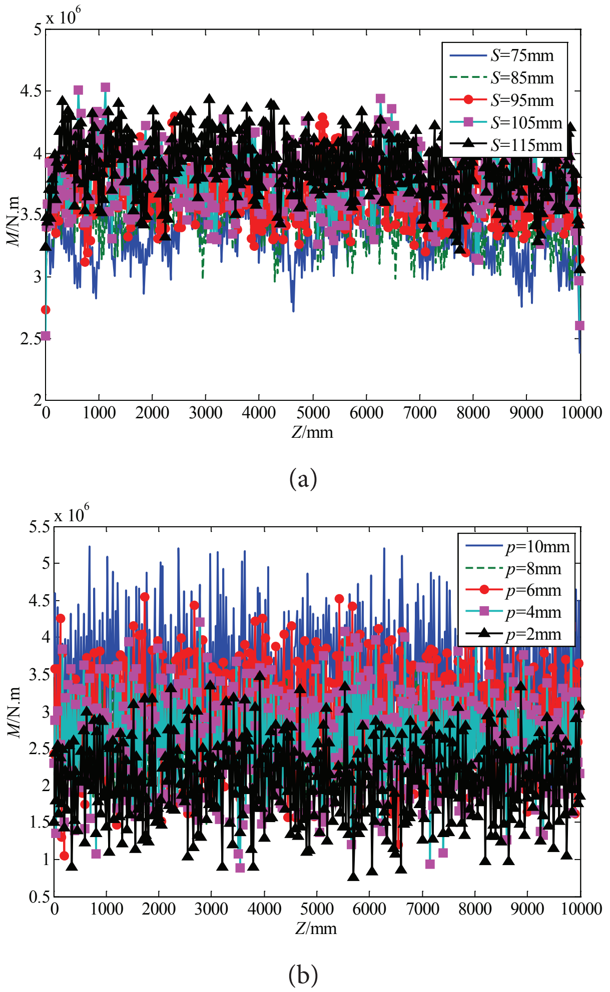

Figure 11. The influence of different parameters on cutterhead bending moment (a) Influence of cutter spacing (p=10mm). (b) Influence of penetration (S=85mm).

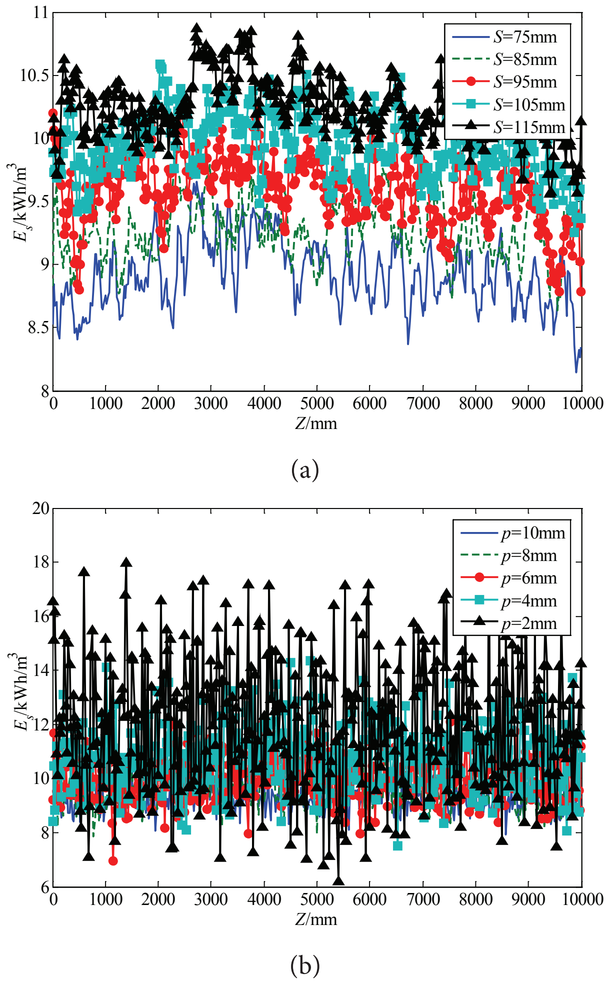

Figure 12. The influence of different parameters on cutterhead specific energy (a) Influence of cutter spacing (p=10mm). (b) Influence of penetration (S=85mm).

(3) From the statistical data in Table 4 can be known, the cutterhead torque, thrust and bending moment mean values are all increased with the penetration, yet the specific energy mean value is decreased with it. With the normal cutter spacing keeping constant in 85mm, when the penetration increases from 2mm to 10mm, the increase value of torque mean value is the maximum, which increases about 3.8 times. And the mean values increment of thrust and bending moment are almost equal, which are about 69.7% and 68.1%, respectively. In addition, the cutterhead specific energy mean value decreases by about 23.3%.

(4) The change regulations of cutterhead tunneling performance standard deviations with normal cutter spacing and penetration can also be known from Table 3 and Table 4. The cutterhead thrust and bending moment standard deviations show positive correlation with the two parameters, and the cutter spacing value increases by 53%, thrust and bending moment standard deviations increase by about 4.2% and 9.4%, respectively. Moreover, the penetration increases from 2mm to 10mm, thrust and bending moment standard deviations increase by about 43%and 45.6%, respectively. Besides, with the increase of normal cutter spacing, the cutterhead torque standard deviation shows a trend of first increase and then decrease. But with the increase of penetration, it presents an opposite tendency. With regard to the cutterhead specific energy standard deviation, it also shows a trend of first increase and then decrease with the increase of normal cutter spacing, and it shows an inverse correlation with penetration.

(5) Under the condition of penetration p=10mm, the cutterhead bending moment coefficient of variation magnitude are greater than other indexes, which is more than 20%, and the values of other indexes are about 5%. It indicates that the unit average dispersion degree of bending moment is the maximum. In addition, with the increase of normal cutter spacing, almost all the indexes coefficient of variation decreases in different degrees except the bending moment. When the normal cutter spacing is equal to 95mm, the bending moment coefficient of variation is the minimum. From the point view of reducing the average vibration intensity of cutterhead bending moment, it demonstrates that the optimal value of normal cutter spacing is 95mm under this condition.

(6) When the normal cutter spacing is equal to 85mm, with the increase of penetration, the cutterhead thrust and bending moment coefficient of variations are basically remain unchanged, which indicates that the penetration has little effect on the average dispersion degree of the two indexes. However, the penetration has a great impact on the cutterhead torque and

specific energy coefficient of variations. The penetration is increased from 2mm to 10mm, the two coefficient of variations all decrease by about 73%. It shows that proper increase of penetration is beneficial to reduce the average vibration intensity of cutterhead torque and specific energy.

4 Conclusions

A spatial three-dimensional separation zone model for cutterhead tunneling under the typical geology is established, based on the geological exploration data of TBM tunneling sections. Then a prediction method of TBM cutterhead dynamic tunneling performance under the typical geological conditions is proposed, which comprehensively considers the tunneling parameters, cutter layout information and the tunneling section rock dynamic changes, on the basis of the multi-cutters CSM model and field test statistic data. Last, taking an actual TBM cutterhead system as an example, the proposed prediction method is used to program a numerical simulation process for cutterhead dynamic loads, and the dynamic cutters loads, cutterhead tunneling loads and specific energy are obtained. Besides, the influences of the normal cutter spacing and penetration on the cutterhead performance are analyzed, and a series of qualitative and quantitative conclusions are obtained. The main conclusions can be drawn as follows:

(1) The change laws of cutterhead tunneling performance curves with different parameters are basically identical.

(2) The cutterhead loads have a positive correlation with the normal cutter spacing and penetration, and the specific energy is positively related to the normal cutter spacing but negatively related to penetration.

(3) Under the working condition of penetration p=10mm, the cutterhead bending moment coefficient of variation magnitude exceeds 20%, and the optimal value of the normal cutter spacing is 95mm at this situation.

(4) When the normal cutter spacing is equal to 85mm, the penetration has a greater influence on the torque and specific energy coefficient of variations, which indicates that proper increase of penetration is beneficial to reduce the average vibration intensity of the two indexes. The proposed prediction method of TBM cutterhead dynamic tunneling performance and the engineering practice numerical analysis results can provide reference for TBM cutterhead layout and tunneling parameters matching.

Acknowledgements This work is financially supported by the National Natural Science Foundation of China (51775113),the Natural Science Foundation of Fujian Province, China (2017J01675), and Scientific Research Foundation of Fujian University of Technology (GY-Z160048).

Conflict of interest The authors declare that they have no conflict of interest.

References

[1] Huo J. Z., Wu H. Y., Sun W., Zhang Z.G., Wang L. P., Dong J.H., 2017. Electromechanical coupling dynamics of TBM main drive system. Nonlinear Dynamics, 90, 2687-2710.

[2] Chai B. M., Bai Y. L., Liu J. Q., Li L. L., 2017. Research on multiple damage of remanufacturing TBM cutterhead. Journal of Hebei University of Engineering (Natural Science Edition), 34, 109-112.

[3] Samuel A.E., Seow L.P., 1984. Disc force measurements on a full-face tunnelling machine. International Journal of Rock Mechanics & Mining Sciences & Geomechanics Abstracts, 21,83-96.

[4] Rostami J., 1997. Development of a force estimation model for rock fragmentation with disc cutters through theoretical modeling and physical measurement of crushed zone pressure. Colorado: Colorado School of Mines. Department of Mining Engineering.

[5] Zhang Z.X., Kou S.Q., Lindqvist P.A., 2003. In-situ measurements of cutter forces on boring machine at Äspö hard rock laboratory part II. characteristics of cutter forces and examination of cracks generated. Rock Mechanics & Rock Engineering, 36, 63-83.

[6] Gertsch R., Gertsch L., Rostami J., 2007. Disc cutting tests in Colorado Red Granite: Implications for TBM performance prediction. International Journal of Rock Mechanics & Mining Sciences, 44, 238-246.

[7] Entacher M., Winter G., Galler R.,2013. Cutter force measurement on tunnel boring machines-Implementation at Koralm tunnel. Tunnelling & Underground Space Technology Incorporating Trenchless Technology Research, 38, 487-496.

[8] Jeong H. Y., Cho J. W., Jeon S., Rostami J., 2015. Performance assessment of hard rock TBM and rock boreability using punch penetration test. Rock Mechanics & Rock Engineering, 49, 1-16.

[9] Yang H., Wang H., Zhou X., 2016. Analysis on the rock-cutter interaction mechanism during the TBM tunneling process. Rock Mechanics & Rock Engineering, 49,1073-1090.

[10] Xiao N., Zhou X. P., Cheng H., Zhai S.F., 2015. Mechanism of rock fragmentation by TBM cutters using 3D FEM-SPH coupling method. Journal of China Coal Society, 40, 1263-1269.

[11] Liu J. Q., Liu M. M., Guo W., 2015. Research on the simulation of cutting rock rotary by hard rock tunnel boring machine disc cutters. Journal of Mechanical Engineering, 51,199-205.

[12] Geng Q., Wei Z., Ren J.,2017. New rock material definition strategy for FEM simulation of the rock cutting process by TBM disc cutters. Tunnelling & Underground Space Technology, 65,179-186.

[13] Xia Y. M., Guo B., Cong G. Q., Zhang X. H., Zeng G. Y.,2017. Numerical simulation of rock fragmentation induced by a single TBM disc cutter close to a side free surface. International Journal of Rock Mechanics & Mining Sciences, 91, 40-48.

[14] Jiang M., Liao Y., Wang H.,2017. Distinct element method analysis of jointed rock fragmentation induced by TBM cutting. European Journal of Environmental & Civil Engineering, 7,1-20.

[15] Xia Y. M., Tian Y. C., Tan Q., Hou Y. M.,2016. Side force formation mechanism and change law of TBM center cutter. Journal of Central South University, 23,1115-1122.

[16] Geng Q., Wei Z., Meng H., 2016. An experimental research on the rock cutting process of the gage cutters for

rock tunnel boring machine (TBM). Tunnelling and Underground Space Technology, 52,182-191.

[17] Zhu X. H.,2014. Research on distribution characteristic of excavation load on TBM cutterhead. Changsha: Central South University.

[18] Liu J., Ren J., Wei G.,2015. Thrust and torque characteristics based on a new cutter-head load model. Chinese Journal of Mechanical Engineering, 28, 801-809.

[19] Liu J. Q., Bin H. C., Guo W.,2019. Study on load characteristics of TBM cutterhead under mixed-face rock ground condition. Journal of Harbin Engineering University, doi:10.11990/jheu.201609049.

[20] Huang T., Wang X. L., Liu H. T., Yang Y. H., 2016. Force analysis of an open TBM gripping-thrusting-regripping mechanism. Mechanism & Machine Theory, 98,101-113.

[21] Han M.D., Cai Z. X., Qu C. Y., Jin L. S.,2017. Dynamic numerical simulation of cutterhead loads in TBM tunneling. Tunnelling & Underground Space Technology, 70, 286-298.

[22] Rostami J.,2008. Hard rock TBM cutterhead modeling for design and performance prediction. Geomechanics & Tunnelling, 1,18-28.

[23] Geng Q., Wei Z. Y., Meng H., Francisco J. M., 2016. Mechanical performance of TBM cutterhead in mixed rock ground conditions. Tunnelling & Underground Space Technology Incorporating Trenchless Technology Research, 57,76-84.

[24] Geng Q., Wei Z. Y., Meng H., Francisco J. M., Amund B.,2016.Free-face-assisted rock breaking method based on the multi-stage tunnel boring machine (TBM) cutterhead. Rock Mechanics & Rock Engineering, 49,4459-4472.

[25] Huo J. Z., Wu H. Y., Yang J., Sun W., Li G. Q., Sun X. L.,2015. Multi-directional coupling dynamic characteristics analysis of TBM cutterhead system based on tunnelling field test. Journal of Mechanical Science and Technology, 29,3043-3058.

[26] Huo J. Z., Hou N., Sun W., Wang L.P., Dong J.H., 2016. Analyses of dynamic characteristics and structure optimization of tunnel boring machine cutter system with multi-joint surface. Nonlinear Dynamics, 1,1-18.

[27] Avunduk E., Copur H.,2018. Empirical modeling for predicting excavation performance of EPB TBM based on soil properties. Tunnelling & Underground Space Technology, 71,340-353.

[28] Wang L.H., Kang Y.L., Cai Z.X., Zhao Y., Zhao H.F., Su P.C.,2012. The energy method to predict disc cutter wear extent for hard rock TBMs. Tunnelling & Underground Space Technology Incorporating Trenchless Technology Research, 28,183-191.

[29] Mirahmadi M., Tabaei M., Dehkordi M. S.,2017. Estimation of the specific energy of TBM using the strain energy of rock mass, case study: Amir-Kabir water transferring tunnel of Iran. Geotechnical and Geological Engineering, 35,1991-2002.

Viser Technology Pte. Ltd.
Mechanical Engineering Science
https://doi.org/10.33142/me.v1i1.660

Research Article Open Access

Optimization of the Hot Pressing Process for Preparing Flax Fiber/PE Thermoplastic Composite

Yiqi Wang[1*], Guangpeng Cui[1], Zhujian Shao[1], Yongjie Bao[2], Hang Gao[1]

[1] Key Laboratory for Precision and Non-traditional Machining Technology of Ministry of Education, Dalian University of Technology, Dalian 116024, China
[2] Marine engineering college, Dalian Maritime University, Dalian 116026, China

***Corresponding Author:** Yiqi Wang, Dalian University of Technology, Dalian 116024, China; wangyiqi@dlut.edu.cn*

Abstract:
The hot pressing process parameters were optimized to prepare flax fiber reinforced polyethylene (PE) thermoplastic composite by the Taguchi method. The optimal hot pressing process parameters were determined to increase the tensile strength of the composite. The optimal parameters of the design include the following sections: hot pressing temperature, pressure, hot pressing time and coupling agent modification time. An L_9 (3*4) orthogonal matrix based on the Taguchi method was created. By means of analysis of signal-to-noise ratio and analysis of variance, the optimal hot pressing process parameters combination was found, compared to the average tensile strength in the nine design experiments, and the tensile strength was improved nearly 10%.

Keywords: *flax fiber; hot pressing process; optimization; Taguchi method; ANOVA*

Citation: Y.Q. Wang, et al., Optimization of the Hot Pressing Process for Preparing Flax Fiber/PE Thermoplastic Composite. *Mech Eng Sci*, 2019,1(1): 42-47. https://doi.org/10.33142/me.v1i1.660

1. Introduction

In recent years, with global energy shortages and environmental pollution, fiber-reinforced composite materials are gradually developing towards a green ecology [1-10]. Natural fiber reinforced composites with the characteristics of low cost and recyclability are used to replace other synthesized fiber reinforced composites [1–3]. The good mechanical properties is showed by composite reinforced with natural fibers [5]. As a kind of natural fiber, flax fibers have several advantages: low density [6], high Young's modulus [2], biodegradability relatively high tensile and flexural modulus [7], and it shows the same outstanding performance as glass fiber reinforced plastics [8–10]. At the same time, thermoplastic resin is superior to thermosetting compound in terms of its excellent characteristics. The thermoplastic resin is used widely as the matrix material for environmental protection. Because the polymerization reaction has been completed before the impregnation, the hot pressing process is completely a physical process, and compared with the thermosetting resin, there is no environmental pollution problem, and it is called a green material of the 21st century [11].

By reading a wide range of literature to study green composite or reinforced biocomposite [5-9]. With the help of hot pressing process, flax fiber and polypropylene (PP) were used as raw materials to prepare composite materials. The influence of hot pressing parameters (temperature and hot pressing time) on the mechanical properties of the composite plate was analyzed by orthogonal design. The optimal solution was obtained by the range analysis and variance analysis. It found that the mechanical properties of flax fiber/PP composite were the best with the hot pressing temperature of 180°C and hot pressing time of 40min [12]. When the flax fiber has a content of 30 and 40wt.%, the strength of the flax/PLA (polylactic acid) composite is 50% better than flax/PP composites [13]. The Flax fiber/PLA Through the analysis of peeling test and tensile test, the optimum hot pressing parameters of the flax fiber/PP composite were that pressing temperature was 180°C, hot pressing time was 5min and hot pressing pressure was 6MPa [14]. For bamboo fiber/PP composite, by analysis of tensile strength and flexural strength. 170**°C, 3**MPa and 140s are optimum hot pressing process parameters [15]. In addition, the optimum hot pressing parameters of other plant fiber composite are temperature 179°C and pressure 178bar [16].

Besides the basic hot pressing parameters, in order to obtain better mechanical properties, flax fibers need to be modified during hot pressing. Coupling agents are also important for enhancing the mechanical properties of natural fiber thermoplastic composite. Some studies showed that the cellulose/PP composite which the fiber modified with the maleic anhydride-polypropylene copolymer can increase the tensile strength by 80% [17]. Mo [18] studied the effect of ramie short fibers surface KH-550 modification on the interlaminar fracture toughness of laminates. Besides the silane coupling agent was used to modify aramid. The contact angle test shows that the contact angle of the modified aramid becomes smaller, indicating that the KH550 silane coupling agent can be improved the hydrophilicity of aramid [19]. It found that alkali modification improved the compatibility between jute fiber and matrix, and their interface bonding strength. The mechanical properties of jute fiber reinforced composites after alkali modification are better than unmodified composite [20]. Tensile tests have been performed for evaluated the tensile strength of flax fiber reinforced composites. The Max. tensile strengths for linear low density polyethylene and its related composites reinforced by flax fibers were about 13.40MPa and the 14.30MPa [21], which were about 19.50MPa and the 20.50MPa for the cases of high density polyethylene and its related composites reinforced by flax fibers [22].

The flax fiber and PE that has low cost and can be decomposed are chosen as the raw material. Besides, the flax fiber/PE thermoplastic composite have a wide range of applications.
Many attempts have been made to study the hot pressing process of natural fiber composite materials. The most important of these is the optimal design of the pressing parameters. In addition to the traditional hot pressing parameters, fiber modification is also considered to enhance the mechanical properties of the composite plate. The selection of hot pressing parameters involves four parts: hot pressing temperature, hot pressing pressure, hot pressing time and coupling agent modification time. Reasonable adjustment of the size of the four parameters is critical to the quality of the specimen. In order to find suitable hot pressing parameters, the hot pressing experiment was carried out using the Taguchi method.

The experimental factors include four hot pressing parameters, and there are three levels in the each parameter. The L_9 (3*4) orthogonal experimental table was designed. Signal-to-noise (S/N) ratio analysis and analysis of variance (ANOVA) were carried out to determine the influence of different hot pressing parameters on the tensile strength of the specimen and the optimal experimental parameters.

2. Experimental procedure

2.1 Experimental details

As shown in Figure 1, there are flow chart of hot pressing process and material property characterization. The flax fiber and PE film were used as raw material to prepare fiber/PE thermoplastic composite, the hot pressing process was applied with the help of hot pressing machine to prepare composite plate. After that, the composite specimens were prepared with the size of 100mm×10mm×3mm, the tensile test was performed following by ASTM. The cross section of morphology of composite specimens were observed by SEM (scanning electron microscope).

The Taguchi method was originally established to reduce the number of experiments, and the design of experiments (DOE) were designed to find the best process parameters [23]. The DOE was realized by the matrix tool. The S/N ratio and the ANOVA are two important tools for Taguchi method analysis. They can be used to determine the optimal parameters and the influence of various experimental factors on the optimal parameters [24-25].

The hot pressing process of the material is completed by using a hot press machine. The setting of the hot pressing parameters was designed by the Taguchi method. The mechanical properties of the specimens were tested by a universal tensile machine with a tensile rate of 1 mm/min.

The main parameters in the hot pressing process include hot pressing temperature (A), hot pressing pressure (B) and hot pressing time (C). Because the flax fiber composite itself has poor adhesion to fibers and resins, it is necessary to modify the flax fiber with a silane coupling agent to enhance the cross-sectional bonding property. Thus, another parameter modification time (D) by silicon coupling agent is studied. As shown in the Table 1, there are four hot pressing parameters and three levels for each hot pressing parameter.

Table 1. Hot pressing process parameters and corresponding levels

Parameters	Unit	Level 1	Level 2	Level 3
A (hot pressing temperature)	°C	120	130	140
B (hot pressing time)	h	0.25	0.50	0.75
C (pressure)	MPa	1.00	1.50	2.00
D (modification time)	h	0.50	1.00	2.00

According to the Taguchi method, an orthogonal matrix of L_9 (3*4) was used as shown in Table 2, it contains nine hot pressing experiments.

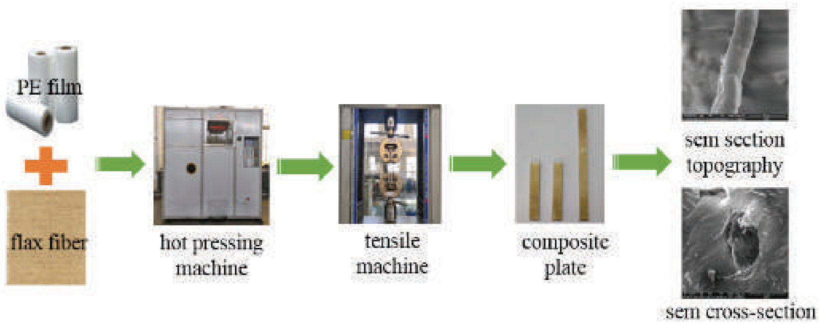

Figure 1. The flow chart of hot pressing process and material property characterization

Table 2. An L_9 (3*4) orthogonal array of the Taguchi method

Number of experiments	Parameters				
	A	B	C	D	Tensile Strength /MPa
No. 1	120	0.25	1.00	0.50	23.83
No. 2	120	0.50	1.50	1.00	23.45
No. 3	120	0.75	2.00	2.00	26.42
No. 4	130	0.25	1.50	2.00	24.38
No. 5	130	0.50	2.00	0.50	25.18
No. 6	130	0.75	1.00	1.00	22.03
No. 7	140	0.25	2.00	1.00	25.64
No. 8	140	0.50	1.00	2.00	22.33
No. 9	140	0.75	1.50	0.50	22.11

3. Results and discussion

3.1 Analysis of the S/N ratio

Through the S/N ratio, the influence of each experimental factor on the response value can be analyzed and the optimal experimental parameters can be predicted. Besides, smaller-is-better (Eq. (1)), larger-is-better (Eq. (2)) and nominal-is-the best (Eq. (3)) are used to calculate the S/N ratio.

$$\eta = -10\log\frac{1}{n}\left(\sum_{i=1}^{n} y_i^2\right) \quad (1)$$

$$\eta = -10\log\frac{1}{n}\left(\sum_{i=1}^{n} 1/y_i^2\right) \quad (2)$$

$$\eta = 10\log\frac{1}{n}\left(\sum_{i=1}^{n} y_i^2/s^2\right) \quad (3)$$

and η is mean the S/N ratio, n represents the number of experiments, y_i represents the response value of i^{th} experiment, and s is square error. In this study, tensile strength was used as an optimized response. The greater the tensile strength, the better the mechanical properties of the plate, so the second formula is chosen.

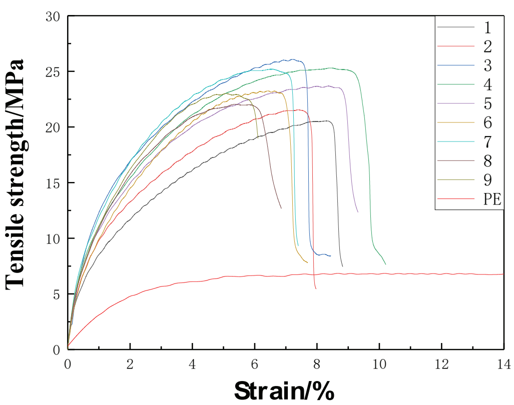

Figure 2. Stress-strain curves for flax fiber/PE composite specimens and pure resin specimens

As shown in the Figure 2, the average of the results of the three tensile specimens under each hot pressing parameter and the average of the tensile results of the pure PE resin specimens were used for comparative analysis. The flax fiber reinforced thermoplastic composite specimens has higher tensile strength than pure PE resin specimens, the average stress is 23.93MPa, and the tensile strength of the pure PE resin specimen is 7.87MPa. However, the pure PE resin specimens have larger strain than flax fiber/PE composite tensile specimens.

The results of the signal to noise ratio are shown in Table 3. According to Table 3, for tensile strength, the best combination of parameters: the hot pressing temperature is 120 °C, the hot pressing time is 0.25 h, and the hot pressing pressure is 2.00MPa, silane coupling agent modified the flax fiber for 2.00 h.

Table 3. The S/N response table (larger-is-better) for tensile strength

Level	Parameters			
	A	B	C	D
1	27.79	27.82	27.13	27.49
2	27.54	27.47	27.35	27.48
3	27.35	27.40	28.21	27.72
Delta (Δ)	0.45	0.42	1.09	0.24
Rank	2	3	1	4

3.2 Analysis of variance (ANOVA)

As shown in the Table 4, the ANOVA are also used to analysis the influence of each experimental factor on the response value. Besides, the percentage of contribution (P%) of variance and p-value are the important for the ANOVA to analyze experiment. The analysis and calculation of Taguchi experiment can refer to these two books [26, 27]. The sequential sums of squares (*Seq SS*) and adjusted sums of squares (*Adj SS*) of experiment factor k are given by

$$Seq\,SSk = Adj\,SSk = \sum_{i=1}^{n} 3\left[(mk)l - m\right]_l^2 \quad (4)$$

The formula of the adjusted mean square (Adj *MS*) and the F-statistic (F) are given by

$$F = \frac{Adj\,SS_k}{DF_k} \div \frac{Seq\,SS}{DF_E} \quad (5)$$

$$Adj\,MS_k = \frac{Adj\,SS_k}{DF_k} \quad (6)$$

and E is mean error, SS_T represents the total sum of squares given by

$$SS_T = \sum_{i=1}^{n} (\eta_i - m)^2 \quad (7)$$

The formula of the percentage contribution of the different factors to the response value is given by

$$P = \frac{SS_k}{SS_T} \times 100 \quad (8)$$

From the analysis of variance in Table 4, it was found that, there are differences in the magnitudes of the four P (%) of A, B, C, and D. According to the magnitude of the P (%), it can be inferred that the contribution of the four hot pressing parameters to the tensile strength is that: C>A>B>D. Combined with the above analysis, the optimal hot pressing process parameters are A1B1C3D3.

3.3 Microstructure

As shown in the Figure 3, there are flax fiber on the section morphology of the specimens after tensile, three microscopic pictures of tensile sections with different modification times were used as controls. It can found that more matrix attached to the surface of flax fiber with the extension of the modification time with the coupling agent. Because the coupling agent modification changes the functional group on the surface of the fiber, which made the fiber and matrix have better bonding.

In addition to modification time with the coupling agent, hot pressing temperature and pressure also have a great influence on microstructure, as shown in the Figure 4. No. 3 has more pressure than No. 1, and the gap between the fiber and matrix is smaller, so the combination is closer. No. 8 has a higher temperature than No. 1, and the gap between the fiber and matrix is smaller, so the combination is closer. From the above observation, it found that the PE matrix can be more easily filled into the fiber bundle in the higher hot pressing temperature and pressure. Because the higher temperature reduces the viscosity of the matrix, it has better mobility, and under the higher pressure, it is easier to immerse into the inside of the fiber bundle and reduce the internal gap of the fiber bundle.

Table 4. Summary of ANOVA results for tensile strength

	DF	Seq SS	Adj SS	Adj MS	F	P (%)	p-Value
A	1	2.1814	2.1814	2.1841	109.20	10.58	0.061
B	2	2.1485	2.1485	1.0742	53.71	10.42	0.096
C	2	15.3617	15.3617	7.6808	384.04	74.54	0.036
D	2	0.8978	0.8978	0.4489	22.45	4.36	0.148
Error	1	0.02	0.02	0.02		0.10	
Total	8	20.6120	20.6120			100	

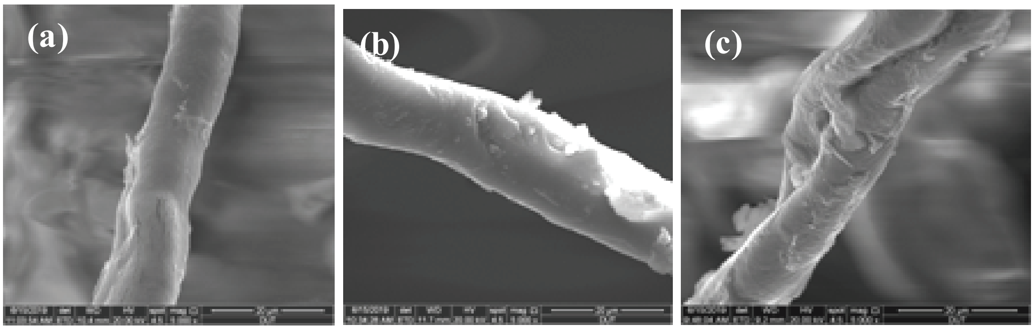

Figure 3. SEM images of flax fiber in composite (a) no modification, (b) with 0.50 h modification, and (c) with 2.00 h modification by the silane coupling agent

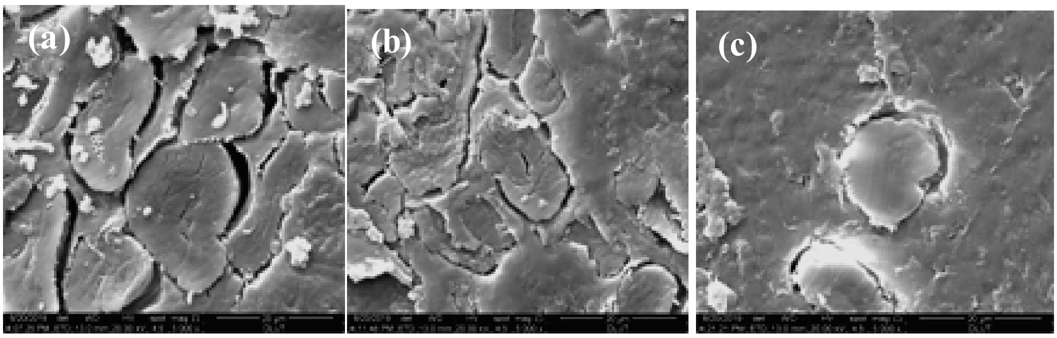

Figure 4. SEM images of composite cross section prepared at different processing conditions: (a) No. 1, (b) No. 3, and (c) No. 8

3.4 Verification experiment

Verification experiments are very important in engineering analysis. The optimization results can be verified by the four hot pressing parameters. The verification experiment was carried out by using the best hot pressing process A1B1C3D3. To obtain the maximum tensile strength produced by the optimization process. Base on the systematical and scientific study, the tensile strength of the flax/PE thermoplastic composite material made by other researchers were about 20MPa [21-22], and it was improved to 27MPa, which was increased more than 30% by our optimization method. Results show that the hot pressing process parameters can be optimized effectively by the Taguchi method. It can effectively improve the tensile strength of flax fiber thermoplastic composite.

4. Conclusion

The Taguchi method was proposed to determine the optimal hot pressing process parameters which improved the tensile strength of the test composite specimen. In total, nine experiments were performed using an L_9 (3*4) orthogonal matrix, four hot pressing parameters were chosen as design parameters, and each hot pressing parameter had three levels. Besides, the S/N ratio and ANOVA were calculated for the optimization. The validation experiment was performed to verify the best parameters which can improve tensile strength. Through the analysis of the optimization of the hot pressing process, the following conclusions can be drawn:

(1) Through the analysis of the S/N ratio, the optimal hot-pressure parameters are suggested as: the hot pressing temperature is 120 °C, the hot pressing time is 0.25 h, and the hot pressing pressure is 2.00MPa. The silane coupling agent modified the flax fiber for 2.00 h. Analysis of variance results showed that, the contribution of the four factors to the tensile strength of the panel is: C>A>B>D, combined noise ratio analysis, the final hot pressing optimization parameter is: A1B1C3D3.

(2) The optimal hot pressing process parameter verification results show that, compared to the average tensile strength, the tensile strength under the optimal parameters is improved about 10%. The Taguchi method effectively increase the tensile strength of flax fiber thermoplastic composite.

(3) Combined with hot pressing parameters and microstructure pictures, as can be seen, coupling agent modification can enhance the degree of fiber and matrix bonding, so it make the fiber surface have more matrix adhesion. The temperature and pressure work together to fill the PE matrix into the fiber bundle, high temperature reduces the viscosity of the matrix, so that it has better mobility, and under the larger pressure, it is easier to immerse into the inside of the fiber bundle. The hot pressing time has little effect on the performance of the specimen.

Acknowledgments: This work was supported by the National Natural Science Foundation of China (NSFC) [grant nos. 51605076, 51875079], and the Fundamental Research Funds for the Central Universities [grant no. DUT18LAB18].

References

[1] Witik RA, Payet J, Michaud V, et al. Assessing the life cycle costs and environmental performance of lightweight materials in automobile applications. Composite Part A: Applied Science and Manufacturing 2011; 42(11): 1700–1709.

[2] Oksman K, Skrifvars M, Selin JF, et al. Natural fibers as reinforcement in polylactic acid (PLA) composite. Composite Science and Technology 2003; 63(9): 1317–1324.

[3] Joshi SV, Drzal LT, Mohanty AK, et al. Are natural fiber composites environmentally superior to glass fiber reinforced composites? Composites Part A: Applied Science and Manufacturing. 2004; 35(3): 370–376.

[4] 4 Snoeck D, Belie ND. Mechanical and self-healing properties of cementitious composite reinforced with flax and cottonised flax, and compared with polyvinyl alcohol fibers. Biosystems Engineering 2012; 111: 325–350.

[5] Charlet K, Beakou A. Mechanical properties of interfaces within a flax bundle – Part I: Experimental analysis. International Journal of Adhesion and Adhesives 2011; 31: 875–890.

[6] Shah DU, Porter D, Vollrath F, et al. Can silk become an effective reinforcing fibers? A property comparison with flax and glass reinforced composite. Composite Science and Technology 2014; 101: 173–183.

[7] GARKHAIL SK, HEIJENRATH RWH, PEIJS T. Mechanical Properties of Natural-Fibre-Mat-Reinforced Thermoplastics based on Flax Fibres and Polypropylene. Applied Composite Materials 2000; 7: 351–372.

[8] Woigk W, Fuentes CA, Rion J, et al. Interface properties and their effect on the mechanical performance of flax fiber thermoplastic composite. Composite Part A: Applied Science and Manufacturing 2019; 122: 8–17.

[9] Dicker MPM, Duckworth PF, Baker AB, et al. Green composite: a review of material attributes and complementary applications. Composite Part A: Applied Science and Manufacturing 2014; 56: 280–291.

[10] Duc F, Bourban PE, Plummer CJG, et al. Damping of thermoset and thermoplastic flax fiber composite. Composite Part A: Applied Science and Manufacturing 2014; 64: 115–230.

[11] Zhang W, Huang S. Hemp fiber reinforced thermoplastic composite material and its development and application. FRP/composite 2010; 2(03): 81–83.

[12] Fu CL, Wang XL, Cui P, et al. Performance comparison of three kinds of plant fiber/polypropylene composite. Journal of Textile Science and Engineering 2018; 35(03): 110–112.

[13] Oksman K, Skrifvars M, Selin JF. Natural fibers as reinforcement in polylactic acid (PLA) composites. Composites Science and Technology 2003; 63: 1317–1324.

[14] Yang B, Wang JY, Yan BJ, et al. Preparation and Mechanical Properties Analysis of Jute Fiber/ES Fiber Composite. Shanghai Textile Technology 2017; 45(06): 26–29.

[15] Yan TH. Research on molding process and properties of flax thermoplastic reinforced composite. Shanghai: Dong hua University, 2009. 50–86.

[16] Liu TS. Research on Dry Hot Pressing Process Optimization and Molding Equipment for Plant Fiber Tableware. China Academy of Agricultural Mechanization Sciences 2009; 40: 200–218.

[17] Arbelaiz A, Ferna´ndez B, Ramos JA, et al. Mechanical properties of short flax fibre bundle/polypropylene composites: Influence of matrix/fibre modification, fibre content, water uptake and recycling. Composites Science and Technology 2005; 65: 1582–1592.

[18] Mo ZC, Hu CY, Guo CC, et al. Intercalation of ramie short fiber between carbon fiber/epoxy matrix composite. Journal of Composite Materials 2017; 34(06): 1237–1244.

[19] Wang YJ, Meng JG, Zhang YF, et al. Performance Test of Aramid Modified by Silane Coupling Agent. Synthetic fiber 2017; 46(04): 43–46.

[20] Ma W. Preparation and properties of thermoplastic natural bamboo fiber composite. Hangzhou: Zhejiang Agriculture and Forestry University, 2012. 47–68.

[21] Li X, Panigrahi S, Tabil LG. A study on flax fiber reinforced polyethylene biocomposites. Applied Engineering in Agriculture 2009; 25(4): 525–531.

[22] Ku H, Wang H, Pattarachaiyakoop N, et al. A review on the tensile properties of natural fiber reinforced polymer composites. Composites: Part B 2011; 42: 856–873.

[23] Wang YQ, Afsar AM, Song JI. Optimization of brazing conditions for OFHC Cu and ASTM A501 low carbon steel by Taguchi method. International Journal of Precision Engineering and Manufacturing 2009; 10: 97–104.

[24] Wang YQ, Byun JH, Kim BS, et al. The use of Taguchi optimization in determining optimum electrophoretic conditions for the deposition of carbon nanofiber on carbon fibers for use in carbon/epoxy composite. Carbon 2012; 50: 2853–2859.

[25] Taguchi G. Introduction to quality engineering. New York: McGraw-Hill; 1990.

[26] Roberts MJ, Russo R. A student's guide to analysis of variance. London: Routledge, 2009. 92–109.

[27] Montgomery DC. Design and analysis of experiments (5th ed.). New York: John Wiley Sons, 2001. 65–72.

Viser Technology Pte. Ltd.
Mechanical Engineering Science
https://doi.org/10.33142/me.v1i1.661

Research Article Open Access

Cement Pavement Surface Crack Detection Based on Image Processing

Hongwei Lei [a], Jianlian Cheng [b,*], Qi Xu [c]

Highway Maintenance Equipment National Engineering Laboratory, Key Laboratory of Road Construction Technology and Equipment Ministry of Education, School of Construction Machinery,Chang'an University,Xi'an 710064,China

****Corresponding Author:*** *Jianlian Cheng, cjlian@chd.edu.cn*

Abstract:
This article introduces the application of image recognition technology in cement pavement crack detection and put forward to method for determining threshold about grayscale stretching. This algorithm is designed for binarization which has a self-adaptive characteristic. After the image is preprocessed, we apply 2D wavelet and Laplace operator to process the image. According to the characteristic of pixel of gray image, an algorithm designed on binarization for Binary image. The feasibility of this method can be verified the image processed by comparing with the results of three algorithms: Otsu method, iteration method and fixed threshold method.

Keywords: *Pavement crack detection; Grayscale stretching; Self-adaptive; 2D Wavelet; Laplace; Binarization*

Citation: H.W. Lei, J.L. Cheng, Q. Xu, Cement Pavement Surface Crack Detection Based on Image Processing. *Mech Eng Sci*, 2019,1(1): 48-53. https://doi.org/10.33142/me.v1i1.661

1. Introduction

Pavement Surface Crack is one of the main damage forms of road. Manual crack detection is time-consuming, laborious and costly. This method is no longer suitable for the market. Road surface image capture and processing techniques are now widely used. However, due to various reasons of interference, the captured image is not easy to identify [1].

In order to solve the problems we encountered, many scholars have done the corresponding research. Fan Jiu-lun [2] proposed the two-dimensional otsu's curve thresholding segmentation method for gray-level images; Lakhwinder Kaur [3] proposed image de-noising NormalShrink threshold method, but it can lead to blurry edges on the target. DONG Hong-Yan [4] proposed the multiscale edge detection based on laplacian pyramid method, this approach enhances the boundary between the target and background; Nobuyuki Otsu [5-9] proposed the Otsu method for binary image conversion, however, when it is applied to pavement crack image processing, the results are not ideal.

In this article, we begin with gray scale transformation, and then we use weighted average method to transform the captured image. Using the improved grayscale stretching algorithm to stretch the gray image. After that, we use Laplace operator to sharpen the abrupt region of the image pixel value. Next step is image de-noising which use 2D wavelet de-noising method. Finally, an algorithm about binarization that have a self-adaptive characteristic is used to transform the image. The transformed image is compared with the processing results of Otsu method, iteration method and fixed threshold method.

The results show that the grayscale stretching algorithm and line self-adaptive threshold binarization algorithm in this paper presented are effective in image processing.

2. Image preprocessing

Images which are captured at high speed usually have three disturbing factors: uneven illumination, random noise and the occlusion of irregular objects. Cement pavement cracks are mainly divided into three types: transverse, longitudinal and irregular oblique cracks. Usually, the color of the crack is dark, that is, the gray-level of the target is low. To sum up, in image processing, it is necessary to enhance the target surface crack and reduce the interference from the background [10].

2.1 Gray-level transformation

There are three methods that maximum method, average method and weighted average method for image to transformation its gray-level [11]. The maximum method is to select the maximum value from the R, G and B values of the image as the R, G and B values of the new image. That is, as the following formula (1) is shown.

$$R = G = B = \max(R, G, B) \tag{1}$$

The gray image obtained by this method is not suitable for pavement crack image processing because of its high brightness. The average method converts the R, G and B values of the image into the average values of the original R, G and B values, as formula (2) shown below:

$$R = G = B = (\frac{R+G+B}{3}) \tag{2}$$

The gray image generated by this method is softer than those obtained by other methods, while the processing of cracked image requires enhancing the edge of mutant pixel, so this method is not applicable, too.

The weighted average method is to carry out the weighted average of the values of R, G and B according to a certain weight value, as formula (3) shown below.

$$R = G = B = \frac{(\omega_R R + \omega_G G + \omega_B B)}{3} \tag{3}$$

ω_R、ω_G、ω_B are the weights of R, G and B, and different values are taken to form different grayscale images. According to experience, taking $\omega_G > \omega_R > \omega_B$ could make the obtained images easier to recognize. In general, we take $\omega_R = 0.2989$, $\omega_B = 0.5870$, $\omega_G = 0.1140$, that could obtain better grayscale images at this time, as shown in figure1.

2.2 Grayscale stretching method

2.2.1 Algorithm

Image quality is often affected by many reasons, which hinders the detection of cracks. Grayscale stretching is a common method to improve image quality.

The histogram of cement pavement crack image is mainly of single-peak type, and the crack of pavement is in the dark part with lower gray-level. The background focuses near the peak. Grayscale stretching is completed through grayscale transformation [12].

Let $l(n,m)$ be the input image, its minimum gray-level J and maximum gray-level K are defined as follows:

$J = \min[l(n,m)]$;

$K = \max[l(n,m)]$

Map J and K linearly to 0 and 255, respectively, and the resulting image $q(n,m)$ is as follows:

$$q(n,m) = (\frac{255}{J-K})[l(n,m) - J] \tag{4}$$

According to the characteristics of road surface image, using stretching method to improve the above formula. The main way of segmental stretching is to divide the gray histogram of pavement crack image into multiple sections, and then conduct linear processing to enhance the recognition degree of the image without losing the original information of the image. The piecewise linear transformation can highlight the grayscale details of the target and suppress the background of the image according to the actual needs [13]. The formula (5) is as follows:

$$q(n,m) = \begin{cases} \frac{m_1}{n_1} l(n,m), & l(n,m) < n_1 \\ \frac{m_2 - m_1}{n_2 - n_1}[l(n,m) - n_2] + m_1, & n_1 < l(n,m) < n_2 \\ \frac{255 - m_2}{255 - n_2}[l(n,m) - n_2] + m_2, & n_2 < l(n,m) < 255 \end{cases} \tag{5}$$

The grayscale range of the image is $[0,255]$. According to the requirements, the range n of the piecewise function and the slope m of each function are selected, so we divide the gray level of the image into $[0,n_1]$, $[n_1,n_2]$ and $[n_2,255]$, and the second section is stretched, which can effectively suppress the background area and enhance the crack pixel of the road image. However, the numerical selection of n_1 and n_2 is a difficult work. According to the characteristics of pixel distribution of different images, different segmentation points can be selected. If the selected segmentation point is not reasonable, it may cause image distortion or enhance the image noise.

2.2.2 Piecewise function method

According to the characteristics of cement pavement images, designing the algorithm to determine the threshold values n_1 and n_2, The formula (6),(7) are as follows:

$$n_1 = \frac{\sum_k x_{i_1 j_1}}{k} \quad (i_1, j_1 \in M) \tag{6}$$

$$n_2 = \frac{\sum_k x_{i_2 j_2}}{k} \quad (i_2, j_2 \in M) \tag{7}$$

n_1 in the piecewise function is the expected value of the last 30% in the order from the largest to the smallest of the grayscale pixel values. n_2 in the piecewise function is the expected value of the first 30% in the order from large to small of the grayscale pixel values. K is 30% of the total number of pixels. That is, $x_{i_1 j_1}$ and $x_{i_2 j_2}$ are the pixel value.

Grayscale stretching was performed on the crack image, and the results were shown in figure 1. (a), (b) and (c) refer to the original, grayscale and grayscale stretching results.

(a)

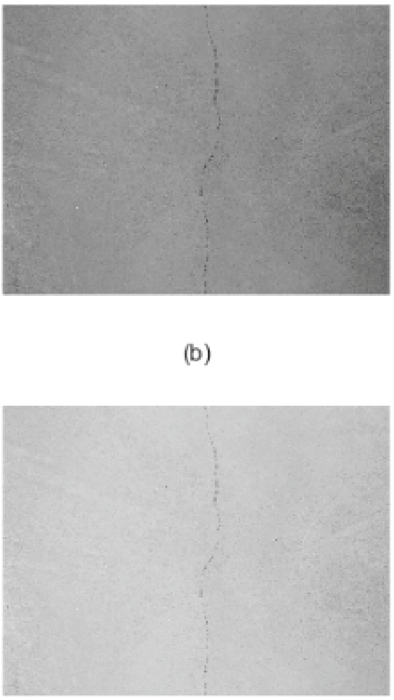

(b)

(c)

Figure 1. Image processing results comparison

3. De-noising method based on 2D wavelet

Road surface images contain noise, which will cause interference to image grayscale stretching, sharpening and segmentation in the later stage. Due to the variable nature of its window, wavelet transform can maintain the image detail information at the same time of de-noising, that is, narrow window is used when the signal is high frequency, and wide window is used when the signal is low frequency [14].

Denotes the mother wavelet is $\psi(t)$, the scaling factor is a, and the translation factor is b, then the wavelet generated by the mother wavelet is :

$$\psi_{a,b}(t)=\frac{1}{\sqrt{|a|}}\psi(\frac{t-b}{a}) \tag{8}$$

There we have, $a,b\in R, a\neq 0$.

For the mother wavelet $\psi(t)$, there we have:

$$C_{\psi}=\int_{-\infty}^{+\infty}\frac{|\hat{\psi}(\omega)|^2}{|\omega|}\mathrm{d}\omega<\infty \tag{9}$$

The continuous wavelet transform of signal $f(t)$ is

$$w_f(a,b)=\left\langle f,\psi_{(a,b)}\right\rangle=|a|^{-\frac{1}{2}}\int_{-\infty}^{+\infty}f(t)\overline{\psi(\frac{t-b}{a})}\mathrm{d}t \tag{10}$$

$w_f(a,b)$ corresponds to the decomposition of $f(t)$ in family of function $\psi_{a,b}(t)$. It can also be regarded as the filtering operation of the original signal $f(t)$ and a set of wavelet bandpass filters of different scales, so that the signal can be decomposed into a series of frequency bands for analysis and processing.

Sample a and b, take $a=a_0^m, b=nb_0a_0^m$, and obtain the discrete wavelet transform (DWT). Generally, $a_0=2, b_0=1$ are selected. In this case, DWT is called multi-resolution analysis.

Mallat puts forward the tower-type algorithm for solving wavelet coefficients [15], which enables discrete wavelet transform to appear in the form of digital QMF filter Banks. The wavelet decomposition formula of multiresolution analysis is

$$\begin{cases} c_k^{j-1}=\sum_n a_{n-2k}c_n^j \\ d_k^{j-1}=\sum_n b_{n-2k}c_n^j \end{cases} \tag{11}$$

The reconstruction formula is

$$c_k^j=\sum_n(p_{k-2n}c_n^{j-1}+q_{k-2n}d_n^{j-1}) \tag{12}$$

Each row and column pixels of the image are processed by Mallat algorithm respectively to complete a 2D wavelet transform. There we get four subgraphs representing different frequency characteristics and direction characteristics of the original image.

The wavelet transform threshold de-noising method proposed by Donoho et al. [16] is as follows:

Step1: The wavelet coefficients of signals are obtained after wavelet transform of signals.

Step2: The nonlinear threshold t acting on the wavelet coefficient, and obtain the modified coefficient value, That is:

hard threshold method

$$\hat{x}=T_k(X,t)=\begin{cases} X, |X|\geq t \\ 0, |X|<t \end{cases} \tag{13}$$

soft threshold method

$$\hat{x}=T_k(X,t)=\begin{cases} \mathrm{sgn}(X)(|X|-t), |X|\geq t \\ 0, |X|<t \end{cases} \tag{14}$$

The nonlinear soft threshold is :

$$t=\sigma\sqrt{2\log n} \tag{15}$$

Where, n is the signal length, σ is the signal standard variance, and t is the estimated threshold level.

Step3: carry out wavelet inverse transformation and reconstruct the signal.

The above 2D wavelet de-noising method is used to process the original image, and the processed results are shown in figure 2.

Figure 2. The result of 2D wavelet de-noising

4. Laplace operator transformation

The main method of image sharpening enhancement is to strengthen the part of image pixel where the value change is bigger, so as to make the contour of image clearer. In other words, when the pixel gray value of the selected center of the neighborhood is lower than the average gray value of other pixels in the field, the gray value of this center pixel will be reduced, and vice versa. In order to achieve image sharpening processing.

Laplace operator is a widely used sharpening operator in image sharpening processing [4].Laplace operator is a kind of second-order differential operator, whose input image will not affect the operator after rotating at a certain angle. For 2D image $f(x,y)$, the general equation of Laplace operator is:

$$\nabla^2 f = \frac{\partial^2 f}{\partial x^2} + \frac{\partial^2 f}{\partial y^2} \tag{16}$$

Among them:

$$\frac{\partial^2 f}{\partial x^2} = f[x+1,y] - 2f[x,y] + f[x-1,y] \tag{17}$$

$$\frac{\partial^2 f}{\partial y^2} = f[x,y+1] - 2f[x,y] + f[x,y-1] \tag{18}$$

The equation in discrete form is:

$$\begin{aligned} \partial^2 f(x,y) = {} & f(x+1,y) + f(x-1,y) + \\ & f(x,y+1) + f(x,y-1) - 4f(x,y) \end{aligned} \tag{19}$$

Laplace operator and appropriate filter template are used to sharpen the crack image after gray stretch, and the results are shown in figure 3.

Figure 3. The result of Laplace operator transformation

5. Methods in this article

The histogram of the crack image processed by the above method is unimodal. The Ostu method [17] is for obtaining the threshold value of images with bimodal gray histogram. Obviously, it has poor performance in pavement crack image processing. The iterative method retains too much noise when it is applied to pavement crack image processing. The fixed threshold method loses too much information in the work.

R. j. Wall put forward dynamic calculation of the threshold algorithm [18], that divide image into many small pieces, get thresholds from each small piece. In comparison, the performance of this algorithm is improved. Due to the cracks are line shape, after the processing image in Wall's algorithm kept too much noise, the effect is not ideal.

In view of this situation, this article designs a binarization algorithm for cement pavement crack images. The pixel of cement pavement crack image is mainly divided into two parts: background and target. The pixel value of the target part is obviously lower than that of the background part. Therefore, the common image segmentation algorithm has a large degree of distortion in the image segmentation of cement pavement. It cause the background and the noise get enhancement or the crack target information to lose.

Most of the already proposed adaptive threshold binarization algorithm have been used to segment pixels into chunks, that is, to consider the pixel value characteristics of a local 2D neighborhood, which leads to inadequate selection of threshold and unsatisfactory processing effect in crack image processing.

According to the characteristics of cement pavement image, designing the adaptive threshold binarization algorithm as follows. The processing image size is 1024×768.

The operation process of this algorithm is shown in figure 4.

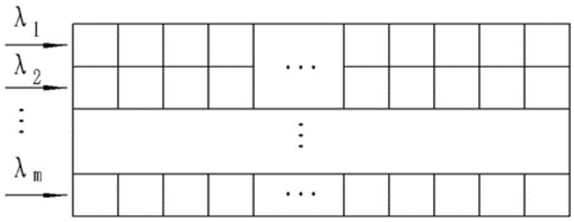

Figure 4. The process of running the line threshold algorithm

Identify the grayscale image as $f(x,y)$, Where, $x \in (1,2,\cdots,m)$ and $y \in (1,2,\cdots,n)$ are the matrix whose pixel of gray image is m rows and n columns, and the element is a_{xy}. Each a_{xy} value pair should have a pixel gray value of $a_{xy} \in (0,255)$. Arrange each row pixel according to its gray value from small to large, then take the first s, where $s = \left[\frac{n}{10 \times t}\right], t \in R$.

After many experiments, when the pavement crack image select $t = 0.98$ processing effect is good. Then the threshold of line x is $\lambda_x = \frac{a_{x1} + a_{x2} + a_{x3} + \cdots + a_{xs}}{s}$, and the pixel whose gray value is bigger than λ_x,then set it equal to 255; If pixels with a grayscale value less than λ_x, let set it equal to 0.

Traverse all the pixels of the image, that is, complete the binarization transformation of the gray image.

6. Conclusions

The pavement crack images processed by gray stretch, Laplace sharp and 2D wavelet threshold de-noising were converted into binary-valued images respectively by Ostu method, iterative method and fixed threshold method and the method desighed in this article. The results are shown in figure 5, where (a), (b), (c) and (d) are the processing results of Ostu method, iteration method, fixed value method and line threshold algorithm.

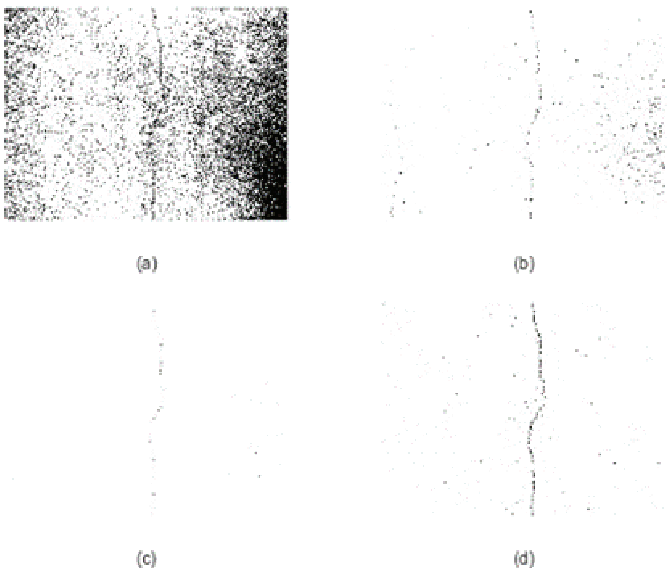

Figure 5. Comparison of binarization results

In figure 6, figure 7, figure 8 and figure 9 are project charts of processing results of Ostu method, iteration method, fixed value method and line threshold algorithm. It can be seen that the noise in the image vertical projection processed by Ostu method seriously affects the recognition of crack location; The image processed by iterative method is lost information and the image has large noise interference. After the fixed threshold method, the target crack information is lost seriously. Line threshold algorithm, the threshold binarization algorithm proposed in this paper, lost fewer information after processing.

Computer technology improves the efficiency of maintaining the pavement. It saves labor cost and time cost. Compared with other binarization methods, the method proposed in this paper is more effective in image processing of pavement cracks. It loses less information and the resulting image is more recognizable.

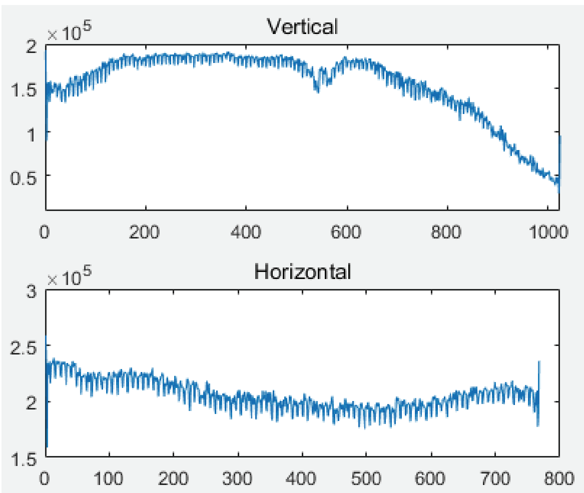

Figure 6. The projection of Ostu method processing results

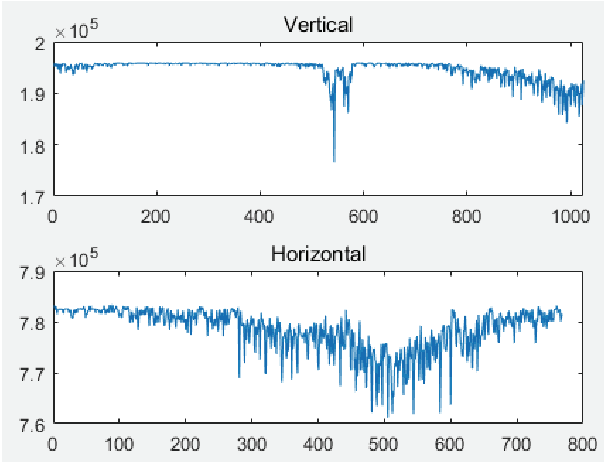

Figure 7. The projection of iteration method processing

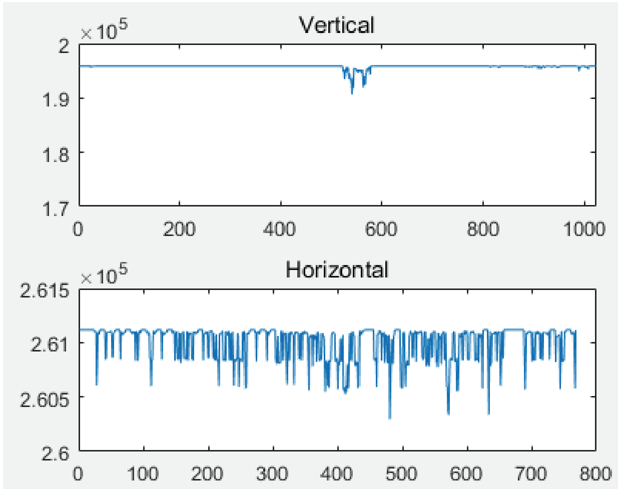

Figure 8. The projection of fixed value method processing result

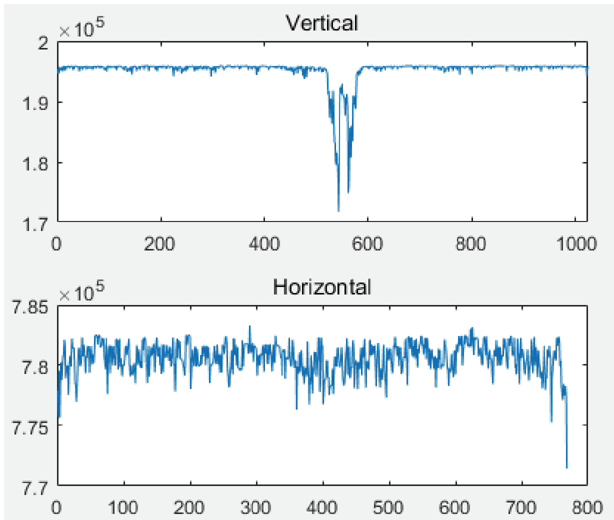

Figure 9. The projection of line threshold method processing result

References

[1] CHUO Er-yong, Development Summary of International Pavement Surface Distress Automatic Survey System [J]. Transport Standardization, 2009, 09: 96-97;

[2] FAN Jiu-lun, ZHAO Feng, Two-Dimensional Otsu's Curve

Thresholding Segmentation Method for Gray-Level Images [J], Acta Electronica Sinica,2007,35(4):751-755;

[3] Lakhwinder KAUR，Savita GUPTA，R.C. CHAUHAN. Image Denoising using Wavelet Thresholding [A]. Proceedings of the Third Indian Conference on Computer Vision, Graphics & Image Processing [C]. Ahmadabad, India: Allied Publishers Private Limited, 2002, 11:1522-1531;

[4] DONG Hong-yan, WANG Lei, LI Ji-cheng, SHEN Zhen-kang, Multiscale edge detection based on Laplacian pyramid [J], Opto-Electronic Engineering,2007,7(34):135-140;

[5] Ohtsu N.A threshold selection method from gray-level histograms [J].IEEE Transactions on Systems Man & Cybernetics，2007，9（1）：62-66.

[6] Ferman A M，Tekalp A M，Mehrotra R.Robust color histogram descriptors for video segment retrieval and identification [J].IEEE Transactions on Image Processing;A Publication of the IEEE Signal Processing Society, 2002，11(5)：497-508;

[7] Zhang C，Xie Y，Liu D，et al.Fast threshold image segmentation based on 2D fuzzy fisher and random local optimized QPSO [J].IEEE Transactions on Image Processing, 2017, 26(3): 1355-1362;

[8] Qi Lin，Wang Jing，Chen Yanlei，et al. Research on the image segmentation of icing line based on NSCT and 2-D OSTU[C], International Conference on Modelling, Identification and Control, 2015: 1-5;

[9] Liu S.Image segmentation technology of the Ostu method for image materials based on binary PSO algorithm[M], Advances in computer science, intelligent system and environment. Berlin Heidelberg: Springer, 2011：415-419;

[10] PENG Bo1, JIANG Yang-sheng, HAN Shi-fan1, LUO Nanxin, A Review of Automatic Pavement Crack Image Recognition Algorithms[J], Journal of Highway and Transportation Research and Development, 2014, 7, 7(31): 10-25;

[11] Gu Mehua, Su Binbin, Wang Miaomiao, Wang Zhilei, Survey on decolorization methods[J], Application Research of Computers, 2018, 36(5):

[12] Hideyuki Tamura , Computer image processing technology [M]。Beijing Normal University Publishing House,1986；

[13] Rafael C. Gonzalez, Richard E. Woods，Digital image processing [M], Publishing House of Electronics Industry,2017;

[14] 马拉特，A wavelet tour of signal processing[M].China Machine Press，2003

[15] Angel P，Morris C，Analyzing the Mallat wavelet transform to delineate contour and textural features[J]．Computer Vision and Image Understanding，2000，80 (3) : 267-288;

[16] D.L.Donoho, I.M.JohnStone.Ideal spatial adaptation via wavelet shrinkage[J]. Biometrika, 1994, 81: 425-455;

[17] Otsu N.A threshold selection method from gray-level histo-grams[J].IEEE Transactions on Systems,Man and Cyber-netics,1979,9(1):62-66

[18] Castleman, K. Digital Image Processing. Prentice-Hall Signal Pro-cessing Series, 1979.

Viser Technology Pte. Ltd.
Mechanical Engineering Science
https://doi.org/10.33142/me.v1i1.662

Research Article Open Access

Strength Evaluation of a Bogie Frame by Different Methods

Daoyun Chen[1,*], Shouguang Sun[2], Qiang Li[2]

[1] Key Laboratory of Conveyance and Equipment (Ministry of Education), East China Jiaotong University, Nanchang 330013, China
[2] School of Mechanical,Electronic and Control Engineering, Beijing Jiaotong University, Beijing 100044, China

***Corresponding Author:** *Daoyun Chen, E-mail address:13116326@bjtu.edu.cn*

Abstract:
Some crucial loads that current strength design specifications have not taken into ac-count are also considered when assessing the strength of a bogie frame. Calculation methods of these loads come from load analysis. Finite element simulation and fa-tigue test rig have been used to assess static strength and fatigue strength of a bogie frame. In addition to the two methods, actual running test is also used to assess bogie frame fatigue strength. In finite element simulation method, endurance limit and modified Goodman fatigue limit diagram are two important tools to judge whether fatigue strength of a bogie frame meets requirement. In actual running test method, Miner linear cumulative damage rule is used to assess bogie frame fatigue strength. Endurance limit and modified Goodman fatigue limit diagram are two effective tools to judge fatigue strength of the frame. For the measured dynamic stress data, Miner linear cumulative damage rule seems to be very effective when judging fatigue strength of the frame. All the above methods have proved that static and fatigue strength of the tested bogie frame meets requirement.

Keywords: *Strength; Bogie frame; Finite elements; Fatigue test rig; Actual running test*

Citation: D.Y. Chen, S.G. Sun, Q. Li, Strength Evaluation of a Bogie Frame by Different Methods. *Mech Eng Sci*, 2019,1(1): 54-64. https://doi.org/10.33142/me.v1i1.662

1. Introduction

Bogie frame, one of the most important high-speed train load-bearing components，is located between wheelsets and train carriage. Bogie frame belongs to typical frame type structure and it has very complex loading conditions. To some extent, whether structural strength meets requirements of relevant regulations directly determines safety of high-speed train. Therefore, it is very necessary to assess bogie frame strength. There are a variety of structural strength evaluation standards of bogie frame in the world today such as EN 13749 [1], UIC 615-4 [2] and JIS E 4207 [3]. These standards have made clear experimental rules of bogie frame's static strength and fatigue strength. According to these standards, loads applying on a bogie frame mainly consist of vertical load and transverse load. Calculation methods of these loads are also listed by formulas. By using of these standards to assess bogie frame strength can get satisfactory results [4-7]. However, loading condition of bogie frame is extremely complex. Only using two kinds of load and neglecting the other loads to analyze bogie frame strength will get risk assessment results.

In order to accurately reflect loading condition of bogie frame and assess bogie frame strength, this paper calculates vertical loads, transverse loads, longitudinal loads, motor inertia loads, gearbox hanger loads, brake friction loads and anti-side-rolling torsion pole loads to evaluate bogie frame strength.

In this paper, strength evaluation of bogie frame mainly consists of static strength evaluation and fatigue strength evaluation. Static strength evaluation is operated by means of finite element simulation and load testing on test rig. Fatigue strength evaluation is operated by means of finite element simulation, load testing on test rig and train running test on actual railway.

2. Load calculation method

The studied bogie frame mainly consists of two side beams and two transverse beams. Various kinds of component mounting base are installed on the frame so that loads are very complicated. Four ends of the frame connect with axle box springs and four locating bases connect with axle box rotary arms.

Loading condition of the bogie frame is shown in Figure 1. Vertical loads and transverse loads can be calculated from formulas in EN13749. Calculation methods of the other types of load are deduced from load analysis.

2.1. Vertical loads

Vertical loads are applied to each side frame. According to EN13749, the load that each side frame withstand is calculated as (1):

$$F_{z1max}=F_{z2max}=\frac{1.4g}{2n_b}(M_v+C_1\text{-}2m^+) \tag{1}$$

Nomenclature

F_{z1},F_{z2}	Vertical loads acting on each side frame	F_{zbrake}	Vertical load caused by braking load
C_1	The mass of the passengers under overload condition	a_{bmax}	Maximum braking deceleration
M_v	Net mass of the train body	R	Radius of wheel
n_b	Number of each carriage bogie	R_f	Friction radius of brake disk
m^+	Mass of the bogie	K	Stiffness of air spring
n_e	Number of each bogie axle	F_{anti}	Anti-side-rolling torsion pole load
F_y	Transverse load acting on bogie frame	C	Damp of second vertical shock absorber
F_x	Longitudinal load acting on bogie frame	L_{anti}	Transverse pitch between two anti-side-rolling torsion pole seats
a_x	Longitudinal impact acceleration of bogie	á	Side-rolling angle of train carriage body
a_{ver}	Vertical vibration acceleration of motor	â	Torsion angle of torsion pole
a_{tra}	Transverse vibration acceleration of motor	L	Arm length of torsion bar
a_{lon}	Longitudinal vibration acceleration of motor	T_r	Torsional rigidity of torsion pole
I_{ver}	Vertical load of motor caused by inertia	ó$_1$	Major principal stress
I_{tra}	Transverse load of motor caused by inertia	ó$_2$	Secondary principal stress
I_{lon}	Longitudinal load of motor caused by inertia	ó$_3$	Third principal stress
M_m	Mass of motor	ó$_{von}$	Vonmises stress
F_{gz}	Gear box hanger load caused by short circuit torque of motor	K_n	Normalized constant
L_{tan}	Orthogonal distance between hanger rod center line and axle center line	ö	Variable to adjust the proportion of each distribution function in the combined distribution
F_1	Reactive load applying on driving gear shaft	$f(x)_1$	Probability density function of Weibull distribution
T_{mmax}	Short circuit torque of motor	$f(x)_2$	Probability density function of lognormal distribution
R_1	Radius of driving gear	f(x)	Probability density function of combined distribution
R_2	Radius of driven gear	n_i	Cycle numbers of each level
i	Transmission ratio	C_3, m	S-N curve parameters
F_{gzmax}	Maximum gear box hanger load	ó$_{-1i}$	Stress amplitude of each level
M_g	Mass of gearbox	D	Miner damage
F_x'	Reactive load of F_x	N_i	Fatigue life under certain stress level

2.2. Transverse loads

According to EN13749, transverse loads are calculated as (2):

$$F_{ymax}=2[10^4+\frac{(M_v+C_1)g}{3n_en_b}] \tag{2}$$

Transverse loads are distributed on lateral stop and air spring seat.

2.3. Longitudinal loads

Longitudinal loads are calculated according to Newton's Second Law of Motion. The formula is listed as (3):

$$F_{xmax}=m^+a_{xmax} \tag{3}$$

The acting positions of longitudinal loads are two traction rod seats.

2.4. Motor inertia loads

Considering the influence of vibration acceleration, motor inertia loads are listed as follows:

$$I_{ver}=M_ma_{ver} \tag{4}$$

$$I_{tra}=M_ma_{tra} \tag{5}$$

$$I_{lon}=M_ma_{lon} \tag{6}$$

2.5. Gearbox hanger loads

Gearbox hanger loads are caused by two main aspects. One of the aspects is the load that caused by short circuit torque of motor. This torque is also called starting torque. When power is connected to motor and motor has yet to start turning, wires between stator and rotor are equivalent to short circuit. The torque is very large at this moment which can be up to 2.2 times bigger than rated load torque of motor.

Load diagram under the condition of motor short circuit is shown in Figure 2.

As can be seen from Figure 2, the gearbox hanger is connected to case body. Driving gear is connected to motor and driven gear is connected to hollow axle of high-speed train. When motor runs, driven gear is driven to rotate by driving gear. As a result, motor torque is passed to driven gear. According to principle of mechanics, all the torques are converted to loads applying on driving gear shaft, hollow axle of high-speed train and gearbox hanger. According to force moment equilibrium principle at central point of driven gear, force moment equilibrium equation can be listed as follows:

$$F_{gz}L_{tan}=(R_1+R_2)F_1=(R_1+R_2)\frac{T_{mmax}}{R_1} \tag{7}$$

Therefore,

$$F_{gz}=\frac{T_{mmax}(R_1+R_2)}{R_1L_{tan}}=\frac{(1+i)T_{mmax}}{L_{tan}} \tag{8}$$

Considering vibration load of gearbox, maximum load applying on gearbox hanger is

$$F_{gzmax}=\frac{(1+i)T_{mmax}}{L_{tan}}+\frac{M_g a_{ver}}{3} \tag{9}$$

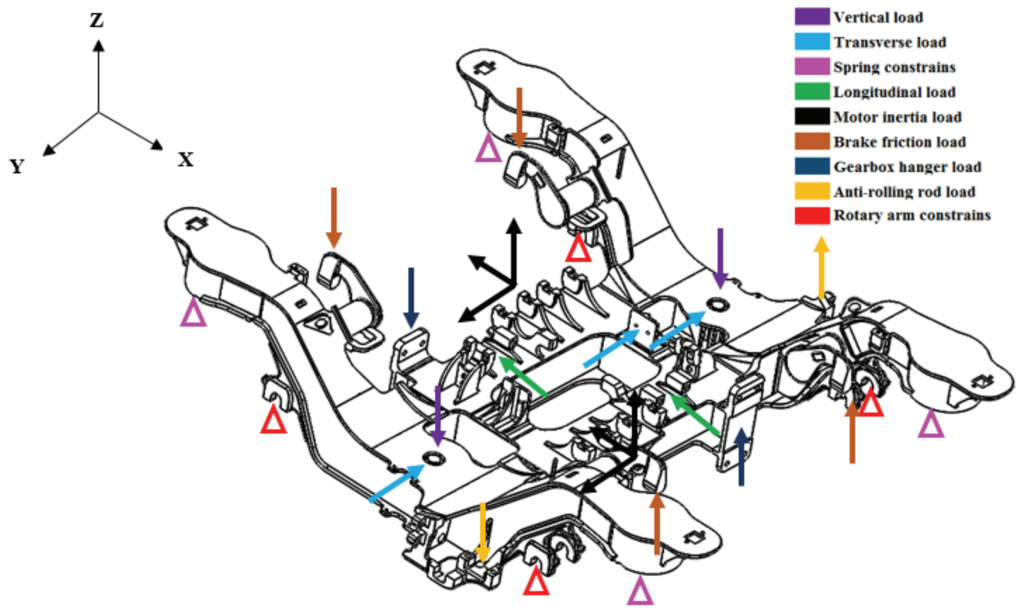

Figure 1. Bogie frame load diagram

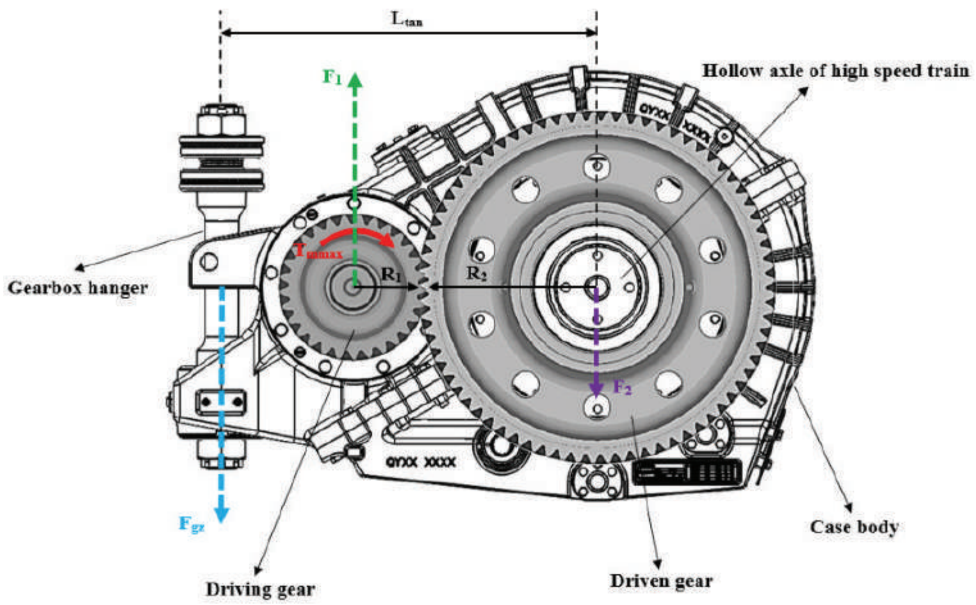

Figure 2. Load diagram of gearbox

2.6. Brake friction loads

The brake mode of bogie in this paper is wheel disc brake. When brake calipers act on brake discs, wheel loads can be considered as dynamic balance. The load diagram is shown as Figure 3.

According to EN13749, the longitudinal loads of bogie frame can be calculated as (10):

$$F_x = a_{bmax}\frac{M_v + C_1}{n_b} \tag{10}$$

According to moment balance principle, friction load of each axle that caused by maximum braking load under emergency braking condition is

$$F_{zbrake} = \frac{F_x\, R}{4R_f} \tag{11}$$

2.7. Anti-side-rolling torsion pole loads

The load diagram of anti-side-rolling torsion pole is shown as Figure 4.

On the basis of load balance, anti-side-rolling torsion pole load can be calculated as (12):

$$F_{anti} = \frac{T_r\, \beta}{L_{anti}\cos\beta} \tag{12}$$

The geometrical relationship between side-rolling angle of train carriage body and torsion angle of torsion pole is

$$\frac{L_{anti}}{2}\sin\alpha \approx L\sin\beta \tag{13}$$

3. Static strength evaluation of bogie frame

The purpose of static strength assessment is to test the stresses of bogie frame under static exceptional loads so that whether static strength can meet requirements will be judged. If stresses are lower than yield stress of the frame, then the frame can be considered to meet requirements of static strength. In this paper, two methods, that is finite element simulation and load testing on test rig, are used to evaluate static strength of bogie frame.

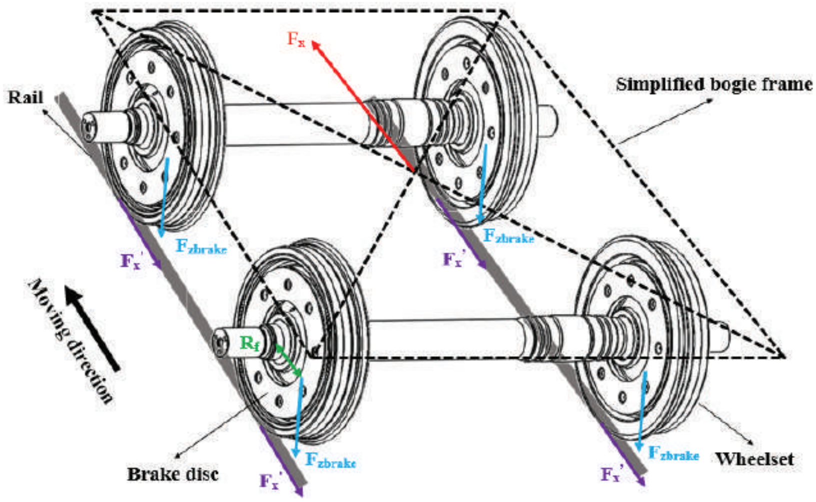

Figure 3. Load diagram of wheelset

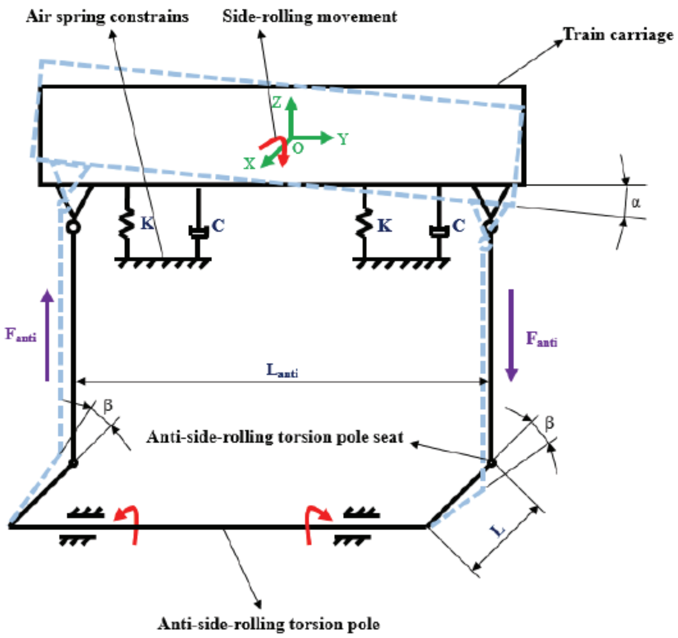

Figure 4. Load diagram of anti-side-rolling torsion pole

Therefore, anti-side-rolling torsion pole load can be modified as

$$F_{anti}=\frac{T_r \arcsin\frac{L_{anti}\sin\alpha}{2L}}{L_{anti}\sqrt{1-(\frac{L_{anti}\sin\alpha}{2L})^2}} \tag{14}$$

3.1. Checking static strength of bogie frame by means of finite element simulation

Considering bogie parameters under exceptional conditions and formulas of each load, final load cases are listed in Table 1.

Through finite element calculation, there are five positions show maximum stress on the frame under 13 kinds of load case. The vonmises stress response of the results are shown in Figure 5.

Table 2 shows frame material mechanics property parameters. After comparison of Figure 5 and Table 2, it can be seen clearly that all the stress values of the selected measuring points are lower than yield limit of base metal. Therefore, the bogie frame has enough static strength. Figure 6 displays finite element calculation results under the eighth load case which is the worst load conditions in the total 13 load cases.

As can be seen from Figure 6, the maximum stress occurs in gearbox reinforcing plate. The value of its vonmises stress is 319.6 MPa.

Table 1: Supernormal load values under different load cases.

Load type	Location		Load case 1	2	3	4	5	6	7	8	9	10	11	12	13
Vertical load	Left side beam		-183.5	-183.5	-183.5	-183.5	-183.5	-183.5	-183.5	-183.5	-183.5	-183.5	-183.5	-183.5	-183.5
	Right side beam		-183.5	-183.5	-183.5	-183.5	-183.5	-183.5	-183.5	-183.5	-183.5	-183.5	-183.5	-183.5	-183.5
Transverse load	Air spring seat		0	0	0	-14.6	14.6	0	0	0	0	0	0	0	0
	Lateral stop		0	0	0	-120.9	120.9	0	0	0	0	0	0	0	0
Longitudinal load	Front		0	126.4	-126.4	0	0	66.7	-66.7	23.4	-23.4	32.2	-32.2	0	0
	Back		0	126.4	-126.4	0	0	23.4	-23.4	66.7	-66.7	32.2	-32.2	0	0
Anti-rolling rod	Left		0	0	0	60	-60	0	0	0	0	0	0	0	0
	Right		0	0	0	-60	60	0	0	0	0	0	0	0	0
Brake friction	Front		0	0	0	0	0	0	0	0	0	48.6	-48.6	0	0
	Back		0	0	0	0	0	0	0	0	0	-48.6	48.6	0	0
Gearbox hanger	Front		0	0	0	0	0	156.1	-156.1	47.8	-47.8	0	0	0	0
	Back		0	0	0	0	0	-47.8	47.8	-156.1	156.1	0	0	0	0
Motor inertia	Vertical	Front	0	0	0	0	0	0	0	0	0	0	0	-85.7	-85.7
		Back	0	0	0	0	0	0	0	0	0	0	0	-85.7	-85.7
	Lateral	Front	0	0	0	0	0	0	0	0	0	0	0	39	-39
		Back	0	0	0	0	0	0	0	0	0	0	0	39	-39
	Longitudinal	Front	0	0	0	0	0	0	0	0	0	0	0	23.4	-23.4
		Back	0	0	0	0	0	0	0	0	0	0	0	23.4	-23.4

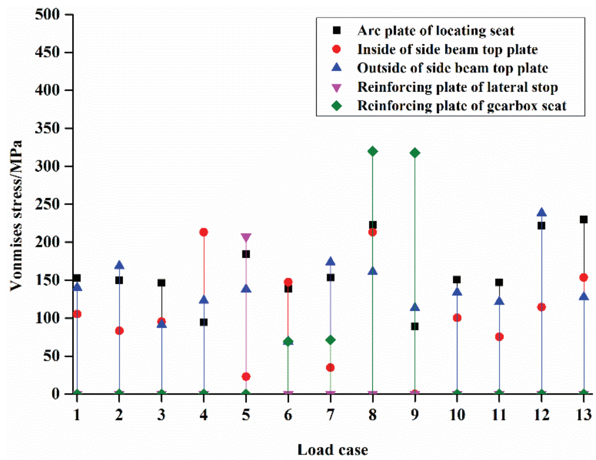

Figure 5. Response of five locations of maximum vonmises stress under different supernormal load cases.

Table 2: Material mechanics property parameter

Frame material	S355J2G
Tensile strength (MPa)	510
Yield strength (MPa)	355
Endurance limit of S-N curve by 10^7 cycles (MPa)	130
Elastic modulus(MPa)	206000
Poisson's ratio	0.29

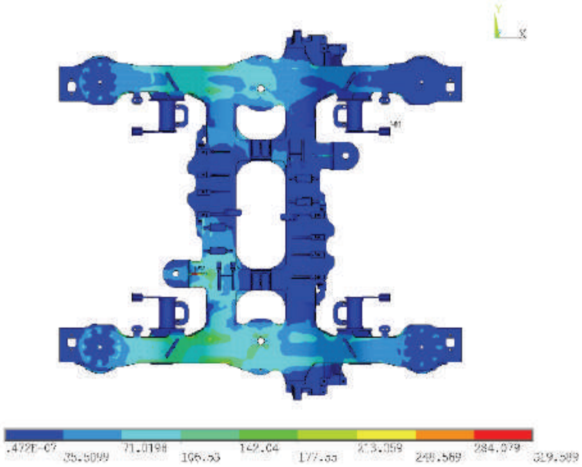

(a) The complete figure

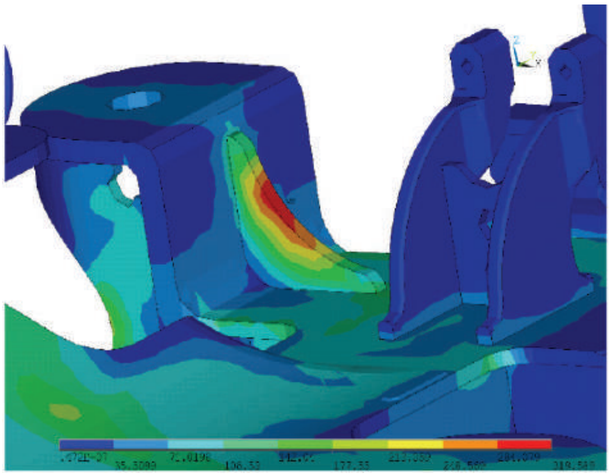

(b) The local figure of the reinforcing plate

Figure 6. Finite element results of the worst load cases.

Table 3: Von Mises stress results comparison between FE and test(MPa).

Location	Meth-od	Load case												
		1	2	3	4	5	6	7	8	9	10	11	12	13
Arc plate of locating seat	FE	152.5	150.2	146.3	94.7	184.2	138.4	153.3	223.1	89.2	150.5	147.2	221.6	230.2
	Test	154.5	154.2	150.3	87.7	180.2	130.4	152.3	221.1	95.2	156.5	147.2	228.6	235.2
Inside of side beam top plate	FE	105.3	83.2	95.4	213.1	23.1	147.2	34.7	213.1	0	100.3	75.3	114.3	153.5
	Test	93.3	80.2	87.4	207.1	23.1	144.2	32.7	206.1	10	100.3	75.3	113.3	151.5
Outside of side beam top plate	FE	140.2	168.9	91.4	123.3	138.1	69.2	173.7	161.2	113.6	133.8	121.6	238.5	127.9
	Test	149.2	178.9	94.4	126.3	145.1	65.2	171.7	156.2	120.6	129.8	118.6	234.5	118.9
Reinforcing plate of lateral stop	FE	0	0	0	0	207.2	0	0	0	0	0	0	0	0
	Test	0	0	0	0	201.4	0	0	0	0	0	0	0	0
Reinforcing plate of gearbox seat	FE	0	0	0	0	0	69.2	71.4	319.6	317.7	0	0	0	0
	Test	0	0	0	0	0	67.2	71.4	308.6	310.7	0	0	0	0

3.2 Checking static strength of bogie frame by means of load testing on test rig

The full-size bogie frame was installed on MTS fatigue test rig. The biggest test load of actuator is 1000kN. Around the test rig, there were no high-intensity magnetic field, noise and calibration which could affect the testing accuracy. The temperature was kept at about 25℃ and air relative humidity was not greater than 80%. All the loads were applied by actuators. The type and value of the applied loads were consistent with finite element calculation. The complete experiment equipment is shown in Figure 7.

After applying loads on the frame, it can be seen in real time that stress values of all measuring points were lower than yield limit of base metal. Therefore, it was confirmed that static strength meets the requirements from the angle of experiment. Table 3 shows the good consistence between FE and test under supernormal load cases.

4. Fatigue strength evaluation of bogie frame

4.1. Checking fatigue strength of bogie frame by means of finite element simulation

4.1.1 Normal service loads calculation

Operating loads of bogie frame are needed to check fatigue strength. The calculation formulas of operating loads are consistent with exceptional loads. The only difference between them is that values of the parameters in those formulas have to change according to exceptional loads or normal service loads.

The normal operating load values under different load cases are shown in Table 4 and calculation results of finite element simulation are listed in Table 5

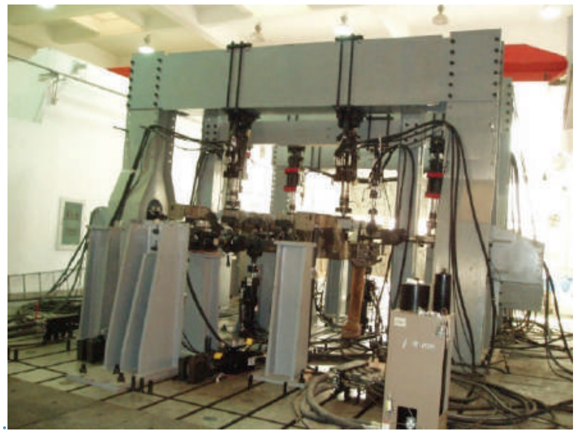

Figure 7. MTS fatigue test rig.

Table 4: Normal operating load values under different load cases.

Load type	Location		Load case 1	2	3	4	5	6	7	8	9
Vertical load	Left side beam		-124.5	-112.1	-112.1	-161.9	-161.9	-87.2	-87.2	-136.9	-136.9
	Right side beam		-124.5	-87.2	-87.2	-136.9	-136.9	-112.1	-112.1	-161.9	-161.9
Transverse load	Air spring seat		0	0	14.6	0	14.6	0	-14.6	0	-14.6
	Lateral stop		0	0	68.7	0	68.7	0	-68.7	0	-68.7
Longitudinal load	Front		0	16.7	16.7	16.7	16.7	16.7	16.7	16.7	16.7
	Back		0	16.7	16.7	16.7	16.7	16.7	16.7	16.7	16.7
Anti-rolling rod	Left		0	14.2	14.2	14.2	14.2	14.2	14.2	14.2	14.2
	Right		0	14.2	-14.2	-14.2	-14.2	-14.2	-14.2	-14.2	-14.2
Brake friction	Front		0	31.1	31.1	31.1	31.1	31.1	31.1	31.1	31.1
	Back		0	31.1	-31.1	-31.1	-31.1	-31.1	-31.1	-31.1	-31.1
Gearbox hanger	Front		0	34.2	34.2	34.2	34.2	34.2	34.2	34.2	34.2
	Back		0	34.2	-34.2	-34.2	-34.2	-34.2	-34.2	-34.2	-34.2
Motor inertia	Vertical	Front	0	-36.8	-36.8	-36.8	-36.8	-36.8	-36.8	-36.8	-36.8
		Back	0	-36.8	-36.8	-36.8	-36.8	-36.8	-36.8	-36.8	-36.8
	Lateral	Front	0	-29.4	-29.4	-29.4	-29.4	-29.4	-29.4	-29.4	-29.4
		Back	0	-29.4	-29.4	-29.4	-29.4	-29.4	-29.4	-29.4	-29.4
	Longitudinal	Front	0	-23.4	-23.4	-23.4	-23.4	-23.4	-23.4	-23.4	-23.4
		Back	0	-23.4	-23.4	-23.4	-23.4	-23.4	-23.4	-23.4	-23.4

Table 5: Finite element simulation results under normal service loads.

Location	Load case 1	2	3	4	5	6	7	8	9	Stress range	Mean stress
Traction rod seat	0	41.2	35.7	41.5	34.6	51.1	29.3	37.4	41.8	51.1	25.55
Motor suspension	0	52.3	47.7	62.2	59.6	53.4	64.1	73.3	64.2	73.3	36.65
Anti-rolling rod seat	0	37.7	66.3	82.9	63.6	71.2	85.4	89.6	97.4	97.4	48.7
Braking hanging brackets	0	64.5	66.1	82.4	105.9	77.2	88.6	92.3	101.2	105.9	52.95
Arc plate of locating seat	103.8	145.1	149.2	186.6	190.7	160.1	192.3	201.1	219.2	115.4	161.5
Inside of side beam top plate	99.6	142.6	110.7	153.3	136.5	154.3	192.4	185.2	214.3	114.7	156.9
Outside of side beam top plate	92.3	64.5	99.5	82.9	127.1	71.2	21.4	134.1	66.2	112.7	77.75
Reinforcing plate of lateral stop	0	0	116.1	0	105.9	0	113.5	0	107.5	116.1	58.1
Reinforcing plate of gearbox seat	0	75.6	66.3	69.3	84.7	71.2	85.4	44.7	73.1	85.4	42.7

4.1.2 Fatigue strength evaluation method basing on endurance limit

It is well known that when steel is applied load that changes over time, the stress will also change over time. If the value of alternating stress exceeds an ultimate strength and lasts for a long term, material will be destroyed. The ultimate strength is called endurance limit. Therefore, material will not be destroyed if the stress amplitude is lower than endurance limit. As can be seen from Table 5, all measuring points' stress amplitudes are lower than endurance limit. As a result, fatigue strength of the bogie frame meets requirement.

4.1.3 Fatigue strength evaluation method basing on modified Goodman fatigue limit diagram

Modified Goodman fatigue limit diagram [8] is a kind of simplified fatigue limit diagram. Based on linear empirical formula proposed by Goodman, actual fatigue limit stress lines are replaced by straight lines. This diagram is, in fact, a kind of fatigue damage stress envelope. If any stress points are located in the envelope, then fatigue fracture of the material will not occur after N times fatigue cycles. Based on material mechanics property parameters, the modified Goodman fatigue limit diagram is shown in Figure 8. At the same time, the stress points of finite element simulation result are also shown in Figure 8.

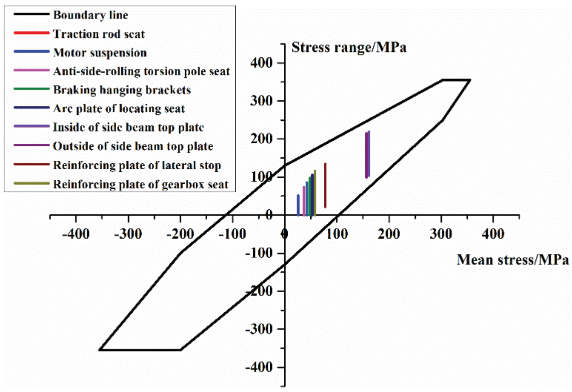

Figure 8. Goodman fatigue limit diagram

It can be seen from Figure 8 that all stress points are located in the envelope of modified Goodman fatigue limit diagram. Therefore, fatigue strength of the bogie frame meets requirement.

4.2 Checking fatigue strength of bogie frame by means of load testing on test rig

The bogie frame was also installed on MTS fatigue test rig when operating fatigue strength test. There are three different stages during test and each frame load at each stage is composed of three different forms of load, that is static load, quasi-static load and dynamic load. The cycle number of quasi-static load in the first stage is 6 million. The cycle number of quasi-static load in the last two stages is all 2m. The quasi-static load cycles are normally reversed every 10 dynamic cycles. The dynamic load frequency is 2 Hz. The load loading diagrams are shown in Figure 9 and Figure 10.

Figure 11 is operation interface of the fatigue test rig system. Through computer control, different types of load are applied on frame according to certain rules. At the same time, loading status of the frame can be monitored in real time. The fatigue test started in mid-November 2014 and ended in early April 2015. The bolts and test-ing tool were replaced several time during the whole test period. The magnetic powder inspection was operated after 2 million, 4 million, 6 million, 8 million and 10 million cycles respectively. The testing results showed that no fatigue crack was formed in the bogie frame.

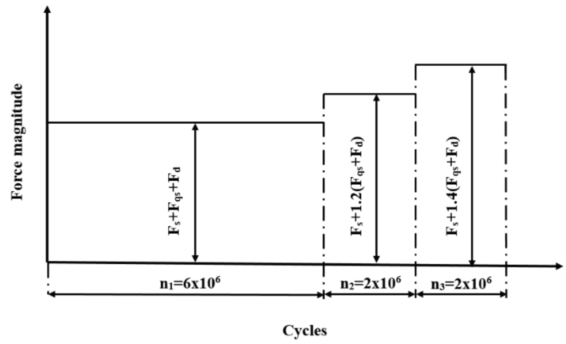

Figure 9. Variation of load magnitudes during test

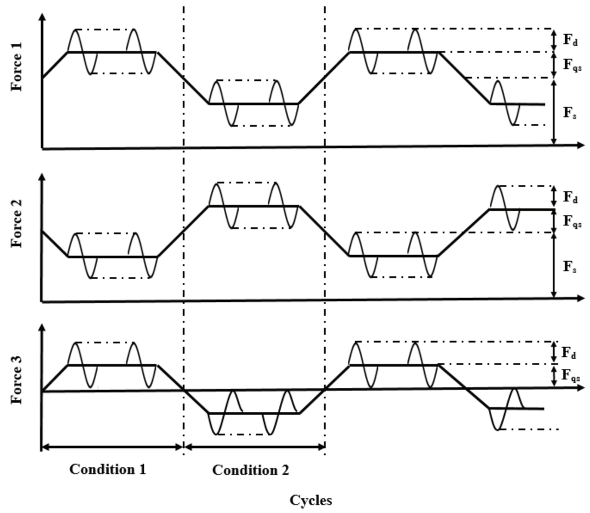

Figure 10. Variation of loads with respect to time

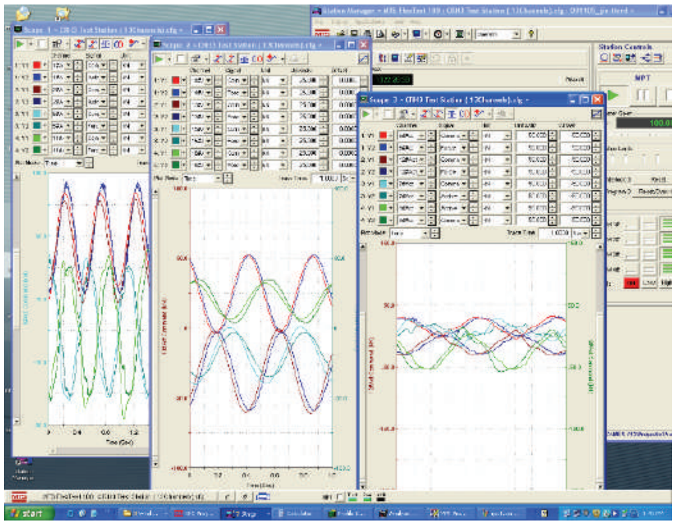

Figure 11. Computer control interface of fatigue test rig.

4.3. Checking fatigue strength of bogie frame by means of train running test on actual railway

In order to verify the frame's fatigue strength in the process of practical application, strain rosettes were pasted on fatigue critical parts of the bogie frame. Frame diagram of measuring points is shown in Figure 12. There are nine types of measuring point and twenty-eight positions of measuring point. All the strain gauges were protected by silica gel and were connected with IMC data acquisition system by wires. The IMC data acquisition system was placed in the train carriage, which is shown in Figure 13.

The tested train is a new kind of high-speed train which consists of eight train unit. The tested frame was installed in the first quarter of the head car. The installation position of the tested frame is shown in Figure 14.

The operation route is Beijing-Shanghai express railway which was opened in 2011. Total length of the railway is 1318 kilometers and the top speed of tested train is 350 km/h. The train ran a full round trip and a great deal of dynamic stress data was collected.

4.3.1 Test data processing

Although the test equipment has high accuracy and reliability, normal signal will still be difficult to avoid interference by various interference sources. Therefore, it is definitely necessary to process the signal before analysis. The signal processing process is shown in Figure 15.

4.3.2 Statistical processing of dynamic stress signal

Each strain rosette has three strain test channels. Three principal stresses of each measuring point can be gotten through certain conversion formula. Then vonmises stress can be calculated through the following formula:

$$\sigma_{von}=\sqrt{\frac{(\sigma_1-\sigma_2)^2+(\sigma_2-\sigma_3)^2+(\sigma_3-\sigma_1)^2}{2}} \tag{15}$$

There are a total of 28 measuring points' vonmises stress time domain data. These data cannot be directly used to judge fatigue strength of the frame. To make use of the measured data to check fatigue strength of the frame, rain-flow counting meth-

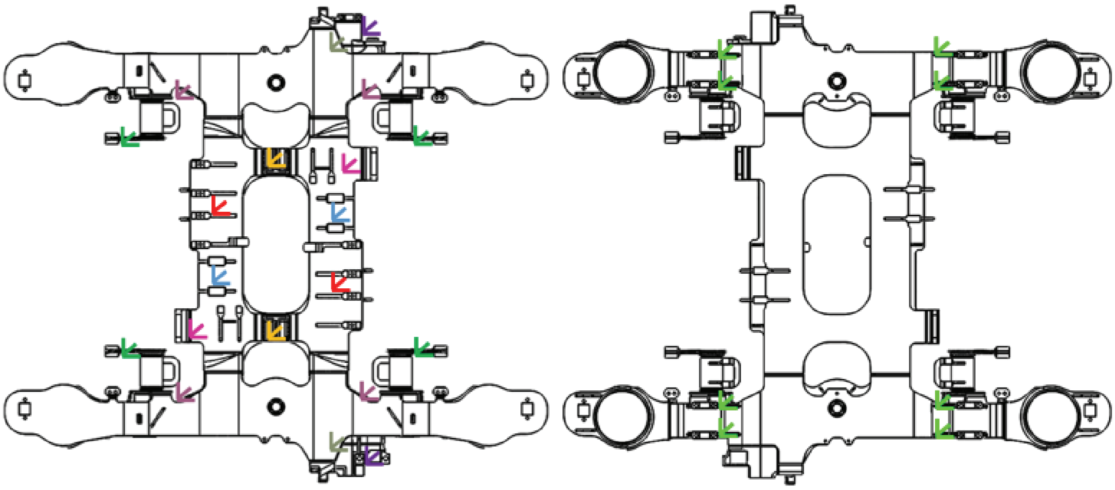

Figure 12. Measuring points diagram of bogie frame

Figure 13. Data acquisition system

Figure 14. Location plan of the tested bogie frame.

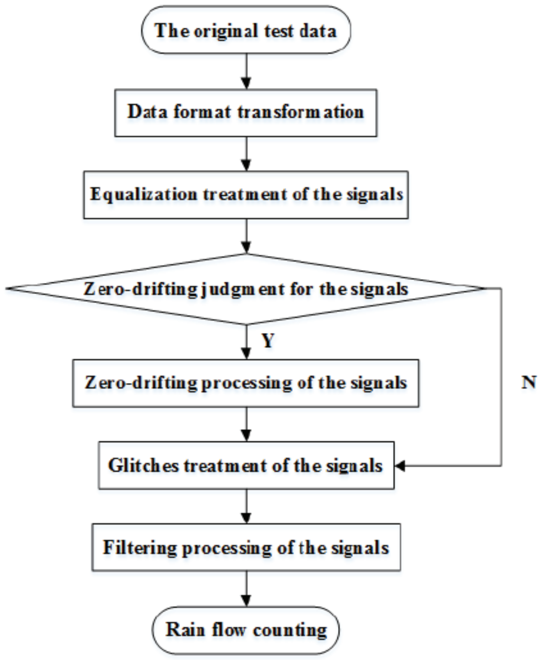

Figure 15. The flow chart of data processing.

od is used to process the time domain data. Table 6 is statistical counting result of one of the gearbox seat me- asuring point.

For the structure, the measured dynamic stress time history is often a subsample of limited length so that the dynamic stress spectrum cannot be directly used for fatigue strength evaluation. A feasible method is to carry on the statistical inference to get dynamic stress extension spectrum which contains the possible maximum value during the period of service. It is necessary to do the distribution fitting of measured dynamic stress spectrum before statistical inference. There are some common types of distribution such as truncated normal distribution, lognormal distribution and Weibull distribution. Through different values of shape parameter, the shape of Weibull distribution changes a lot and has a strong adaptability. Lognormal distribution has a good adaptability when the data distribution is uneven and high-low amplitude areas vary widely. In order to ha- ve a combination benefits of these two types of distribution, this paper combines the two types of distribution to become a new kind of distribution which is called combined distribution. The probability density function is set as follows:

$$f(x)=\frac{1}{K_n}[\varphi f(x)_1+(1-\varphi)f(x)_2] \tag{16}$$

The data in Table 6 is fitted by using of the combined distribution. The fitting curve and frequency distribution histogram are shown together in Figure 16.

Table 6: The rain flow count results of a gearbox seat measuring point.

Level	Class midpoint (MPa)	Frequency
1	6.73	378678
2	10.19	208683
3	13.66	98715
4	17.12	42743
5	20.58	17472
6	24.05	7305
7	27.51	3006
8	30.97	1301
9	34.43	618
10	37.9	292
11	41.36	148
12	44.82	80
13	48.29	50
14	51.75	25
15	55.21	18
16	60.41	8
17	70.8	8

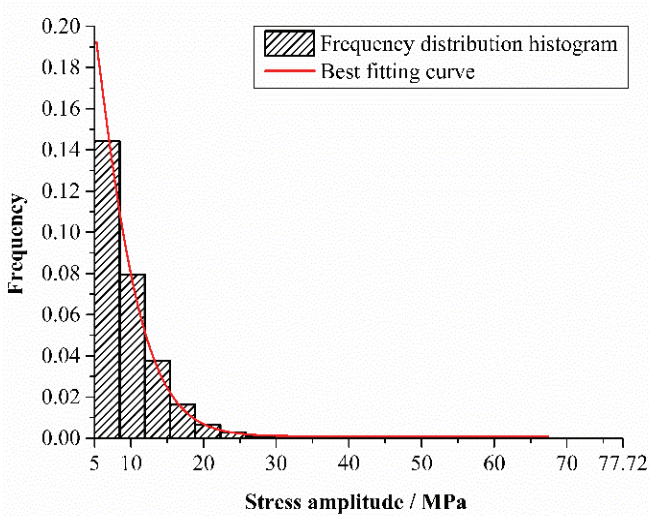

Figure 16. Frequency distribution histogram and fitting curve.

As can be visually seen from Figure 16, the fitting curve and frequency distribution histogram match very well.

4.3.3 The extension of stress spectrum and damage calculation

Due to the limited sample size of the dynamic stress time history data, it is necessary to do statistical inference to get the maximum stress value. According to [9], 10^{-6} should be seen as the maximum stress's probability of occurrence. The maximum stress that may occur during service period can be gotten by reverse solving the distribution function under the help of exceedance probability.

In this paper, the inferred maximum stress value is 81.13 MPa which is slightly larger than the measured maximum 77.72MPa. In order to get the measured extension spectrum, all levels of the measured spectrum need to be multiplied by a coefficient so that the total cycles can reach 10^{-6}. The minimum value of extension spectrum is also 5 MPa. The inferred results are shown in Table 7.

The damage can be calculated according to the extension spectrum of combined distribution. The calculation of damage is on the basis of Miner linear cumulative damage rule [10]. Considering the parameters of S-N curve, the formula can be modified as (17):

$$D=\sum_{i=1}^{17}\frac{n_i}{N_i}=\sum_{i=1}^{17}\frac{n_i\sigma_{-1i}^{m}}{C_3} \tag{17}$$

Table 7: Comparison of measured spectrum and extended spectrum.

Level	Measured spectrum		Extended spectrum	
	Amplitude (MPa)	Frequency	Amplitude (MPa)	Frequency
1	6.73	498818	7.24	532654
2	10.19	274890	11.72	262792
3	13.66	130034	16.20	112365
4	17.12	56304	20.68	54256
5	20.58	23015	25.16	22351
6	24.05	9623	29.64	8659
7	27.51	3960	34.12	3754
8	30.97	1714	38.60	1615
9	34.43	814	43.08	789
10	37.9	385	47.56	401
11	41.36	195	52.04	156
12	44.82	105	56.52	95
13	48.29	66	61.00	53
14	51.75	33	65.48	29
15	55.21	24	69.96	22
16	60.41	11	74.44	6
17	70.80	11	78.92	3

Design using mileage of the high-speed train is 12 million kilometers. According to Miner linear cumulative damage rule, Structure fatigue fracture will occur when the total damage equal to 1. That is to say, the total railway operation mileage is 12 million kilometers. However, the damage calculated by (15) is the damage that train runs 2636 kilometers. To dete-

rmine whether fatigue failure of each measuring point will happen when the train run 12 million kilometers, the measured damage should be converted to equivalent damage that train runs 12 million kilometers. Assuming that damage is proportional to train running mileage, then measured damage and equivalent damage can be listed as Table 8.

As can be seen from Table 8, equivalent damage values of all the frame measuring points are all less than 1. In addition, measuring points with the same types have damage value with the same order of magnitude.

Table 8: Measured damage value and equivalent damage value of each measuring point.

No.	Location	Measured damage	Equivalent damage
1	Traction rod seat	3.10E-07	1.41E-03
2		5.20E-07	2.36E-03
3	Motor suspension	7.70E-06	3.50E-02
4		7.70E-06	3.50E-02
5	Anti-rolling rod seat	1.20E-07	5.45E-04
6		1.20E-07	5.45E-04
7	Braking hanging brackets	4.20E-08	1.91E-04
8		2.20E-08	1.00E-04
9		4.70E-08	2.14E-04
10		3.20E-08	1.45E-04
11	Arc plate of locating seat	2.20E-05	1.00E-01
12		6.20E-05	2.82E-01
13		3.70E-05	1.68E-01
14		4.50E-05	2.05E-01
15		3.40E-05	1.55E-01
16		3.80E-05	1.73E-01
17		3.40E-05	1.55E-01
18		5.50E-05	2.50E-01
19	Inside of side beam top plate	8.20E-07	3.73E-03
20		5.20E-07	2.36E-03
21		3.40E-07	1.55E-03
22		8.40E-07	3.82E-03
23	Outside of side beam top plate	2.70E-06	1.23E-02
24		3.70E-06	1.68E-02
25	Reinforcing plate of lateral stop	7.70E-06	3.50E-02
26		6.90E-06	3.14E-02
27	Reinforcing plate of gearbox seat	2.20E-06	1.00E-02
28		7.20E-06	3.27E-02

5. Summary

In this paper, finite element simulation and fatigue test rig are implemented to assess static strength and fatigue strength of a bogie frame. In addition, actual running test was also operated to assess fatigue strength of the frame. The results show that static strength of the tested bogie frame meets requirements. For the measured dynamic stress data, Miner linear cumulative damage rule seems to be very effective when judging fatigue strength of the frame. All the above methods have proved that fatigue strength of the tested bogie frame meets requirement.

References

[1] EN 13749: railway applications – methods of specifying structural requirements of bogie frames. CEN Brussels; 2005.

[2] UIC 615-4: powered vehicles-bogies and running gear-strength tests of bogie frames. Paris; 1994.

[3] JIS E 4207: design specification of railway rolling stock bogie; 2004.

[4] Jung-Seok Kim. Fatigue assessment of tilting bogie frame for Korean tilting train: Analysis and static tests. Engineering Failure Analysis. 13 (2006) 1326-1337.

[5] M. Kassner. Fatigue strength analysis of a welded railway vehicle structure by different methods. Int J Fatigue. 34 (2012) 103-111.

[6] Jung-Seok Kim, Nam-Po Kim. Evaluation of structural safety of a tilting bolster. Engineering Failure Analysis. 14 (2007) 63-72.

[7] Jeong-Woo Han, Jae-Dong Kim, See-Yeob Song. Fatigue strength evaluation of a bogie frame for urban maglev train with fatigue test on full-scale test rig. Engineering Failure Analysis 31 (2013) 412-420.

[8] Bin Xiang, Jianping Shi, Lingyan Guo, Xuewen Liu, Shuhua Liu, Jizhong Lin. Plotting and application of Goodman fatigue limit diagram of railway common materials. China Railway Science. 23 (2002) 72-76.

[9] Dangxiang YI, Guozhi LV, Xiongwei ZHOU. Maximal loading calculation for two dimensional fatigue design spectrum under multiple working conditions with probability extrapolation method. Chinese Journal of Applied Mechanics, 03 (2006) 484-487+517.

[10] Miner M A. Cumulative damage in fatigue. J Appl Mech, 12(3) (1945) 159-164.

Viser Technology Pte. Ltd.
Mechanical Engineering Science
https://doi.org/10.33142/me.v1i1.664

Research Article Open Access

Study on Vertical Vibration Characteristics of the 2-DOF Strip Rolling Mill Model with a Single Weak Defect on the Work Roll Bearing Outer Raceway

Zhengnan Sun[1], Dongxiao Hou[1*], Liang Xu[1], Peiming Shi[2]

[1]Department of Control Engineering, Northeast University at Qinhuangdao, Qinhuangdao, China
[2]School of Electrical Engineering, Yanshan University, Qinhuangdao, China

***Corresponding Author:** Dongxiao Hou, Qinhuangdao, Hebei 066004, China; houdongxiao1982@163.com*

Abstract:
Considering the influence caused by a early single pit defect on the outer raceway of the work roll bearing, a 2-DOF plate strip rolling mill vertical vibration model with a single point weak fault on the outer raceway was established. With the practical parameters of the roughing mill of the 1780 hot continuous rolling mill, the vertical vibration characteristics of the rolling mill work roll with different rotating speed and different single pit defect area on the bearing outer raceway are analyzed by numerical simulation. It is found that with the change of the rotation speed of the work roll, different nonlinear vibration behaviors occurred, such as superharmonic resonance, main resonance, com-bined resonance and sub-harmonic resonance. Especially the subharmonic resonance of the work roll is more harmful than the main resonance when the work roll speed is twice the rotation speed corresponding to the first and second natural frequency of the rolling mill. This work provides a theoretical basis for further clarifying the effect caused by a early defect of the work roll bearing on the mill vibration.

Keywords: *Work roll bearing; Weak defect; Strip mill; Vertical vibration*

Citation: Z.N. Sun et al, Study on Vertical Vibration Characteristics of the 2-DOF Strip Rolling Mill Model with a Single Weak Defect on the Work Roll Bearing Outer Raceway. *Mech Eng Sci*, 2019,1(1): 65-70. https://doi.org/10.33142/me.v1i1.664

1. Introduction

With the increase requirements in rolling speed and product quality, the problem about vibration of the strip mill has become increasingly prominent. The vibration not only affects the surface quality of the rolled product, but the frequent vibration also accelerates the wear of the rolling equipment components, thereby reducing the service life of the rolling equipment. There are many reasons for the vibration of the rolling mill, Wu et al. studied the effects of different sizes defects on the surface of the work roll of the Sendzimir 20-high rolling mill on the vibration characteristics, which provides a theoretical basis for monitoring the indentation defects on the surface of the work roll[1]. Lu et al. proposed a dynamic increment model for chatter in a Universal Crown Contral mill(UCM mill), which considering strip hardening, elastic deformation of the work roll, nonlinear friction, transfer delay of the strip and dynamic coupling effect of tension between adjacent stands,and his work provides a more accurate prediction of mill chatter and a basis for optimal design of rolling parameters[2]. Shi studied the influence casued by the angle of the jointed shaft in the drivelines of the rolling mill and the friction force of the roll gap on the nonlinear vibration of the rolling mill, and found that the optimal angle of the jointed shaft is 4.7613°[3]. Study by Vladimir et al. have shown that the main cause of chatter in the rolling mill is the frictional conditions in the roll gap, and then is the residual chatter marks on the roll, which sometimes can also cause chatter[4].

A work roll bearing defect can also cause the vibration of the rolling mill as a common factor. Son et al. first proposed that the defect of the work roll bearing and the backup roll oil film bearing can cause the vibration of the rolling mill[5]. Wu et al. analyzed the vibration power spectrum of the rolling mill by measuring the vibration of the high-speed rolling mill, and found that the frequency modulation is caused by 12 ripples in the inner raceway of the work roll bearing[6]. Youngdeuk et al. established a six-degree-of-freedom vibration model of a cold tandem mill considering the stiffness caused by roller bearings and contact between rolls, the chatter frequency affecting the rolling performance was found by studying the dynamic characteristics of the rolling mill vibration[7]. Work roll bearings are important rotating parts in the mill work stand, which carries a heavy working load and in a poor working environment. Its operating state directly affects the rolling precision of the rolling mill. The rolling mill often vibrates when the work roll bearing has a certain degree of defect. And then the quality of the product is affected. At present, the vibration behavior caused by the failure of the rolling mill work roll bearing, are often measured and diagnosed from the bearing alone, which neglecting the mutual coupling between the work roll bearing and the rolling mill mechanical structure. Therefore, it is impossible to find out the influence rule of the work roll bearing defect on the nonlinear vibration of the rolling mill.

Therefore, this paper established a vertical vibration model of a two-degree-of-freedom strip mill with a single point pit defect on the work roll bearing outer raceway. With the practical parameters of the roughing mill of 1780 hot continuous rolling mill, analyzing the vertical vibration dynamics of the rolling mill under the conditions of different work roll speeds and single pit defect areas on bearing outer raceway, which provides a theoretical basis for further clarifying the effect of a early defect of the work roll bearing on the rolling mill vibration. In actual production of the factory, we can estimate whether the working roll bearing is likely to fail according to its vibration characteristics when the mill vibrates. Replace the defected bearing in time. Finally, the production efficiency of the factory is improved.

2. The 2-DOF Vertical Vibration Model of the Rolling Mill with a Single Pit Weak Raceway Defect on the Work Roll Bearing

2.1. Contact Force Model of the Work Roll Bearing with a Single Pit Weak Raceway Defect

Considering the bearing outer raceway weak defect, idealized the defect area as a closed ellipse, so the schematic diagram of the weak defect model on the outer raceway of the work roll bearing can be drawn, as shown in Figure 1.

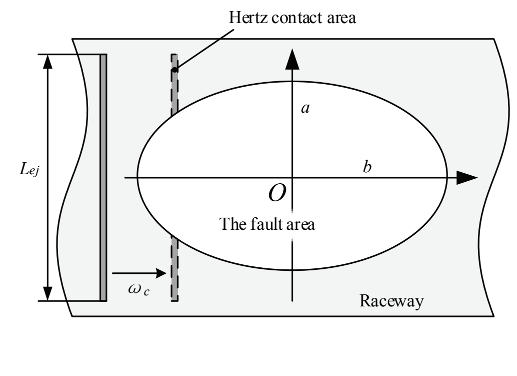

Figure 1. Schematic diagram of weak defect model on the outer raceway

In the Figure 1, L_{ej} is the effective contact length between the rolling element j and the outer raceway, ω_c is the rotation angular velocity of the cage, a is the short axis length of the elliptical defect zone, and b is the long axis length of the elliptical defect zone. According to the defect model in Figure 1, the total contact force $F_b(x_2)$ between the roller and the raceway is[8]

$$F_b(x_2)=\sum_{j=1}^{Z}K_j\delta_j(t)^{10/9}\cos\alpha\sin\varphi_j(t) \tag{1}$$

In Equation (1), Z is the number of rollers in the bearing, $\varphi_j(t)$ is the position of rolling element j, $\varphi_j(t)=2\pi(j-1)/Z+\omega_c t$. ω_c is the rotation angular velocity of the cage, $\omega_c=(n\pi/60)(1-D_b\cos\alpha/((d_o+d_i)/2))$, n is the run speed of the work roll, D_b is the average diameter of the roller cross section, d_o and d_i are the outer diameter and inner diameter of the bearing, respectively. K_j is the total contact stiffness between the inner and outer raceways of the work roll bearing and rolling element j.

$$k_j=8.06\times10^4L_{ej}^{8/9}2^{9/10} \tag{2}$$

With L_{ej} is defined as

$$L_{ej}=\begin{cases}L_e-y,\theta<\dfrac{\varphi_d}{2}\\[2mm] L_e,\quad\theta\geq\dfrac{\varphi_d}{2}\end{cases} \tag{3}$$

Where L_e is the ideal contact length between the roller and the outer raceway without defect, φ_d is the angular extent of the outer raceway defect, which is defined as $\varphi_d=4b/D_0$. θ is the angular distance between the defect center and Hertz contact line for rolling element j and the outer raceway, $\theta=|\mathrm{mod}(\varphi_j(t),2\pi)-1.5\pi|$. y is the length of the roller that is not in effective contact with the raceway in the defect zone, and is defined as

$$y=2a\sqrt{1-\theta^2D_0^{\,2}/(4b^2} \tag{4}$$

Where D_0 is the average diameter of the outer raceway surface.

The contact deformation $\delta_j(t)$ for rolling element j between the inner and outer raceway is given by

$$\delta_j(t)=x_0\sin\varphi_j(t)\cos\alpha+x_2\cos\varphi_j(t)\cos\alpha+z_0\sin\alpha \tag{5}$$

Where x_0, x_2 and z_0 is the relative displacement of the inner and outer raceway in the horizontal direction, the vertical direction and the axial direction, respectively.

2.2. 2-DOF Vertical Vibration Model of the Rolling Mill with a Weak Defect on the Work Roll Bearing Outer Raceway

Considering the influence of the contact force of the work roll bearing with defect in Equation (1), a 2-DOF vertical vibration model of the rolling mill with a weak defect of the work roll bearing can be established, as shown in Figure 2.

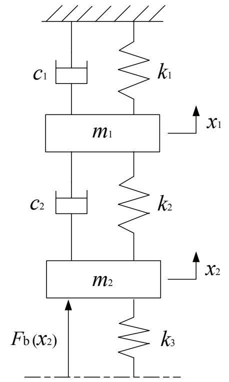

Figure 2.2-DOF vertical vibration model of the rolling mill with a weak defect on the work roll bearing

The model includes a equivalent mass m_1 representing the upper backup roll, its bearing and bearing seat. a equivalent mass m_2 representing the upper work roll, its bearing and bearing seat. The spring and damper constants k_1 and c_1 represent the stiffness and damping between the upper backup roll and the middle part of mill beam. The spring and damper represent the spring and damper constants k_2 and c_2 represent the stiffness and damping between the upper backup roll and the upper work roll. The spring costant k_3 represents the stiffness between the work roll and the strip. The force $F_b(x_2)$ represents the faulty reaction force of the work roll bearing to the work roll.

Using the rolling mill vertical vibration model in Figure 1, the equations of the dynamic motion are now given by

$$\begin{aligned} &m_1\ddot{x}_1 + c_1\dot{x}_1 + c_2(\dot{x}_1 - \dot{x}_2) + k_1x_1 + k_2(x_1 - x_2) = 0 \\ &m_2\ddot{x}_2 + c_2(\dot{x}_2 - \dot{x}_1) + k_2(x_2 - x_1) + k_3x_2 = F_b(x_2) \end{aligned} \tag{6}$$

3. Simulation and Analysis

Using the actual parameters of the rough rolling mill of the 1780 hot strip mill in a factory[9], the mechanical parameters of the rolling mill are shown in Table 1.

Table 1. Mechanical structure parameters of the roughing mill of the 1780 hot strip mill

Variable	Unit	Value
m_1	*kg*	7.59×10^4
m_2	*kg*	1.596×10^4
k_1	*N/m*	3.241×10^{10}
k_2	*N/m*	5.948×10^{10}
k_3	*N/m*	2.566×10^{10}
c_1	*N•s/m*	3×10^6
c_2	*N•s/m*	5×10^5

The structural size parameters of the work roll bearing are shown in Table 2.

Table 2. Parameter values of the rolling mill bearing

Description	Variable/Unit	Value
Outer diameter	d_o/mm	900
Inner diameter	d_i/mm	710
Average diameter of the outer raceway surface	D_0/mm	845
Average diameter of the roller cross section	D_b/mm	49.8
Roller effective length	L_e/mm	53.64
Number of rollers	Z	32
Contact angle	α	13°8′ 21″

3.1. Calculation of a Single Pit Defect Frequency on Bearing Outer Raceway

The frequency of the bearing rolling element passing through a point on the outer ring raceway is calculated as[10]

$$f_o = \frac{Zn}{120}\left(1 - \frac{D_0}{d_m}\cos\alpha\right) \tag{7}$$

The first and second natural frequencies of the two-degree-of-freedom rolling mill vertical vibration model can be calculated from Equation (6) as follows

$$\begin{cases} f_1 = 122.84 \text{ Hz} \\ f_2 = 391.19 \text{ Hz} \end{cases} \tag{8}$$

3.2. Analysis of Vibration Characteristics of the Work Roll with a Single Pit Defect on Bearing Outer Raceway

Figure 3-5 present the frequency spectrum waterfall figures of the vertical vibration displacement of the work roll with the change of the work roll rotation speed, when the defect area S of the work roll bearing outer raceway is 8.75π mm², 35π mm² and 140π mm² respectively.

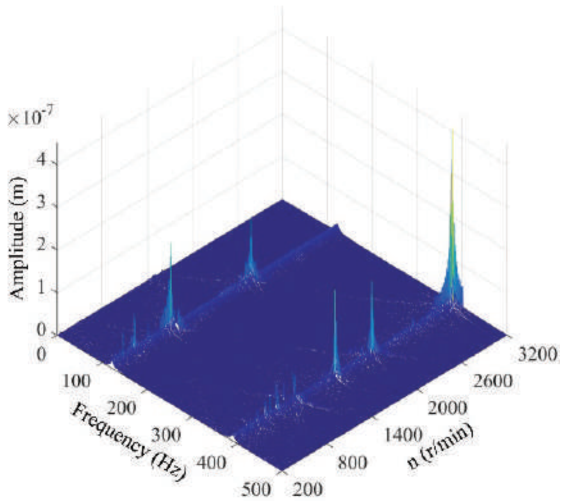

Figure 3. The frequency spectrum waterfall of the vibration displacement of the work roll with the change of the work roll rotation speed (S=8.75π mm²)

Figure 3 presents that the work roll exhibits different spectrum characteristics with different speeds, when the rotation speed reaches 490r/min (the rotation speed corresponding to the first natural frequency), its spectrum curve shows a distinct peak at 123 Hz, at this point, the rolling mill has resonance at the first natural frequency. When the rotation speed reaches 980 r/min (twice the speed corresponding to the first natural frequency), the resonance of the first natural frequency in the work roll will become more intense, the sub-harmonic resonance occurred in the rolling mill at this time, we can see that the subharmonic resonance has a greater influence than the main resonance according to this phenomenon. Therefore, except the work roll rotation speed corresponding to the first natural frequency, it is necessary to avoid twice the rotation speed of the work roll corresponding to the first natural frequency. When the rotation speed reaches 1561 r/min, the work roll exhibits a main resonance of the second natural frequency. When the rotational speed reaches 2051 r/min, resonance of the first and the second natural frequency occurs at the same time, and this behavior also called the combined resonance. When the rotation speed reaches 3122 r/min (twice the rotation speed corresponding to the second natural frequency), the sub-harmonic resonance of the second natural frequency appears again on the work roll.

Figure 3-5 present that sub-harmonic resonance of the second natural frequency will be weakened as the defect area increases, but the main resonance is enhanced when the defect frequency is consistent with the first and second natural frequencies, respectively. Among the vibration behaviors caused by the work roll rotation speed from 200 r/min to 3200 r/min, when the defect frequency is twice the work roll speed corresponding to the first and second natural frequencies, the induced subharmonic resonance is the most serious, respectively. In particular, the subharmonic resonance caused by the defect frequency being twice the second natural frequency of the rolling mill is the most serious.

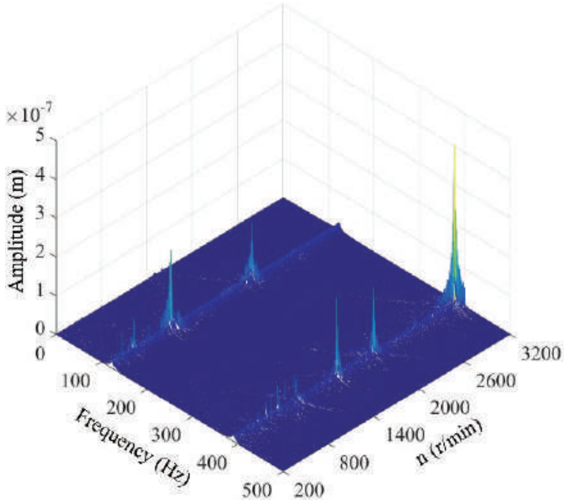

Figure 4. The frequency spectrum waterfall of the vibration displacement of the work roll with the change of the work roll rotation speed (S=35π mm²)

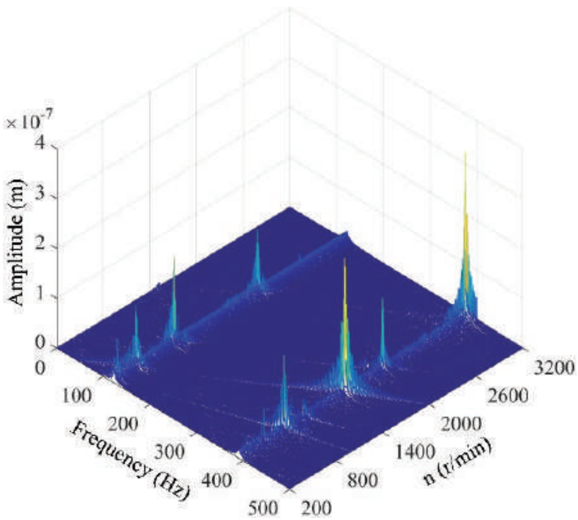

Figure 5. The frequency spectrum waterfall of the vibration displacement of the work roll with the change of the work roll rotation speed (S=140π mm²)

Figure 6 presents the vibration displacement of the work roll under the working conditions of the work roll bearing without defect and micro-defect (the bearing outer raceway defect area is 8.75π mm²) when the work roll rotation is 200 r/min (no resonance). The partial enlargement in the figure is the comparison curve when the vibration reaches steady state. It can be seen that when there is a defect, the work roll exhibits a vibration behavior; however, as the defect is weak, the vibration amplitude of the work roll is very small (the amplitude fluctuation is about 2.2×10^{-8} m).

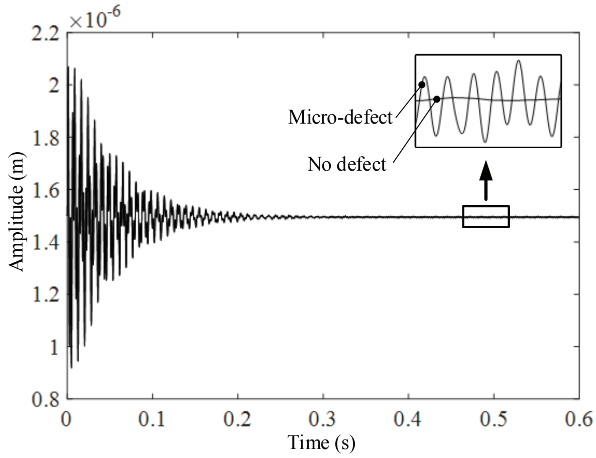

Figure 6. Work roll vibration displacement with or without micro-defect

In the Figure 6, the speed of the working roller is 200 r/min (the defect frequency is 50.12 Hz at this speed), the single pit weak defect area S of the work roll bearing is 35π mm², there is the displacement time domain curve of the work roll vibration and its corresponding spectrum analysis curve.

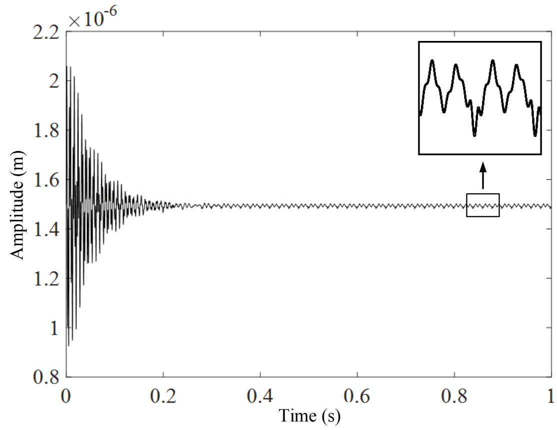

(a) Displacement of the work roll

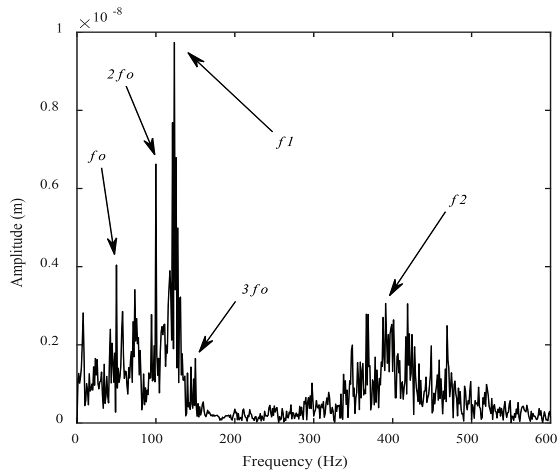

(b) Spectrum analysis of the work roll

Figure 7. Vibration displacement and spectrum of the work roll(n=200 r/min， S=35π mm²)

In the Figure 7(a), the rolling mill presents complex periodic vibrations at this point. Also, we can see that the vibration frequency component of the work roll is very complicated at this time. In addition, except the defect frequency f_o, the natural frequencies f_1 and f_2, other frequency components appear, such as $2f_o$ and $3f_o$.

In the Figure 8, the speed of the work roll is 490.17 r/min (the speed corresponding to the second natural frequency), the single pit weak defect area S of the work roll bearing is 35π mm^2, there is the displacement time domain curve of the work roll vibration and its corresponding spectral analysis curve.

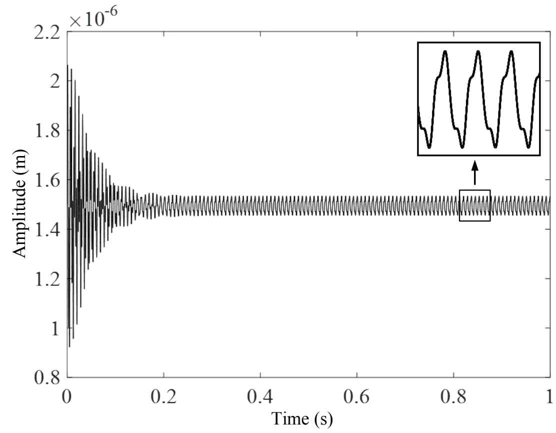

(a) Displacement of the work roll

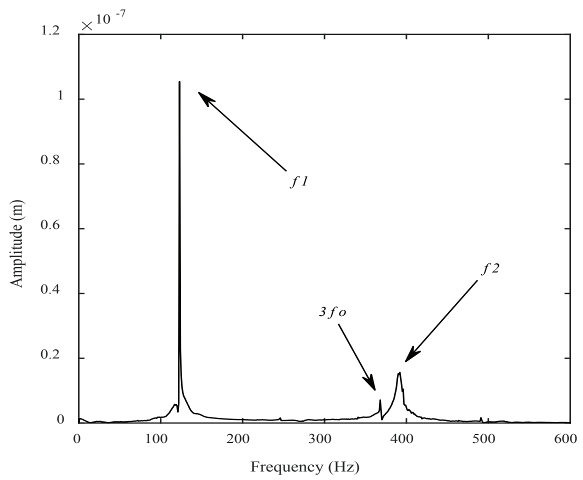

(b) Spectrum analysis of the work roll

Figure 8. Vibration displacement and spectrum of the work roll(n=490.17 r/min, S=35π mm^2)

In Figure 8(b), we can see that except the first and second natural frequency components of the work roll vibration frequencies, there is also a triple frequency component of the first frequency, and the first natural frequency has the largest amplitude among the frequency components.

In Figure 9, the speed of the work roll is 1561 r/min (The speed corresponding to the second natural frequency), the single pit weak defect area S of the work roll bearing is 35π mm^2, there is the displacement time domain curve of the work roll vibration and its corresponding spectral analysis curve

In Figure 9(b), we can see that the vibration frequency components of the work roll contain the first and second natural frequency components, and the second natural frequency has the largest vibration amplitude.

4. Conclusion

(1) Considering the early single pit weak defect on the outer raceway of the work roll bearing, the vertical vibration model of a 2-DOF strip mill with a weak defect of the work roll bearing is established.

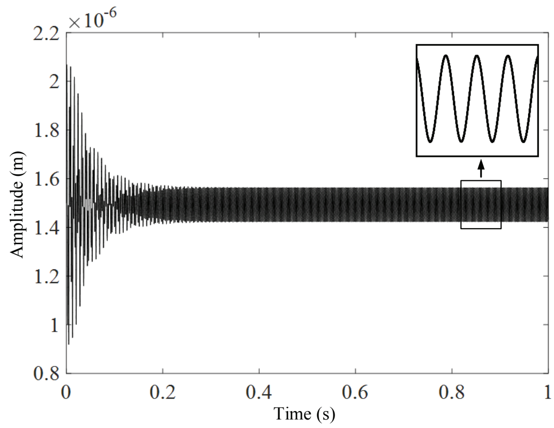

(a) Displacement of the work roll

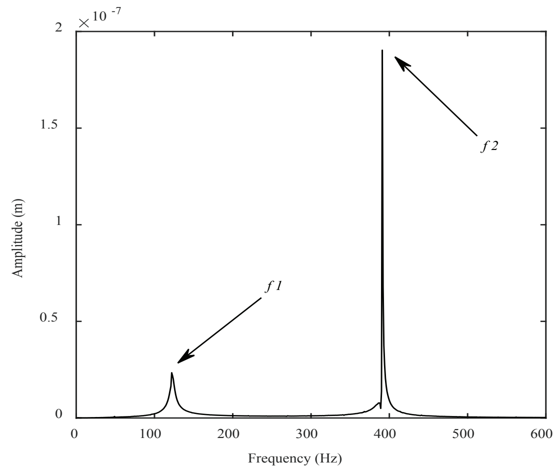

(b) Spectrum analysis of the work roll

Figure 9. Vibration displacement and spectrum of the work roll(n=1516 r/min, S=35π mm^2)

(2) When a single pit weak defect presents on the outer raceway of the work roll bearing, the work roll exhibits nonlinear vibration behaviors such as main resonance, superharmonic resonance, subharmonic resonance, and combined resonance. As the defect area S is 35π mm^2 (the defect is weak), the subharmonic resonance becomes the most severe. As the defect area increases gradually, the subharmonic resonance weakens and the main resonance increases.

(3) The research work of this paper has important reference significance for the simulation of rolling mill vibration with defect on the work roll bearing practically and further clarifying the vibration mechanism of the rolling mill caused by the defect on the outer raceway of the work roll bearing.

Author Contributions: This article presented in the paper was completed by Sun in theoretical derivation and simulation. Hou

proposed the idea of the article. Xu and Shi assisted Sun in completing the simulation.

Conflict of Interest: No conflict of interest was reported by the authors.

Acknowledgments: This research is supported by Natural Science Foundation of China (Grant no. 51405068), Natural Science Foundation of Hebei Province of China (Grant no.E2019203146), and Natural Science Foundation of Hebei Province of China (Grant no.E2014501006).

References

[1]. Shengli Wu, Liming, Yinmin Shao, *et al*. Vibration characteristic analysis of twenty-high rolling mill with local defect on roll surface based on the time-varying contact stiffness. Engineering Failure Analysis 2014; 42: 297–310.

[2]. Xing Lu, Jie Sun, *et al*. Dynamic analysis of vibration stability in tandem cold rolling mill. Journal of Materials Processing Technology 2019; 272:47–57.

[3]. Pei-ming SHI, Ji-zhao LI, *et al*. Nonlinear Dynamics of Torsional Vibration for Rolling Mill's Main Drive System Under Parametric Excitation. Journal of Iron and Steel Rsearch, International 2010; 20: 7–12.

[4]. Vladimir Panjkovic, Ronald Gloss, John Steward, *et al*. Causes of chatter in a hot strip mill: Observations, qualitative analyses and mathematical modelling. Journal of Materials Processing Technology 2012; 212(4): 954–961.

[5]. Son, B., Roh, Y., and Lee, Y., "The Cause of Vibration at Finishing Stands in a Hot Strip Mill," Korean Society for Noise and Vibration Engineering 1994; 1(4), 43–50,.

[6]. Wu, Y. X. and Duan, J. A., Frequency modulation of high-speed mill chatter, J. Mater. Process. Technol. 2002; 129: 148–151.

[7]. Youngdeuk Kim, Chang-Wan Kim, Sungjin Lee, and Hyunchul Park. Dynamic Modeling and Numerical Analysis of a Cold Rolling Mill. International Journal of Precision Engineering and Manufacturing 2013; 14(3): 407–413.

[8]. Xiang LI, Li-yan HAN, Yong-sheng ZHU, *et al*. Fault diagnosis based on nonlinear dynamic modeling in tapered roller bearing. Journal of Vibration and Shock 2014; 33(S):128–131.

[9]. Jing Zhao. Vibration analysis of 1780 HSM R1 machine. Qinhuangdao: Yanshan University, 2011.

[10]. Dick Petersen, Carl Howard, Nader Sawalhi, *et al*. Analysis of bearing stiffness variations, contact forces and vibrations in radially loaded double row rolling element bearings with raceway defects. Mechanical Systems and Signal Processing 2015; 50–51: 139–160.

Publisher: Viser Technology Pte. Ltd.

URL: www.viserdata.com

Add.:21 Woodlands Close, #08-18,

Primz Bizhub SINGAPORE (737854)